Journal of Radar and Optic Remote Sensing

Volume 1, Issue 2

May – June 2018

Islamic Azad University, Yazd Branch, Iran

Permission to publish Journal of Radar and Optic Remote Sensing

With respect to the Reference Number: **96/ص/87/7**dated 1396/01/14(3th April 2017), the 104th commission session was held to evaluate and approve the scientific journal of the Islamic Azad University. The commission announced to grant permission to establish the journal entitled "Journal of Radar and Optic Remote Sensing".

Editorial team of JRORS

Acknowledgement

JRORS would like to thank the following people for their contributions to this volume.

Reviewers

Dr. Seyed Ali Almodaresi

Dr. Ali Akbar Jamali

Dr. Reza Attarzadeh

Dr. Mehdi Tazeh

Dr. Ali Reza Khavaninzadeh

Dr. Mohammad hosseinpour

Dr. Karim Naghdi

Dr. Mohammad Hossein Mokhtari

Dr. Khalil Valizadeh Kamran

In the Name of God

Dear Readers,

I have the enormous opportunity to share the first journal publication to the readers. The Journal of Radar and Optic Remote Sensing (JRORS) is the first radar journal and the first scientific journal in this area of Islamic Azad University (2017). The first issue will be published this year by the Islamic Azad University, Yazd Branch. The publication of the articles resulting from the scholarly research findings contributes to the advancement of knowledge and performance of remote sensing and radar. This journal focuses on original research papers that develop a basic knowledge in the field of remote sensing and radar.

Over the past years, many research articles have been received in the specialized field and just a few have been accepted for publication in each issue based on the reviewers' and the editorial team's decisions regarding the articles. This has somehow upset the authors. Therefore, an apology on behalf of the editorial team for declining and or delaying the publication of some of these inter-disciplinary scholarly articles. It is hoped to add the scientific richness of the journal by releasing articles that reflect your valuable research activities, providing us with the latest publications in the scientific community of remote sensing and radar.

Finally, I would like to sincerely thank the Editorial Board for their dedication to prepare the first issue. It was their efforts that made it possible to publish the first issue on time.

Sincerely,

Dr. Seyed Ali Almodaresi

Editor-in-Chief

Journal of Radar and Optic Remote Sensing

www.jrors.ir

INDEX

Available online at www.jrors.ir

JRORS
Journal Of Radar and Optic Remote Sensing

Journal Of Radar and Optic Remote Sensing

JRORS 2 (2018) 7–23

Inventory of Single Oak Trees Using Object-Based Method on WorldView-2 Satellite Images and Earth

Yousef Taghi Mollaei [a*] , Abdolali Karamshahi [b] , Seyyed Yousef Erfanifard [c]

[a] *Ph.D. Student of forestry in Ilam University*
[b] *Associate Professor and Faculty Member of Forest Sciences Department in University of Ilam*
[c] *Associate Professor, Department of Natural Resources and Environment, College of Agriculture, Shiraz University, Shiraz, Iran*

Received 14 March 2018; revised 15 October 2018; accepted 21 October 2018

Abstract

Remote sensing provides data types and useful resources for forest mapping. Today, one of the most commonly used application in forestry is the identification of single tree and tree species compassion using object-based analysis and classification of satellite or aerial images. Forest data, which is derived from remote sensing methods, mainly focuses on the mass i.e. parts of the forest that are largely homogeneous, in particular, interconnected) and plot-level data. Haft-Barm Lake is the case study which is located in Fars province, representing closed forest in which oak is the valuable species. High Resolution Satellite Imagery of WV-2 has been used in this study. In this study, A UAV equipped with a compact digital camera has been used calibrated and modified to record not only the visual but also the near infrared reflection (NIR) of possibly infested oaks. The present study evaluated the estimation of forest parameters by focusing on single tree extraction using Object-Based method of classification with a complex matrix evaluation and AUC method with the help of the 4th UAV phantom bird image in two distinct regions. The object-based classification has the highest and best accuracy in estimating single-tree parameters. Object-Based classification method is a useful method to identify Oak tree Zagros Mountains forest. This study confirms that using WV-2 data one can extract the parameters of single trees in the forest. An overall Kappa Index of Agreement (KIA) of 0.97 and 0.96 for each study site has been achieved. It is also concluded that while UAV has the potential to provide flexible and feasible solutions for forest mapping, some issues related to image quality still need to be addressed in order to improve the

* Corresponding author. Tel: +98-9176515623.
E-mail address: taghimollaei@yahoo.com.

classification performance.

Keywords: Separation of single trees, Canopy, Remote sensing, Classification, Zagros forests, Haft-Barm of Shiraz.

1. Introduction

Forest inventory was traditionally a useful and accurate way of monitoring forest coverage, but updating cycle is relatively expensive Extra, if it's not direct quoting (Franklin, 2001; Zoèhrer, 1980; Gillis and Leckie, 1993). Wide range of forest can change rapidly, forest inventory traditionally Did not respond adequately to the development of change (Wulder et al., 2008). The climate warming and recent severe droughts have resulted in vegetation mortality in various woody biomasses across the globe (Allen et al., 2010; Breshears et al., 2005; Carnicer et al., 2011; Phillips et al., 2009; van Mantgem et al., 2009).

The separation of single trees and the extraction of tree-related structural data from remote sensing data has been a prominent application in a variety of activities e.g. detailed information on the level of individual trees can be used to monitor forest regeneration (Gougeon and Leckie, 1999; Clark et al., 2004a and 2004b). The reduction of fieldwork is required for surveying (Gong et al., 1999) and damage assessment to be used in the forest (Leckie et al., 1992; Levesque and King, 1999; Kelly et al., 2004).

Forest data, which is derived from remote sensing methods, mainly focuses on the mass (such as parts of the forest that are largely homogeneous, in particular, interconnected) and plot-level data. However, forest level variables are mainly average or aggregate of the combination of trees in the mass. In calculating forest variables such as volume and biomass of the growing population, model at single-tree level are mainly used today (Laasasenaho, 1982; Repola, 2009). Remote sensing data allows us to move from the surface of the mass to the level of single trees, which has a clear interest in precise forestry, forest management planning, biomass assessment and forest modeling (Koch et al., 2006).

The reasons for single-tree extraction from high-resolution satellite imagery are the importance of single trees and their maintenance such as the difficulty in single tree mapping in vulnerable areas, the need for quick access to quantitative characteristics estimation and the importance of remote sensing in statistics for single trees (spatial resolution and satellite data capability has been increasingly enhanced).

So far, no research has been done to estimate the single-tree feature on WV-2 images. In previous studies, the accuracy of estimating the crown area is made using field data, in which the crown shape of the trees is generally considered circular and the crown area is obtained from the mean diameter, provided that the trees, according to the possible vegetative conditions, has crowns with non-hinged shapes. Therefore, it is necessary to assess the accuracy of crown areas in satellite data using more reliable data such as UAV aerial imagery.

Today, remote sensing data provides accurate and reliable information of single-tree biophysical properties in forest lands. In addition, the object-based classification has a particular advantage over other classification methods for extracting crowns and identifying species in a variety of ecosystems. Few study has been done to examine the efficiency of the object-based, which is highly desirable for users.

Remote sensing is a useful tool for forest mapping as it provides data and resources. Today, one of the most commonly used applications in forestry is the identification of single trees and tree species comparison using object-based analysis and classification of satellite or aerial images. Sedliak et al. (2017) identified groups of trees (leaf-leaf needles) in individual structures of massive mixed grass, spruce, and pine forests in WV-2 images. The object-based classification with WV-2 multispectral images was done in eCognition software. The Lidar data has been used for the identification of single tree with overall high accuracy of 87.42 percent. The accuracy of needle calves had risen from 82.93 to 85.73 percent and broadband ranged from 84.79 to 90.16 percent.

Basic object classification method is a useful method to identify the wild plants in numerous habitats. Niphadkar et al. (2017) used WV-2 images to identify shrubs in the tropical forests. The object-based method separates the features with the help of spatial characteristics. As a result, there has been the possibility to isolate the shrub in a complex tropical forests environment, with a non-parametric classification algorithm.

The accuracy of the tree species map allows more detailed analyzes of forest biophysical variables. Raczko and Zagajewski (2017) compared the support vector algorithms, random forest and neural network for the tree species class on aerospace aerial imagery. The results showed that the ANN classification had the highest classification accuracy of (77%), and SVM with 68% and RF with 62% respectively.

Juniati and Arrofiqoh (2017) compared the base pixel and base object classification using parametric and nonparametric methods for pattern matching in Indonesian forests with WV-2 images. They concluded that classifying the base object the best results in segmentation and classification and has the best kappa coefficient, after which the neural network and the Maximum Likelihood Classifier were ranked in the mean of accuracy.

Wen et al. (2017) concluded that the method of classification of piece-based and object based on other methods in extracting urban trees in WV-2 images is superior. They used three levels of classification (pixel, object and piece) to classify trees. The results showed 85% overall accuracy for all methods. In addition, user and producer accuracy reaches over 80% for the tree floor. The method of classification of the base unit was placed in the first priority, then the classification of the object based and in the third stage of the base pixel for the Kappa coefficient.

Okojie (2017) paid for extraction of single tree crowns and evaluated forest structure parameters using airborne UAV images. Accuracy assessment was performed using the root mean square error method. As a result, the crown of the trees and the height of the trees were extracted. The results of the baseline image analysis showed that the segmentation accuracy is significantly related to the spatial resolution of the images, but the internal parameters of the segmentation algorithm should also be appropriate and calibrated.

Thanh and Kappas (2018) compared the random forest tree classifier, the nearest neighbor and vector of support for land use classification using Sentinel-2 multispectral images around the Red River Delta of Vietnam. The accuracy of all classifications was between 90% and 95%. Among these classifications, using different training samples ranging from 50 to 1250 pixels, SVM created a higher overall accuracy. After that, the random forests were ranged with the nearest neighbor.

Estimating forest structural parameters is expensive and time-consuming with ground-based data collection methods. Remote sensing data is a low cost option in modeling and mapping structural parameters in large forest areas.

2. Materials and Methods

2.1. Study Area

The Haft-Barm Lake is located in the geographical location of N294921 E520227 in Fars province. These lakes are located 55 kilometers to the west of Shiraz and northeast of the protected areas of Arjan and Parishan and 2150 meters above sea level. The lakes have beautiful panoramic views of the hillocks and wetlands. The weather in the region is cold and dry in the winter and temperate in the summer. The area has an almost cold and semi-desert climate and its catchment area is 16.9 km^2 and the average annual precipitation is 1010 mm. The various plant species forms the forest and pasture and the vegetation cover. Oak trees are the major forest species in the region that are densely covered by the area. Regarding the range of Arjan between the tropical region of southern Iran and the dry region of the south-east, the cold and semi-humid part of the northwest is an intermediate or ecotone region and very diverse in terms of plant species diversity. This study was conducted on two different sites in the Haft-Barm area of Shiraz. The area of the first site (Baleh Zar village) is 106 hectares, and the second site of the Abe Anar village is 150 hectares (Figure 1).

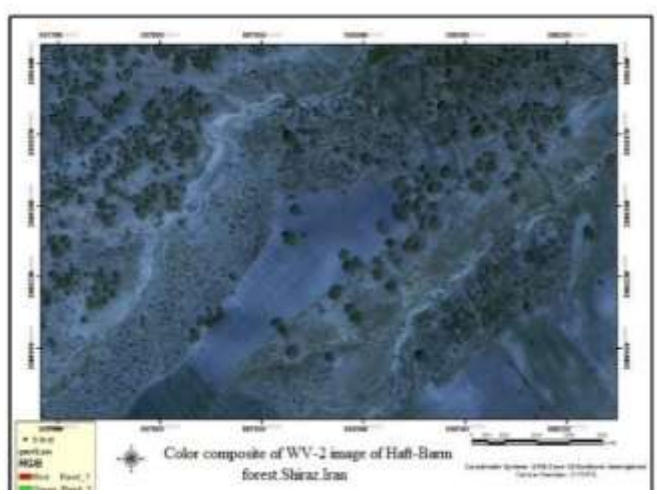

Figure 1. Study area location.

2.2. Data

The data used in this study included the image of the WorldView-2 satellite on May 21, 2015 with a resolution of 1.8 m, and panchromatic bands (spatial resolution of 0.5 m) and UAV aerial imagery with a resolution of 3 cm. Topographic maps of the survey organization with a scale of 1:25,000 and points taken by three-frequency GPS. Also, the SPSS25; Excel version 2016; eCognation v. 8.7; ENVI, 5; Erdas Imagine and Google Earth were used. The flowchart is shown in Figure 2.

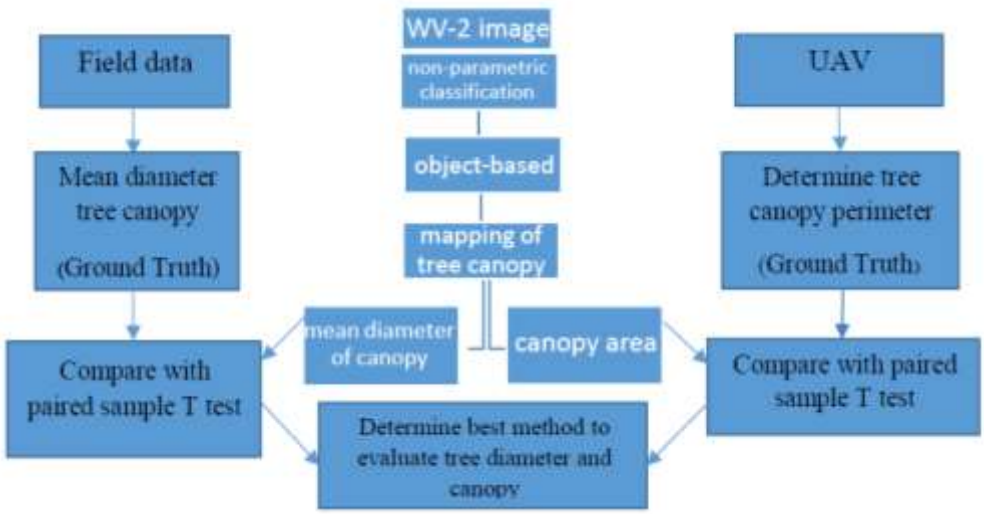

Figure 2. Flowchart of work levels

The Worldview-2 images were georeferenced using the 9-point of three-frequency GPS tracking RTK and static ground reference and the UTM image system was considered. The cloud computing points were taken from ArcGIS10.4 and PCI Geomatica16 software. with an accuracy, the average mean square root (RMSE) of 0.65 pixels was georeferenced using the equation of degree three (ST order polynomia3). Then, Pan sharpening images with a resolution of 0.5 m were created with a combination of polygonal and panchromatic quadrants (Table 1).

Table 1. Characteristics of sensor and four standard bands of WV-2

Wavelength nm	Bands of WorldView-2 sensor
450-800	panchromatic
450-510	blue
510-580	green
630-690	red
770-895	NIR1

In order to inventory the trees perimeter in the forest area, we took pictures of drone images from Phantom 4 Pro. The Phantom 4 Peru is equipped with a one-inch CMOS camera that can capture 20-megapixel quality (Dji, 2016) (Figure 3).

Figure 3. The commercial "ready-to-use" Micro-drones MD 4-200. Payload includes IMU, GPS receiver, downward pointing CIR-modified digital Canon IXUS 100 camera, radio downlink and microprocessor controlled flight control units

2.3. The Nearest neighbor classifier

Classifier of the nearest neighbor (Schowengerdt, 1997): Lists of nonparametric classifications of unknown pixels in accordance to the labels of the neighboring educational vectors in the image space include:

The best neighbor: Labels the nearest pixels surrounding the training pixel.

Nearest k: Assemblies are based on the majority of the training pixel tags near the neighbor k.

The nearest neighbor k is the weighted distance: assigns weights to the closest neighbor k, based on the label of the closest neighboring k instructional pixels, in the opposite proportion to the Euclidean distance of the unknown pixel, and assigns the label to the highest weight of the set.

2.4. Object Based Classification

Pixel Based analysis is usually simple and operates in a comprehensive and general way on the sensors. Although pixels are often not a favorite unit, Measuring is not possible without them. For example, the canopy of separate trees and gap between crowns involves several pixels and creates a spatial self-regulation within objects that we can easily detach in high-resolution images (Woodcock and Strahler, 1987). OBIA seems to search for a "mean" for objects. It searches for objects by segmenting the image into groups of pixels with similar characteristics based on spatial and spatial properties (Benz et al., 2004).

The purpose of the image segmentation is to extract the image objects in the best case according to the scale features, the weight of the inhomogeneity of softness and the compression weight that was performed in the software. These parameters were obtained with ESP and with test and error. Later, the obtained objects enter the classification methods. Multi-resolution segmentation was done

by segmentation process. Using the approach of the nearest neighbor and identifying suitable training samples, the image was classified into two general forest and non-forest classes (Table 2).

Table 2. Weighting for segmentation

Hierarchy	Scale parameter	Color factor	Shape factor	Compactness degree	Softness degree
Level1	10	0.8	0.2	0.7	0.3
Level2	20	0.8	0.2	0.7	0.3

The most basic of the multi-resolution segmentation algorithms is the scale parameter. For the first time Dragut et al. (2010) based on local variations in the multi-scale segmentation algorithm at the time of segmentation and pixel integration used the ESP (Estimation of Scale Parameter), which is the extension of eCognition, and the most appropriate scale for determining the segmentation. If two pixels or the same object are merged, the rate of local variation will decrease, but if two pixels or non-sex objects are merged, the process of local variation changes will increase.

The graph represents the points where the ROC-LV has increased when the pieces were merged and new larger parts were created, which is an appropriate scale for image segmentation. The best scales for our image were 24, 26, 30, 34, 37, 31, 41, 45, 47, 49, 51, 54, 57, 60, 71, 75, 79, 88, and 94 (Figure 4).

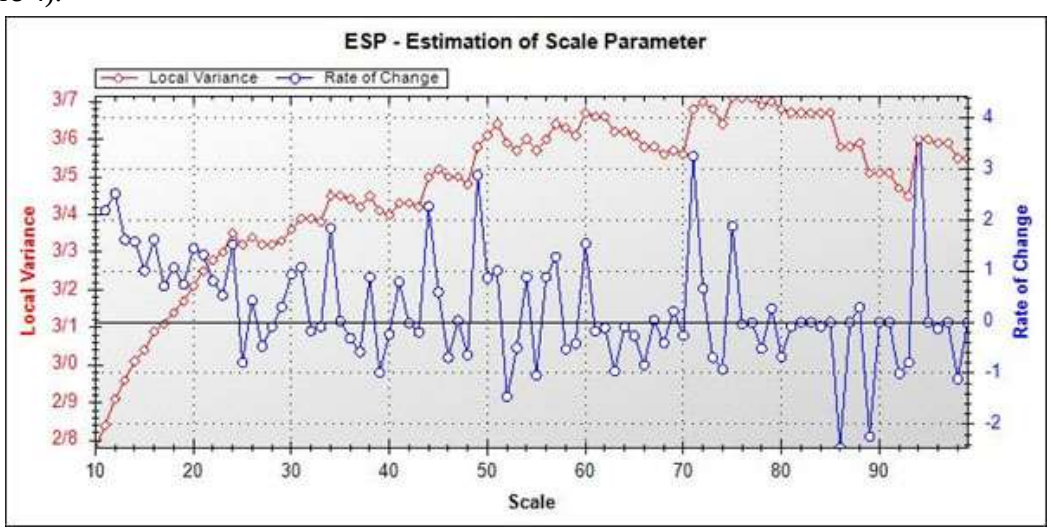

Figure 4. ROC-LV schematic

After selecting the training data, they were arranged in a thematic layer, the TTA mask layer, in the software to be used during the process. The same training data was used for different classification methods and Classification was performed in three ways.

After extracting the forest feature in the three methods, the results were assessed. For this, 100 points were created randomly on the images, and the canopy boundary of these trees was determined from UAV images (Figure 5).

Figure 5. Canopy of 100 determined trees on UAV image for Ground truth

2.5. Accuracy assessment

Accuracy assessment was done in two ways: the usual method, which used Kappa coefficient, and the second method was performed using the AUC method.

2.6. Sampling method for quantitative and qualitative forest characteristics

The study sampling method has been carried out in a systematic approach. A 200x200-meter rectangular grid was overlaid in the image of the region, with 40x40 m rectangular sample pieces discharged into the area. A total of 63 sample plots (36 plots of AbeAnar village and 27 villages of BalehZar village) were measured at each site. In each plot, the considered characteristics of the vegetation included: Recording the diameter of large and small trees, the diameter at breast height (DBH), the tree crown cover, and the health of the tree.

The estimated canopy cover area for BalehZar forest trees on WV-2 and UAV images, the sampling with 200 × 200 square meter network on the ground and satellite images of WV-2 was carried out. In the village of BalehZar 27 plots of 1600 square meters (40 × 40 m) were collected on site 1, and site 2 the village of AbeAnar with 33 plots. In each sample piece, the large and small diameters, the diameter of the breasts and then the crown cover area (equation 1) were measured. The quantitative statistics in the forests of the BalehZar village including the number of samples, mean, standard deviation and standard error in two methods of land cover and WV-2 depiction were presented in Table 1. The results of this study showed that, the sample area was calculated on the basis of equation 1. Then analysis of the canopy cover areas was carried out to the SPSS25 environment (Table 1).

$$\text{Covering the crown surface} = \pi / 4 \times \text{Medium crown diameter} \quad (1)$$

3. Results and discussion

In Figure 6, the results were derived from three types of vector support vector, decision tree, and object-based. As you can see, the quality of the classifications is almost the same. But there are differences in accuracy. The accuracy assessment was done in two ways: the usual method of Kappa coefficient and AUC method. In the accuracy assessment tables, error matrix, overall accuracy, kappa coefficients, manufacturer accuracy, and user precision of each method is presented.

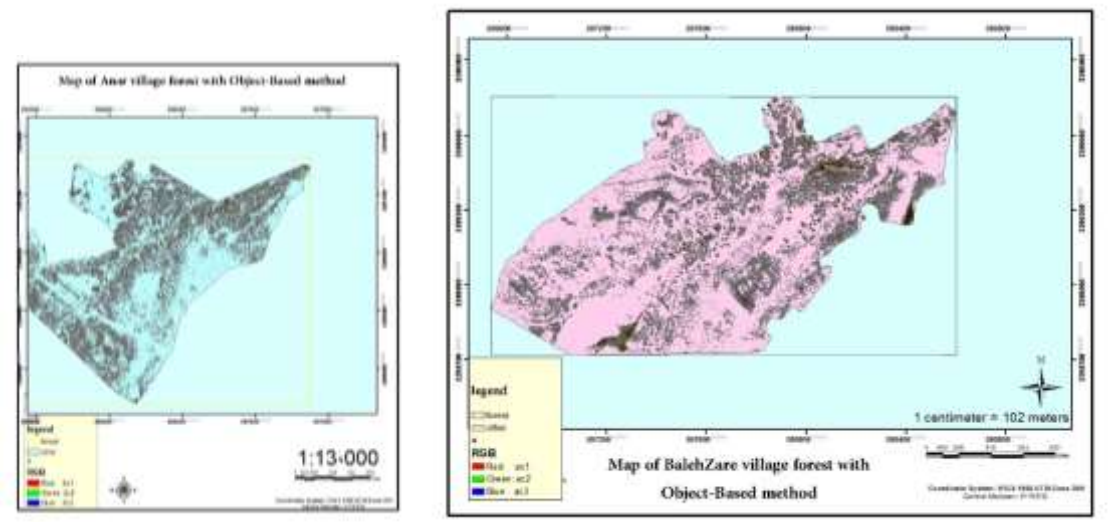

Figure 6. Classification results of the forest feature with object-based algorithm in BalehZare (right image) and Abe Anar sites (left).

3.1. Accuracy assessment of WV-2 canopy cover area with UAV cover

3.1.1. Regression of canopy cover area in BalehZar forests

Data analysis

At first, the normal distribution of data was investigated by Kolmogrov-Smirnov test. The result of the test showed that all data had normal distribution and were significant at 99%level. To compare the canopy coverage obtained from WV-2 satellite imagery and groundbreaking, T-pair test was used at 95% confidence level. The results of the Paired Sample t test between measured forest and image data showed that there was no significant difference between the measurement of canopy coverage in two methods at a significant level of 95% (df = 99, t = 1.984). Figure 8 shows the correctness of the item.

The regression analysis results showed that satellite imagery with an approximate magnitude of 0.95 (R^2 =95%) illustrates the potential for high-resolution WV-2 satellite images (Table 3 and 4 of the statistical model).

In Table 4 of the statistical model, the area of canopy on the ground as an associated variable and canopy area on satellite images is considered as an independent variable. The results of analysis of variance and coefficient test showed that WV-2 satellite images can be used to estimate the canopy surface. The point cloud is plotted in Figure 7. In which the X axis is the crown surface on the satellite image and the Y axis is the crown surface on the ground.

As a result, the WV-2 images can be used instead of land surveying to calculate the area of the canopy of forests, which is consistent with the results of the researchers.

Table 3a. Statistical data of the canopy cover of trees in the forests of BalehZar

Variable of canopy cover percent in forest inventory of BalehZar	Inventory method with UAV	Object-based WV-2 satellite images
Samples number	100	100
Mean (m^2)	68.48	66.70
Standard deviation (m^2)	41.63	40.84
Standard error (m^2)	4.16	4.08

Table 3b. Statistical data of the canopy cover of trees in the forests of AbeAnar

Variable of canopy cover percent in forest inventory of BalehZar	Inventory method with UAV	Object-based WV-2 satellite images
Samples number	100	100
Mean (m^2)	44.62	44.89
Standard deviation (m^2)	28.9	28.68
Standard error (m^2)	2.89	2.87

Table 4. Statistical model of the canopy surface covering the satellite imagery of WV-2 and UAV of forests of the village of Balehazar and AbeAnar

Name	Model	Coefficient R^2	Coefficient r	Model of statistic
Object-based of Balehazar	Linear	0.953	0.976	Y = 2.11 + 0.995X
Object-based of AbeAnar	Linear	0.998	0.999	Y = -0.579 + 1.007X

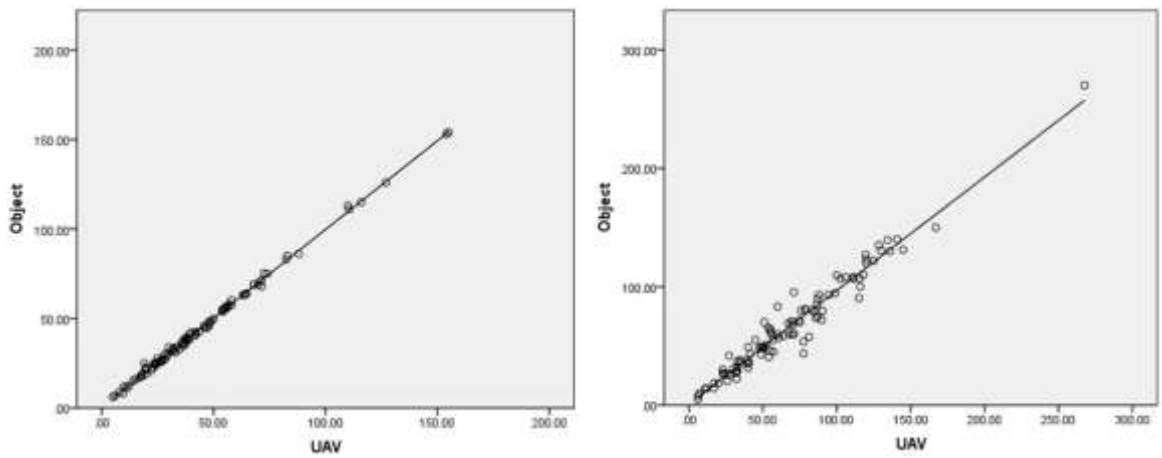

Figure 7. Evaluation of the accuracy of the canopy in Object-Based classification in satellite imagery WV-2 and UAV image in the forests of the village of Balehazar and AbeAnar.

3.2. Evaluation of the accuracy of the diameter of the canopy in satellite imagery WV-2 with the ground in the forests of the village of Balehazar and AbeAnar.

For accuracy evaluation of the diameter of the canopy in satellite imagery WV-2 with ground points in the forests of the village of Balehzar and AbeAnar, initially, the normal distribution of data was investigated by Kolmogrov-Smirnov test. The result of the test showed that all data were normal distribution and are significant at 99% level.

To compare the average diameter of the canopy obtained from WV-2 satellite imagery and ground-level random sampling, t-test was used at 95% confidence level. The results of Paired Sample t test between measured forest and image data showed that there was no significant difference between the measurement of canopy coverage in two methods at a significant level of 95% (df = 99, t = 1.984). Figure 8 shows the correctness of the item.

The regression analysis results showed that satellite images with an approximate coefficient of 0.95 (R2 =95%) indicate that the average diameter of the trees canopy can be obtained with high accuracy from WV-2 satellite images of (Table 5 and 6 of the statistical model).

Table 5a. Statistical data of Medium diameter of canopy of trees in BalehZar forest

	Mean(m)	Samples number	Standard deviation (m)	Standard error (m)
Medium diameter of canopy on ground	9.1279	100	2.959	0.295
Medium diameter of canopy in object-based	8.9876	100	2.733	0.273

Table 5b. Statistical data of Medium diameter of canopy of trees in AbeAnar forest

	Mean (m)	Samples number	Standard deviation (m)	Standard error (m)
Medium diameter of canopy on ground	7.3707	100	2.324	0.232
Medium diameter of canopy in object-based	7.2800	100	2.281	0.228

Table 6. Statistical model of the medium diameter of canopy surface covering in the satellite imagery of WV-2 and ground of forests of the village of Balehazar and AbeAnar

Name	Model	Coefficient R^2	Coefficient r	Model of statistic
Object-based of Balehazar	Linear	0.942	0.888	Y = -0.028 + 1.020X
Object-based of AbeAnar	Linear	0.958	0.918	Y = 0.256 + 0.976X

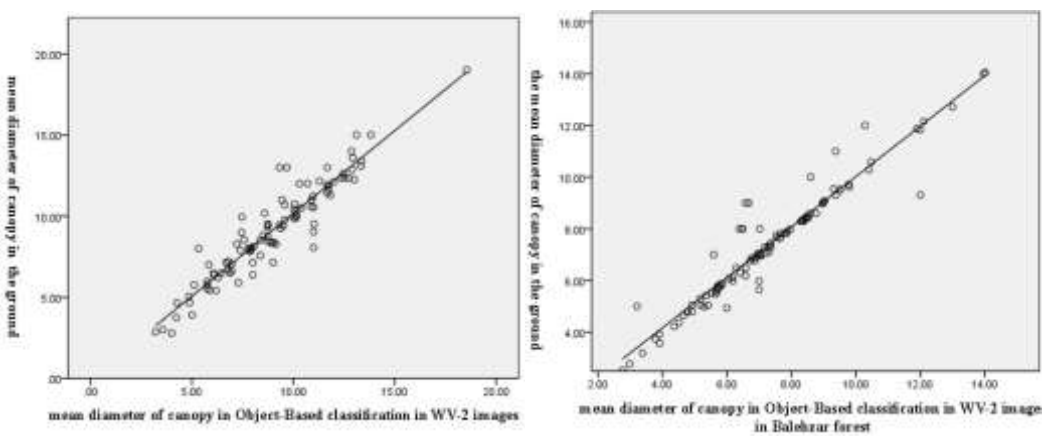

Figure 8. Assessing the accuracy of the mean diameter of canopy in Object-Based classification in WV-2 images and the ground of the trees in the forests of the village of Balehazar and AbeAnar.

3.3. Assessing the accuracy of the crown cover in WV-2 images with the height of the trees in the forests of the village of Balehazar and AbeAnar

At first, the normal distribution of data was investigated by Kolmogrov-Smirnov test. The result of the test showed that all data had normal distribution and are significant at 99% level. The regression analysis results showed that satellite images with a good explanation coefficient of 0.68 (R^2 = 68%) indicated that height can be obtained with proper accuracy from satellite images of WV-2 (Table 7 of the statistical model and Figure 9).

Table 7. Statistical model of canopy surface in WV-2 images and tree height in the forests of the village of Balehzar and AbeAnar

Name	Model	Coefficient R^2	Coefficient r	Model of statistic
Object-based of Balehazar	Linear	0.696	0.828	Y = 5.117 + 0.056X
Object-based of AbeAnar	Linear	0.686	0.826	Y = 4.112 + 0.069X

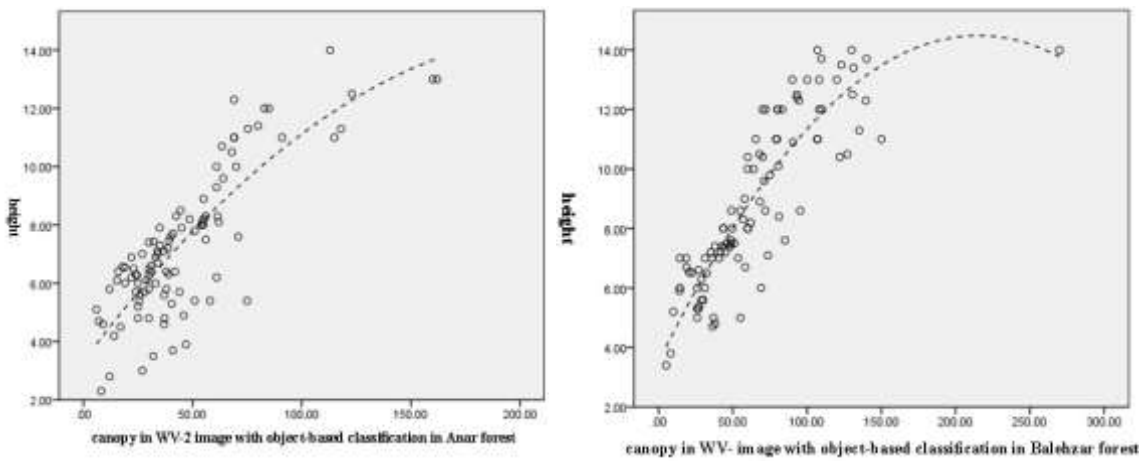

Figure 9. Assessing the accuracy of the crown cover in Object-Based classification in WV-2 images and the height of the trees in the forests of the village of Balehazar and AbeAnar.

This study is one of the first studies to estimate and extract single-tree parameters from high-resolution satellite imagery. A high level of accuracy was obtained in estimating canopy cover, canopy diameter and height of trees with satellite imagery. In the object-based method, the training samples were taken as TTA mask (Training & Test Area MASK) in order to evaluate the accuracy of the classification using spectral data, and the Kappa coefficient was 0.974 (0.967 in the AbeAnar village and 0.981 in the village of BalehZar), with an overall accuracy of 98.82% (99.14% in the AbeAnar village and 98.51% in the village of BalehZar) was obtained in the classification error matrix. Therefore, the base object method, the support vector method, and decision tree method were respectively the highest classification accuracy in the study area (Table 8).

Table 8. Comparison of Object-Based classification in sites with matrix

Object-Based	Classification accuracy
0.974	Kappa coefficient
98.82	Overall accuracy (%)

4. Conclusions

The study found that WV-2 data can be used to predict the tree parameters such as crown cover, bream diameter, tree height, tree number and biomass in the Zagros forests of Iran. The height of the trees can be obtained directly from the digital surface model using drone images. The crown cover and canopy diameter have a very high correlation with the terrestrial data. The combination of drone data with the satellite data from WV-2 has been useful to describe the biodiversity and monitoring the forest biodiversity. OBIA is widely used for forest remote-sensing research (Chubey et al., 2006; Desclee et al., 2006; Hay et al., 2005; Wulder et al., 2008). It has been successful in forest tree studies (Conchedda et al., 2007; Myint et al., 2008; Wang et al., 2004a). The object-based method in the extraction of single forest trees using spectral data is more potent than pixel-based methods.

According to the obtained results using WV-2 satellite spectral data in estimating the canopy surface, it was determined that these data are capable of estimating the quantitative characteristics of the crown cover of oak forests and extraction of single trees in the study area with proper accuracy.

There is a good correlation between the diameters of the crown of trees with ground measurements which indicates that extracting of the data using drone is excellent. The R coefficient result for the crown diameter of the forest trees was 0.85 in average, which is consistent with the results of Shrestha and Wynne (2012). They also obtained a correlation coefficient of 0.9 for the crown diameter.

As Pande-Chhetri et al. (2017) found in the estimation of wetland vegetation with WV-2 images, the object-based method was superior to the pixel-based method. In the current research, the object-based classification is better than other classifications, as the study results indicates that the SVM classification has a superior performance over the tree. The results obtained is compatible with Thanh Noi (2018), Raczko et al. (2017), Pande-Chhetri et al. (2017), Qian et al. (2015), Shafri and Ramle (2009), Shao et al. (2012), Kim et al. (2012), Amami et al. (2015), Ghasemian and Akhondzadeh (2016).

The very high correlation between the estimation of the canopy of the satellite images and terrestrial shows that one can estimate The canopy parameter from the images. The comparison between the estimated crown cover with the crown covering the ground surface in all the three methods shows that there is no significant difference between ground data and satellite image estimation at 5% significance level. This indicates that the nonparametric models used in the study have no significant difference with ground reality.

Considering other researchers' research on the extraction of features using algorithms, it is shown that the present study is of desirable accuracy.

Forecast models of this study, although they are surveyed for trees in Zagros forests, can be used for other forest levels with similar climate and species composition. This kind of forecast with drone images will help to properly assess the quality of carbon stored trees on the level of single trees. Further studies should be developed to predict biophysical parameters such as leaf area index,

stem volume, etc. Management tables for forest planners such as forestry activities, disaster vulnerability, and age class are useful for forest trees. The functionality of these models can improve inappropriate data from other forest levels and if the area is not accessible, these equations can estimate trees from forest levels instead of being present in the field.

References

Amami, R., Ayed, D. B., & Ellouze, N. (2015). An Empirical comparison of SVM and some supervised learning algorithms for vowel recognition. International Journal of Intelligent Information Processing (IJIIP), 3(1).

Allen, C. D., Macalady, A. K., Chenchouni, H., Bachelet, D., McDowell, N., Vennetier, M., ... & Gonzalez, P. (2010). A global overview of drought and heat-induced tree mortality reveals emerging climate change risks for forests. Forest Ecology and Management, 259(4), 660–684.

Benz, U. C., Hofmann, P., Willhauck, G., Lingenfelder, I., & Heynen, M. (2004). Multi-resolution, object-oriented fuzzy analysis of remote sensing data for GIS-ready information. ISPRS Journal of Photogrammetry and Remote Sensing, 58(4), 239-258.

Breshears, D. D., Cobb, N. S., Rich, P. M., Price, K. P., Allen, C. D., Balice, R. G., … & Andrson, J. J. (2005). Regional vegetation die-off in response to global-change-type drought. Proceedings of the National Academy of Sciences, 102(42), 15144–15148.

Carnicer, J., Coll, M., Ninyerola, M., Pons, X., Sánchez, G., & Peñuelas, J. (2011). Widespread crown condition decline, food web disruption, and amplified tree mortality with increased climate change-type drought. Proceedings of the National Academy of Sciences of the United States of America, 108, 1474–1478.

Chubey, M. S., Franklin, S. E., & Wulder, M. A. (2006). Object-based analysis of Ikonos-2 imagery for extraction of forest inventory parameters. Photogrammetric Engineering and Remote Sensing, 72(4), 383-394.

Clark, D.B., Castro, C.S., Alvarado, L.D.A., & Read, J.M. (2004a). Quantifying mortality of tropical rain forest trees using high spatial- resolution satellite data, Ecological Letters, 7:52–59.

Clark, D.B., Read, J.M., Clark, M.L., Cruz, A.M., Dotti, M.F., & Clark, D.A. (2004b). Application of 1-m and 4-m resolution satellite data to ecological studies of tropical rain forests, Ecological Applications, 14:61–74.

Conchedda, G., Durieux, L., & Mayaux, P. (2007). Object-based monitoring of land cover changes in mangrove ecosystems of Senegal. In 4th International Workshop on the Analysis of Multi-Temporal Remote Sensing Images, 44-49. Louvain, Belgium, IEEE.

Desclee, B., Bogaert, P., & Defourny, P. (2006). Forest change detection by statistical object-based method. Remote Sensing of Environment, 102(1-2), 1-11.

Dji. (2016). PHANTOM 4 User Manual. Chine.

Drăguţ , Dirk Tiede & Shaun R. Levick. 2010. ESP: a tool to estimate scale parameter for multiresolution image segmentation of remotely sensed data. International Journal of Geographical Information Science.

Franklin, S. E. (2001). Remote sensing for sustainable forest management. CRC press. Lewis Publishers, New York, pp 296–300.

Ghasemian, N., & Akhondzadeh, M. (2016). Comparison of Methods of Artificial Neural Networks, Support Vector Machine and Decision Tree to Identify Clouds in Landsat 8 Satellite Images. GEJ. 2016, 7(4), 25-36. (In Persian).

Gillis, M. D., & Leckie, D. G. (1993). Forest inventory mapping procedures across Canada (Vol. 114).

Gougeon, F. A., & Leckie, D. G. (1999). Forest regeneration: Individual tree crown detection techniques for density and stocking assessment. In Proceedings of the International Forum on Automated Interpretation of High Spatial Resolution Digital Imagery for Forestry (pp. 10-12). Canadian Forest Service, Pacific Forestry Center Victoria, BC.

Gong, P., Biging, G. S., Lee, S. M., Mei, X., Sheng, Y., Pu, R., Xu, B., Schwarz, K., & Mostafa, M. (1999). Photo ecometrics for forest inventory. Geographic Information Science, 5(1), 9–14.

Hay, G. J., Castilla, G., Wulder, M. A., & Ruiz, J. R. (2005). An automated object-based approach for the multiscale image segmentation of forest scenes. International Journal of Applied Earth Observation and Geoinformation, 7(4), 339-359.

Juniati, E., & Arrofiqoh, E. N. (2017). Comparison of Pixel-Based and Object-Based classification using parameters and non-parameters approach for the pattern consistency of multiscale land cover. The International Archives of the Photogrammetry, Remote Sensing and Spatial Information Sciences, Volume XLII-2/W7, 2017.

Kim, J., Kim, B. S., & Savarese, S. (2012). Comparing image classification methods: K-nearest-neighbor and support-vector-machines. Applied Mathematics in Electrical and Computer Engineering. Harvard, Cambridge. USA.

Kelly, M., Shaari, D., Guo, Q. H., & Liu, D. (2004). A comparison of standard and hybrid classifier methods for mapping hardwood mortality in areas affected by "sudden oak death," Photogrammetric Engineering & Remote Sensing, 70(11), 1229–1239.

Koch, B., Heyder, U., & Weinacker, H. (2006). Detection of individual tree crowns in airborne lidar data. Photogrammetric Engineering & Remote Sensing, 72(4), 357–363.

Laasasenaho, J. (1982). Taper Curve and Volume Functions for Pine, Spruce and Birch. Commun. Inst. Forest Fenn. 108, 1–74.

Leckie, D. G., Yuan, X., Ostaff, D. P., Piene, H., & Maclean, D. A. (1992). Analysis of high spatial resolution multispectral MEIS imagery for spruce budworm damage assessment on a single tree basis. Remote Sensing of Environment, 40(2), 125–136.

Levesque, J., & King, D. J. (1999). Airborne digital camera image semivariance for evaluation of forest structural damage at an acid mine site. Remote Sensing of Environment, 68(2), 112–124.

Myint, S. W., Giri, C. P., Wang, L., Zhu, Z. L., & Gillette, S. C. (2008). Identifying mangrove species and their surrounding land use and land cover classes using an object-oriented approach with a lacunarity spatial measure. GIScience & Remote Sensing, 45(2), 188-208.

Niphadkar, M., Nagendra, H., Tarantino, C., Adamo, M., & Blonda, P. (2017). Comparing Pixel and Object-Based approaches to map an understory invasive shrub in tropical mixed forests. Frontiers in Plant Science, 8, 892.

Okojie, J. (2017). Assessment of forest tree structural parameter extractability from optical imaging UAV dataset, In Ahaus Germany.

Pande-Chhetri, R., Abd-Elrahman, A., Liu, T., Morton, J., & Wilhelm, V. L. (2017). Object-based classification of wetland vegetation using very high-resolution unmanned air system imagery. European Journal of Remote Sensing, 50(1), 564–576.

Phillips, O. L., Aragão, L. E. O. C., Lewis, S. L., Fisher, J. B., Lloyd, J., López-González, G., … & Van Der Heijden, G. (2009). Drought sensitivity of the Amazon rainforest. Science, 323(5919), 1344–1347.

Qian, Y., Zhou, W., Yan, J., Li, W., & Han, L. (2015). Comparing machine learning classifiers for Object-Based land cover classification using very high resolution imagery. Remote Sensing, 7(1), 153-168.

Raczko, E., & Zagajewski, B. (2017). Comparison of support vector machine, random forest and neural network classifiers for tree species classification on airborne hyperspectral APEX images. European Journal of Remote Sensing, 50(1), 144-154.

Repola, J. (2009). Biomass equations for Scots pine and Norway spruce in Finland. Silva Fenn. 43, 625–647.

Schowengerdt, R. A. (1997). Remote Sensing: Models and Methods for Image Processing. Academic, San Diego, USA.

Sedliak, M., Sačkov, I., & Kulla, L. (2017). Classification of tree species composition using a combination of multispectral imagery and airborne laser scanning data. Central European Forestry Journal, 63(1), 1–9.

Shrestha, R., & Wynne, R. H. (2012). Estimating biophysical parameters of individual trees in an urban environment using small footprint discrete-return imaging Lidar. Remote Sensing, 4(2), 484-508.

Shafri, H. Z. M., & Ramle, F. S. H. (2009). A Comparison of Support Vector Machine and Decision Tree Classifications Using Satellite Data of Langkawi Island. Information Technology Journal, 8(1), 64-70.

Shao, Y., & Lunetta, R. S. (2012). Comparison of support vector machine, neural network, and CART algorithms for the land-cover classification using MODIS time-series data. ISPRS Journal of Photogrammetry and Remote Sensing, 70, 78-87.

Thanh Noi, P., & Kappas, M. (2018). Comparison of random forest, k-nearest neighbor, and support vector machine classifiers for land cover classification using Sentinel-2 imagery. Sensors, 18(1), 18.

Van Mantgem, P. J., Stephenson, N. L., Byrne, J. C., Daniels, L. D., Franklin, J. F., Fulé, P. Z., & Veblen, T. T. (2009). Widespread increase of tree mortality rates in the western United States. Science, 323(5913), 521–524.

Wang, L., Sousa, W. P., & Gong, P. (2004a). Integration of object-based and pixel-based classification for mapping mangroves with IKONOS imagery. International Journal of Remote Sensing, 25(24), 5655-5668.

Wen, D., Huang, X., Liu, H., Liao, W., & Zhang, L. (2017). Semantic Classification of Urban Trees Using Very High Resolution Satellite Imagery. IEEE Journal of Selected Topics in Applied Earth Observations and Remote Sensing, 10(4), 1413-1424.

Woodcock, C. E., & Strahler, A. H. (1987). The factor of scale in remote sensing. Remote Sensing of Environment, 21(3), 311-332.

Wulder, M. A., White, J. C., Hay, G. J., & Castilla, G. (2008). Towards automated segmentation of forest inventory polygons on high spatial resolution satellite imagery. The Forestry Chronicle, 84(2), 221-230.

Zoehrer, F. (1980). Forstinventur. Ein Leitfaden fu¨ r Studium und Praxis. Pareys Studientexte 26. Verlag Paul Parey. Hamburg und Berlin. 207 pp.

Available online at www.jrors.ir

JRORS
Journal Of Radar and Optic Remote Sensing

Journal Of Radar and Optic Remote Sensing

JRORS 2 (2018) 24–37

Performance evaluation of FFT_PCA Method based on dimensionality reduction algorithms in improving classification accuracy of OLI data

Parviz Zeaiean Firooz Abadi[a*], Hasan Hasani Moghaddam[b]

[a] *Associated professor of remote sensing and GIS, Faculty of Geography, Kharazmi University*
[b] *MA of remote sensing and GIS, Kharazmi University*

Received 23 September 2018; revised 12 November 2018; accepted 13 November 2018

Abstract

Fusions of panchromatic and multispectral images create new permission to gain spatial and spectral information together. This paper focused on hybrid image fusion method FFT-PCA, to fuse OLI bands to apply Dimensionality Reduction (DR) methods (PCA, ICA and MNF) on this fused image to evaluate the effect of these methods on final classification accuracy. A window of OLI images from Ardabil County was selected to this purpose and preprocessing method like atmospheric and radiometric correction was applied on this image. Then panchromatic (band8) and multispectral bands of OLI were fused with FFT-PCA method. Three dimensionality reduction algorithms were applied on this fused image and the training data for classification were selected from DRs Output. A total of eight classes include bare land, rich range land, water bodies, settlement, snow, agricultural land, fallow and poor range land were selected and classified with support vector machine algorithm. The results showed that classification based on dimensionality reduction algorithms was quite good on OLI data classification. Overall accuracy and kappa coefficient of classification images showed that ICA, PCA and MNF methods 86.9%, 89%, 96.8% and 0.84, 0.91, 0.96 respectively. The MNF based image classification has higher classification accuracy between two others. PCA and ICA have lower accuracy than MNF respectively.

Keywords: Hybrid fusion, FFT-PCA, Dimensionality reduction algorithms, Support vector machine.

* Corresponding author. Tel: +98-9123903621.
E-mail address: zeaiean@khu.ac.ir.

1. Introduction

Remote sensed data have been used to extract relevant information on various natural recourses and environments (Kumar Singla et al., 2018). Land cover is critical information to various land management and scientific application (Liu, 2017). There are large numbers of methods developed and applied to increase total accuracy of land use/cover mapping from satellite imagery (Hasani Moghaddam et al., 2018). Fusion of panchromatic and multispectral bands, is the most critical way to increase information extraction accuracy (Vivekan et al., 2014; Unlusoy, 2013). In recent years, Hybrid image fusion methods were implemented for the fusion of multi resolution images (Dhavan and Garg, 2014). PCA+SWT (Kaur, 2016), DDCT+PCA (Mamachan and Baby, 2015), FFT-HIS (Yusuf et al., 2013), and FFT-PCA (Bashirpour et al., 2017), Are the most important hybrid methods that have been used in recent researches. One of the most effective hybrid methods is FFT_PCA that also preserve spectral and spatial information of the multispectral and panchromatic images as well as original inputs (Bai et al., 2015). The reduction of the dimension of fused image is an important way to perform faster classification. The dimensionality reduction algorithms can efficiently brought down the data to a much smaller number of variables without a significant loss of information (Sorzano et al., 2014). PCA is one of the effective dimensionality reduction methods that tries to find a new coordinate system in which the input data can be expressed with many less variables without a significant error (Sorzano et al., 2014). Another method for dimensionality reduction (DR) is MNF that provides a linear transformation of data, in which the noise data values are lower in the initial conversions, and the amount of noise increases further components (Hasani Moghaddam, 2017). The ICA DR method has received considerable interest in recent years. The key idea of ICA assumes that data are linearly mixed with a set of separate independent sources and demix this signal sources according to their statistical independent measured by mutual information (Wang and Chang, 2006).

Wang and Chang (2006), worked on application of independent analysis in hyper spectral images. The study illustrates that ICA dimensionality reduction methods uses mutual information as a criterion to measure data statistical independency that exceeds second order statistics. The results of the study showed that ICA-DR provide advantages over the PCA-DR and MNF-DR.

Sahisi and Krishna (2016) have done researches in performance evaluation of dimensionality reduction techniques on CHRIS hyper spectral data for surface discrimination title. In this study, they used MNF, PCA and ICA DR methods. They used Hybrid dimensionality reduction method for extracting the concrete materials from the CHRIS hyper spectral data. SAM and SID classifier were used to classify surface materials. The results showed that, SAM classifier gave the best results with an accuracy improvement of 10% after adapting the hybrid method.

Arslan et al., (2017), compared performance of classification methods for a hyper spectral images data set in view of dimensionality reduction methods. Among the DR methods, ICA, PCA and MNF were used in this study. Four classification algorithms including MLC, MD, SAM and SVM were used to evaluate more accurate method among them. The results showed that MLC algorithm

generally performed better than the other classifier while the SAM exhibited significantly lower accuracies in the experiments.

Wang and chang(2017), have studied on unsupervised feature extraction for hyper spectral images by using combination low rank representation and locally linear embedding. They used MNF, PCA and ICA methods for dimensionality reduction of data. The results showed that the PCA method has better performance by 0.77 kappa coefficient and ICA has lower performance by 0.70 kappa coefficient.

The aim of this study is to fused panchromatic and multispectral OLI bands with FFT_PCA method and then apply DR algorithms to this fused image to evaluate the effect of these DR methods on Support Vector Machine of OLI classification accuracy.

2. Material and Methods

2.1. Study area

An area of 2565.838 square kilometer, in Ardabil county is located between 37.45- 39.42 northing latitudes and 47.30-48.55 easting longitudes at northwest of Iran (Ghasemlounia and Sedaghat Herfe, 2017). In this region, the lowest elevation in Ardebil plain is 1294 meters and the highest elevation (Sabalan peak) is 4811 meters above sea level. The average rainfall and annual temperature are 318.4 mm and 14.87°C respectively (Torahi et al., 2016). Figure (1), shows the geographic location of Ardabil county.

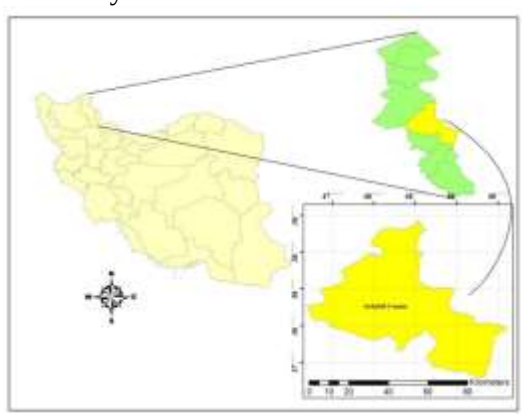

figure 1. Geographic location of study area

2.2. Satellite data used

The OLI sensor provides nine spectral bands (1-9) and TIRS provides two spectral bands (10-11), as shown in Table 1. Seven bands from band 2 to band 7 of OLI are consistent with the TM and ETM+ sensors. The new two spectral bands, band 1 and band 9 allow measuring water resources and coastal zone investigation and improving the detection of cirrus clouds. TIRS conducts thermal

imaging which can be applicable to evapotranspiration rate measure for water management (Chul ko et al., 2015).

Table 1. Wavelength and spatial resolution of the Landsat 8 OLI and TIRS (Knight and Kvaran, 2014 ; Alhirmizy, 2015)

Band	Wavelength Range(μm)	Spatial resolution(m)
OLI 1	0.433-0.453 (Coastal/aerosol)	30
OLI 2	0.450-0.515 (blue)	30
OLI 3	0.525-0.600 (green)	30
OLI4	0.630-0.680 (green)	30
OLI 5	0.845-0.885 (Near-IR)	30
OLI 6	1.560-1.660 (SWIR-1)	30
OLI 7	2.100-2.300(SWIR-2)	30
OLI 8	0.500-0.680 (Pan)	15
OLI 9	1.360-1.390 (Cirrus)	30
TIRS 10	10.30-11.30 (LWIR-1)	100
TIRS 11	11.50-12.50 (LWIR-2)	100

2.3. Methods

The image of Landsat 8-OLI were downloaded from USGS explorer and some image preprocessing analysis such as atmospheric and radiometric corrections were performed on the image before fusing panchromatic and multispectral bands. The FFT-PCA method was used to fuse OLI bands to get 15 meter resolution. Then three DR methods including PCA, ICA and MNF were performed on this fused image and results were classified with Support Vector Machine (SVM) algorithm. The performance of each DR algorithms was evaluated to improve the accuracy of classification of final images using overall accuracy and Kappa coefficient.

2.3.1. Principal Component Analysis (PCA)

PCA is a common technique for DR and finding pattern in high dimension data, Proposed by Pearson in 1901. It is based on computation of low-dimensional representation of a high-dimensional dataset that maximizes the total distribution which is optimal in reconstruction (Ping et al., 2017). The following describes the description in steps:

Step 1. The m samples can be represented by a set of $\Psi = \{X_1, X_2, \ldots, X_m\}$. For each sample, which has n indicators, it can be described as $\Psi = \{X_1, X_2, \ldots, X_m\}$ for $i \in \{1, 2, \ldots, m\}$, and then a m*n matrix X can be constructed with all the observation as follows:

$$X = \begin{bmatrix} X_1 \\ X_2 \\ \vdots \\ X_m \end{bmatrix} = \begin{bmatrix} X_{11} & X_{12} & \cdots & X_{1n} \\ X_{21} & X_{22} & \cdots & X_{2n} \\ \vdots & \vdots & \vdots & \vdots \\ X_{m1} & X_{m2} & \cdots & X_{mn} \end{bmatrix}. \quad (1)$$

Then based on Matrix X, the standardized matrix X* can be obtained by the following procedure.

$$X^* = \begin{bmatrix} X^*_1 \\ X^*_2 \\ \vdots \\ X^*_m \end{bmatrix} = \begin{bmatrix} X^*_{11} & X^*_{12} & \cdots & X^*_{1n} \\ X^*_{21} & X^*_{22} & \cdots & X^*_{2n} \\ \vdots & \vdots & \vdots & \vdots \\ X^*_{m1} & X^*_{m2} & \cdots & X_{mn} \end{bmatrix} \quad (2)$$

Where $X^*_i = (x^*_{i1}, x^*_{i2}, \ldots, x^*_{in})$, $x^*_{ij} = (x_{ij} - \bar{x}_j) / \sqrt{\mathrm{var}(x_j)}$ is the value of the element in the X* after standardizing, $\bar{x}_{ij} = (1/n)\sum_{i=1}^{n} x_{ij}$ and $\mathrm{var}(x_j) = (1/(n-1))\sum_{i=1}^{n} (x_{ij} - \bar{x}_j)^2$ is the average value and the variance of the jth column of matrix X respectively, for $i \in \{1, 2, \ldots, m\}$ and $j = \{1, 2, \ldots, n\}$.

Step 2. Therefore, the correlation matrix R based on the matrix X* can be obtained.

$$R = \begin{bmatrix} r_{11} & r_{12} & \cdots & r_{1n} \\ r_{21} & r_{22} & \cdots & r_{2n} \\ \vdots & \vdots & \vdots & \vdots \\ r_{n1} & r_{n2} & \cdots & r_{nn} \end{bmatrix} \quad (3)$$

Where the value of element r_{ij} in the matrix R can be calculated as follows:

$$r_{ij} = \frac{\sum_{k=1}^{m} (x^*_{ki} - \bar{x}^*_i)(x^*_{kj} - \bar{x}^*_j)}{\sqrt{\sum_{k=1}^{m} (x^*_{ki} - \bar{x}^*_i)^2 \sum_{k=1}^{m} (x^*_{kj} - \bar{x}^*_j)^2}} \quad (4)$$

Where $\bar{x}^*_i = (1/n)\sum_{j=1}^{n} x^*_{ij}$, for $i \in \{1, 2, \ldots, n\}$ and $j \in \{1, 2, \ldots, n\}$.

Step 3. The n eigenvalues $\lambda_1 \geq \lambda_2 \geq \ldots \geq \lambda_n > 0$ of matrix R and the corresponding n eigenvectors $a_1, a_2, \ldots, a_n$ can be obtained,

$$a_1 = \begin{bmatrix} a_{11} \\ a_{21} \\ \vdots \\ a_{n1} \end{bmatrix} \quad a_2 = \begin{bmatrix} a_{12} \\ a_{22} \\ \vdots \\ a_{n2} \end{bmatrix}, \quad a_n = \begin{bmatrix} a_{1n} \\ a_{21} \\ \vdots \\ a_{nn} \end{bmatrix} \quad (5)$$

N principal components is obtained:

$$F_i = a_{1i} \times X^*_1 + a_{2i} \times X^*_2 + \ldots + a_{ni} \times X^*_m \,, (\mathrm{i} = 1, 2, \ldots, \mathrm{n}) \,. \tag{6}$$

Step 4. Compute the contribution rate CR_i and the accumulative contribution rate ACR_i of each principal component $F_i \,(\mathrm{i} = 1, 2, \ldots, \mathrm{n})$, respectively:

$$\begin{aligned} CR_i &= \frac{\lambda_i}{\sum_k^n = 1^{\lambda k}} \,, \\ A\,CR_i &= \sum_{k=1}^{i} CR_k \end{aligned} \tag{7}$$

Usually the top t principal components are retained. $F_1 F_2, \ldots, \mathrm{F}_t$, which correspond to the eigenvalues $\lambda_1, \lambda_2, \ldots, \lambda_t$, and the corresponding accumulated contribution rate should satisfy that $A\,CR - t \geq 85\%$.

Step 5. Through plugging the elements in the matrix X* into the expression of t principal components, the score matrix F can be obtained.

$$F = \begin{bmatrix} F_{11} & F_{12} & \cdots & F_{1t} \\ F_{21} & F_{22} & \cdots & F_{2t} \\ \vdots & \vdots & \vdots & \vdots \\ F_{m1} & F_{m2} & \cdots & F_{mt} \end{bmatrix} , \tag{8}$$

Where $F_{ij} = a_{1j} x^*_{j1} + a_{2j} x^*_{j2} + \ldots + a_{ni} x^*_{jn}$ for $i \in \{1, 2, \ldots, m\}$ and $j \in \{1, 2, \ldots, t\}$.

Therefore, the original matrix X has been transformed into matrix F that has reduced dimensionally, while not losing much information of the original data.

Step 6. The score matrix F= $\left[F_{ij}\right] m \times t$ is a $m \times t$ matrix, the i^{th} samples total points (TP), $TP_i = \sum_j^t = 1 \, F_{ij} \times CR_j$ can be obtained, where CR_j is the j^{th} eigenvalues contribution rate.

2.3.2. Fast Fourier Transform

The Fast Fourier Transform (FFT) is used as a noise reduction mechanism during image processing. The FFT is a computational efficient algorithm used to compute the Discrete Fourier Transform (DFT) and its inverse (IDFT). The FFT algorithm reduces the computational burden to (ONlogN) arithmetic operations. The FFT is a computational efficient method of generating a Fourier transform (Asiedu et al., 2016).

The first stage in execution of FFT during image processing is to compute the Discrete Fourier Transform. The DFT of a column vector, m_{jk} is represented mathematically as:

$$m^*_{jk} = DFT\left\{m_{jk}\right\} = \sum_{r=0}^{p-1} m_{jk} e^{-i(2\pi sr/p)} \,, \tag{9}$$

Where $s = 0, 1, \ldots, p - 1, \; j = 1, 2, \ldots, \mathrm{n}$ and $i = \sqrt{-1}$.

Where m_{jk} is the k[th] column of the image matrix. For an image matrix of order 4, $p=4$ and $s=0,1,2,3$. The DFT becomes;

$$\begin{aligned} m^*_{j0k} &= m_{j0k}e^{-0.ip/2}+m_{j1k}e^{-0.ip/2}+m_{j2k}e^{-0.ip/2}+m_{j3k}e^{-0.ip/2},\\ m^*_{j1k} &= m_{j0k}e^{-0.ip/2}+m_{j1k}e^{-1.ip/2}+m_{j2k}e^{-2.ip/2}+m_{j3k}e^{-3.ip2},\\ m^*_{j2k} &= m_{j0k}e^{-0.ip/2}+m_{j1k}e^{-2.ip/2}+m_{j2k}e^{-4.ip/2}+m_{j3k}e^{-6.ip/2},\\ m^*_{j3k} &= m_{j0k}e^{-0.ip/2}+m_{j1k}e^{-3.ip2}+m_{j2k}e^{-6.ip/2}+m_{j3k}e^{-9.ip/2}. \end{aligned} \quad (10)$$

Therefore,

$$\begin{bmatrix} m^*_{j0k}\\ m^*_{j1k}\\ m^*_{j2k}\\ m^*_{j3k} \end{bmatrix} = \begin{bmatrix} e^{-0.i\pi/2} & e^{-0.i\pi/2} & e^{-0.i\pi/2} & e^{-0.i\pi/2}\\ e^{-0.i\pi/2} & e^{-1.i\pi/2} & e^{-2.i\pi/2} & e^{-3.i\pi2}\\ e^{-0.i\pi/2} & e^{-2.i\pi/2} & e^{-4.i\pi/2} & e^{-6.i\pi/2}\\ e^{-0.i\pi/2} & e^{-3.i\pi2} & e^{-6.i\pi/2} & e^{-9.i\pi/2} \end{bmatrix} \begin{bmatrix} m_{j0k}\\ m_{j1k}\\ m_{j2k}\\ m_{j3k} \end{bmatrix} \quad (11)$$

And

$$\begin{bmatrix} m^*_{j0k}\\ m^*_{j1k}\\ m^*_{j2k}\\ m^*_{j3k} \end{bmatrix} = \begin{bmatrix} 1 & 1 & 1 & 1\\ 1 & -i & -1 & i\\ 1 & -1 & 1 & -1\\ 1 & i & -1 & -i \end{bmatrix} \begin{bmatrix} m_{j0k}\\ m_{j1k}\\ m_{j2k}\\ m_{j3k} \end{bmatrix} \quad (12)$$

The next stage is to compute the Inverse Discrete Fourier Transform (IDFT). The IDFT is given by:

$$m_{jk} = IDFT\left\{m^*_{jk}\right\} = \frac{1}{p}\sum_{r=0}^{p-1} m^*_{jk}e^{i(2\pi st/p)}, \quad (13)$$

For $p=4$ the IDFT is giv

$$\begin{bmatrix} m_{j0k}\\ m_{j1k}\\ m_{j2k}\\ m_{j3k} \end{bmatrix} = \frac{1}{4}\begin{bmatrix} e^{-0.i\pi/2} & e^{-0i\pi/2} & e^{-0.i\pi/2} & e^{\overline{-0.i\pi/2}}\\ e^{-0.i\pi/2} & e^{-1i\pi/2} & e^{-2.i\pi/2} & e^{-3.i\pi2}\\ e^{-0.i\pi/2} & e^{-2i\pi/2} & e^{-4.i\pi/2} & e^{-6.i\pi/2}\\ e^{-0.i\pi/2} & e^{-3.i\pi2} & e^{-6.i\pi/2} & e^{-9.i\pi/2} \end{bmatrix} \begin{bmatrix} m^*_{j0k}\\ m^*_{j1k}\\ m^*_{j2k}\\ m^*_{j3k} \end{bmatrix} \quad (14)$$

And

$$\begin{bmatrix} m_{j0k}\\ m_{j1k}\\ m_{j2k}\\ m_{j3k} \end{bmatrix} = \frac{1}{4}\begin{bmatrix} 1 & 1 & 1 & 1\\ 1 & i & 1 & -i\\ 1 & 1 & -1 & 1\\ 1 & -i & 1 & i \end{bmatrix} \begin{bmatrix} m^*_{j0k}\\ m^*_{j1k}\\ m^*_{j2k}\\ m^*_{j3k} \end{bmatrix} \quad (15)$$

2.3.3. Independent Component Analysis

Independent component analysis (ICA) is a multivariate data analysis method that, gives a linear mixture of statistical independent sources and recovers these components by producing an unmixing matrix (Varshney and Arora, 2004). A problem setting of ICA is as follows: Assume there is an L_ dimensional Zero_ mean non Gaussian source vector $s(n) = [s_1(n), ..., s_L(n)]^T$, such that the components $S_i(n)$ s are mutually independent and an observed data vector $x(n) = [x_1(n), ..., x_N(n)]$ is composed of linear combination of sources $S_i(n)$ at each time point n, such that

$$X(n) = As(n) \tag{16}$$

Where A is a full rank $N \times L$ matrix where $L \leq N$. The goal of ICA is to find a linear mapping W such that each component of an estimate u of the source vector Is independent as possible.

$$u(n) = Wx(n) = WAs(n) \tag{17}$$

The original sources s (n), are exactly recovered when W is the pseudo_ inverse of A up to some scale changes and permutations. For a derivation of an ICA algorithm, one usually assumes that L=N, because there is no idea about the number of sources. In addition, sources are assumed to be independent of time n and are drawn from independent identical distribution $p_i(s_i)$ (Kawn and Kim, 2006).

2.3.4. Minimum Noise Fraction

Minimum noise fraction (MNF) is a well-known technique for hyper spectral imagery denoising. It transforms a noisy data cube into output channel images with steadily increasing noise levels, which means that the MNF output images contain steadily decreasing image quality (Lou et al., 2016). In a common practice, MNF components with eigenvalue less than 1 such as noise are usually excluded from the data in order to improve the subsequent spectral processing results, since Eigen images with near unity eigenvalues are normally noise dominated (Qiu et al., 2006).

3. Classification

After applying FFT-PCA method on OLI bands, three dimensionality reduction algorithms (PCA, ICA, MNF) applied on this fused image and regarding field surveys and visual interpretation of the images, a total of 8 classes including water bodies, snow, rich range lands, poor range lands (degraded), agricultural lands, fallow, bare lands and settlement were selected and training data of each other were taken from the images. A total of 150 training samples for each class were selected from the images after applying the FFT-PCA-PCA, FFT-PCA-ICA and FFT-PCA-MNF methods. After using this method, the separability of the samples was evaluated using the Jeffris Matusita index.

Support vector machine is a useful technique for data classification (Abbasi et al., 2015). A classification task usually involves separating data into training and testing sets. Each instance in the training set contains one “target value” (i.e. the class labels) and several “attributes” (i.e. the features or observed variables). The goal of SVM is to produce a model (based on the training data) which predicts the target values of the test data given only the test data attributes (Hsu et al., 2003).

Given a training set of instance label point $(x_i, y_i), i = 1,...,l$ where $x_i \in R^n$ and $y \in \{1,-1\}^l$, the support vector machine (SVM) requires the solution of the following optimization problem:

$$\min_{w,b,\epsilon} \quad \frac{1}{2} w^T w + C \sum_{i=1}^{l} \epsilon_i$$
$$\text{Subject to } y_i (w^T \phi(x_i) + b) \geq 1 - \epsilon_i, \qquad (18)$$
$$\epsilon_i \geq 0.$$

Here the training vector xi is mapped into a higher (maybe infinite) dimensional space by the function ϕ. SVM finds a linear separating hyperplane with the maximal margin in this higher dimensional space. $C > 0$ is the penalty parameter of the error term. Furthermore, $K(x_i, x_j) = \phi(x_i)^T \phi(x_j)$ is called the kernel function. Though new kernels are being proposed by researchers, beginners may find in SVM books the following four basic kernels:

- Linear: $K(x_i, x_j) = x_i^T x_j$.
- Polynomial: $K(x_i, x_j) = (\gamma x_i^T x_j + r)^d, \gamma > 0$.
- Radial Basis Function (RBF): $K(x_i, x_j) = \exp(-\gamma ||x_i - x_j||^2), \gamma > 0$.
- Sigmoid: $K(x_i, x_j) = \tanh(\gamma x_i^T x_j + r)$.

Here, γ, r are kernel parameters.

4. Results and Discussion

Jefrries Matusita index that was tested for ROIs separabilities showed that all of the classes had good separabilities (>1.90), which is shown in Table (2). Therefore, the samples have a low correlation with each other, and many of the samples are not correlated at all, which indicates the high accuracy of the training samples taken for image classification. The panchromatic and multispectral bands of OLI sensor were fused based on FFT-PCA method. Figure (2), shows the result of OLI bands fusion with FFT-PCA method.

Table 2. Results of Jefrries Matusita index on ROIs correlation

	Water bodies	**Snow**	**Rich range land**	**Poor range land**	**Agriculture**	**Fallow**	**Bare**	**settlement**
Water bodies		2	2	2	2	2	2	2
Snow	2		2	2	2	2	2	2
Rich range land	2	2		1.99	1.99	1.99	1.99	2
Poor range land	2	2	1.99		2	2	1.97	2
Agriculture	2	2	1.99	2		1.93	2	2
Fallow	2	2	1.99	2	1.93		2	2
Bare	2	2	1.99	1.97	2	2		1.99
settlement	2	2	2	2	2	2	1.99	

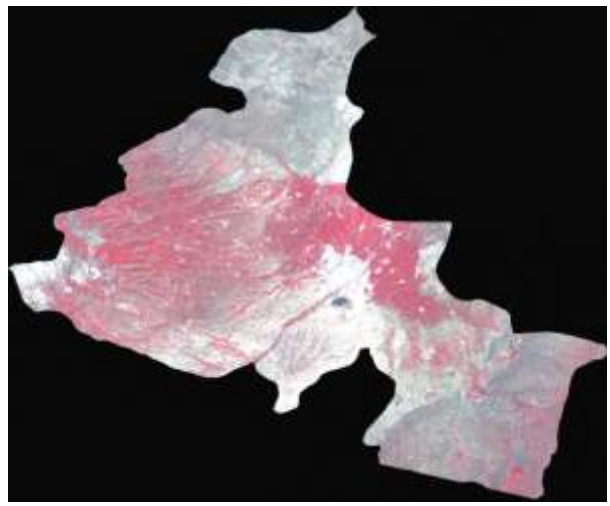

Figure 2. Fusion of OLI panchromatic and multispectral bands based on FFT-PCA method

Three dimensionality reduction algorithms (PCA, ICA, MNF), were applied on the fused image to evaluate the effect of this algorithm on classification accuracy. The classification of images based on FFT-PCA-PCA, FFT-PCA-ICA and FFT-PCA-MNF methods was performed using a Support Vector Machine (SVM), algorithm with a radial kernel. Figures (3-5), show the classification result of images based on each dimensionality reduction algorithms.

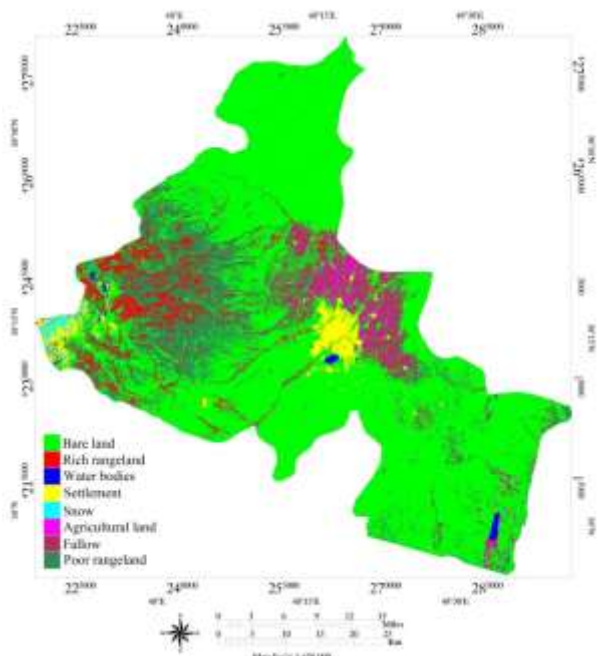

Figure 3. FFT-PCA-PCA based radial SVM classification

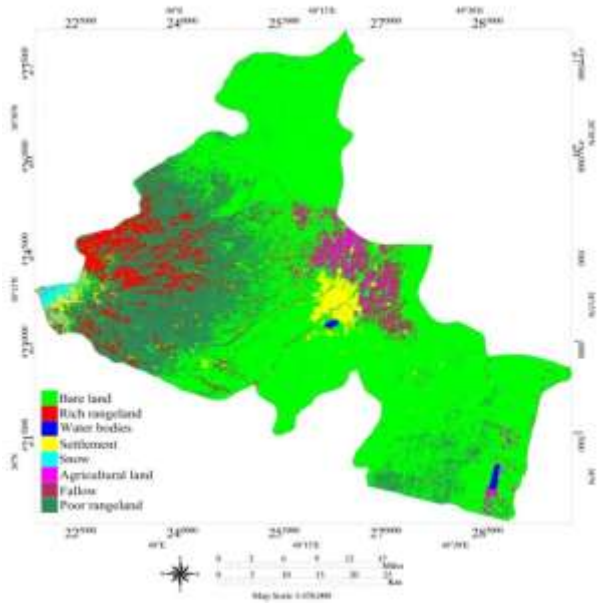

Figure 4. FFT-PCA-MNF based radial SVM classification

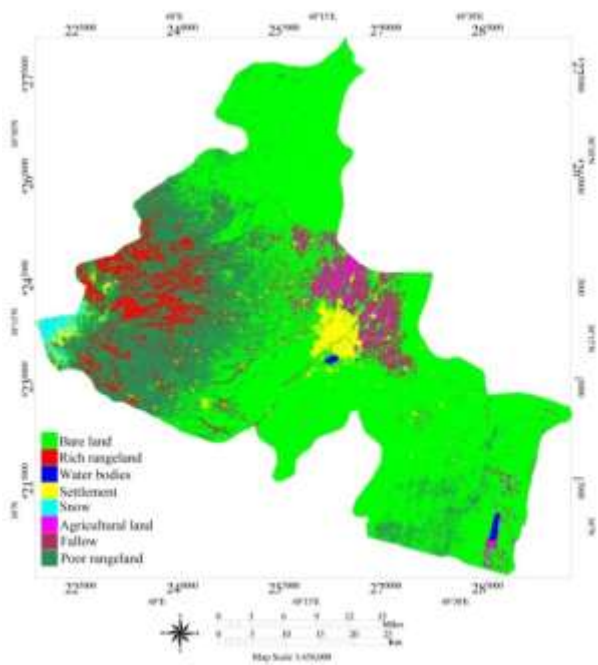

Figure 5. FFT-PCA-ICA based radial SVM classification

The results showed that FFT-PCA-ICA method have the lowest accuracy among the other two. This method has 86.9% and 0.84 overall accuracy and Kappa coefficient respectively. Also FFT-PCA-PCA method has an overall accuracy of 89% and Kappa coefficient of 0.91. The FFT-PCA-

MNF method has the highest accuracy among the other two DR methods in OLI data classification and has 96.8% and 0.96 overall accuracy and Kappa coefficient respectively. Table (3) shows the accuracy assessment of DR methods classification.

Table 3. Overall accuracy and Kappa coefficient

	Overall accuracy (%)	**Kappa coefficient**
FFT-PCA-ICA	86.9	84
FFT-PCA-PCA	89	91
FFT-PCA-MNF	96.8	96

Produce accuracy and user accuracy of DR methods based classification is shown in Table (4).

Table 4. Produce accuracy and User accuracy

		Prod. Acc(%)	**User Acc(%)**		**Prod. Acc(%)**	**User Acc(%)**		**Prod. Acc(%)**	**User Acc(%)**
	Bare land	80.43	51.39		100	86.67		97.44	97.44
	Rich rangeland	71.70	95		100	95		100	95
ICA	Water bodies	94.64	96.36	**PCA**	100	100	**MNF**	100	100
	Settlement	100	95		65	100		98.25	100
	Snow	98.72	96.25		100	69.37		100	100
	Agricultural land	75.81	87.04		100	92.73		92.16	87.04
	Fallow	72.37	84.62		93.55	100		88.71	93.22
	Poor range land	95.56	89.58		84.44	100		95.56	97.73

5. Conclusions

This paper has shown the FFT-PCA-DR based image classification accuracy assessment based on OLI data. The performance of SVM classification based on dimensionality reduction algorithms was quite good on OLI data classification. The overall accuracy and Kappa coefficient values range from 86.9% to 96.8% and 0.84 to 0.96 respectively, showed the effect of selected methods on final classification accuracy. Most of the classes are better classified when MNF DR method selected to SVMs input. The better noise reduction in MNF method may account for the better performance of an OLI data classification. Among the PCA and ICA methods, the ICA has a low performance because of its non-Gaussian nature that developed for hyperspectral data. In comparison to the related research (Lou et al., 2016; Sahisi and Krishna; Bashirpour et al., 2017), in this study, in addition to comparing three common methods of reducing data dimensions, a hybrid method has also been used to integrate data in order to increase the accuracy of data extraction from OLI data. In most studies conducted in this regard, the PCA, ICA, and MNF methods are used for hyper

spectral data that comparison of these three methods to multi-spectral data along with the FFT-PCA method is the strength of this research and distinguishes it from consistent researches.

References

Abbasi, B., Arefi, H., Bigdeli, B., & Roessner, S. (2015). Automatic generation of training data for hyperspectral image classification using Support Vector Machine. 36th International Symposium on Remote Sensing of Environment, Berlin, Germany.

Alhirmizy, S. A. (2015). Comparative Study between Landsat-8 OLI and Landsat-7 ETM+ for sensor signal-to-noise performance, Spectral Distortion, and spectral signature matching: A Study in the IRAQ Landscape, Remote sensing.

Arslan, O., Akyurken, O., & Kaya, S. (2017). A comparative analysis of classification methods for hyperspectral images generated with conventional dimension reduction methods. Turkish Journal of Electrical Engineering & Computer Sciences, 25, 58-72.

Asiedu, L., Adebanji, A. O., Oduro, F. T., & Mettle, F. O. (2016). Statistical assessment of PCA/SVD and FFT-PCA/SVD on variable facial expression. British journal of Mathematics & Computer science, 12, 1-23.

Bai, L., Xu, Ch., & Wang, C. (2015). A review of fusion methods of multispectral image. International Journal for Light and Electron Optics, 126, 4804-4807.

Bashirpour, M., Valadan Zoej, M. J., & Maghsoudi, Y. (2017). Effect of different SRFs on time series of spectral indices, between sentinel-2 and other sensors for the purpose of vegetation land cover monitoring. Journal of geospatial information technology, 5, 123-140.

Chul ko, B., Hun Kim, H., & Yeal Nam, J. (2015). Classification of potential water bodies using Landsat-8 OLI and combination of two boosted random forest classification. Sensors, 15, 13763-13777.

Dhavan, R., & Garg, N. K. (2014). A hybrid approach of wavelets for effective image fusion for multimodal medical images. International journal of technical research and application, 2, 44-48.

Ghasemlounia, R., & Sedaghat Herfe, N. (2017). Study on groundwater quality using geographic information system (GIS), Case study: Ardabil, Iran. Civil engineering, 3, 779-793.

Hasani Moghaddam, H., Adli Atiq, R., Gholami, J., Abasi Ghadim, M., & Zeaiean Firooz Abadi, P. (2018). Performance Analysis of Support Vector Machine, Neural Network and Maximum Likelihood in Land use/cover Mapping and GIS. 2nd International Conference on New Horizons in the Engineering Science, Yildiz Technical University. Istanbul. Turkey.

Hasani Moghaddam, H. (2017). Performance evaluation of wavelet transform with decision level algorithms in fusion of Hyperspectral and High spatial resolution images. MA thesis of Kharazmi University, Tehran. Iran.

Hsu, C. W., Chang, C. C., & Lin, C. J. (2003). A practical guide to support vector classification.

Kaur, D. (2016). Image fusion using Hybrid techniques (PCA+SWT). International journal of engineering and computer science, 5, 15661-15667.

Knight, E, J., & Kvaran, G. (2014). Landsat-8 operational land imager design, characterization and performance. Remote sensing, 6, 10286- 10305.

Kwak, N., & Kim, C. (2006). Dimensionality reduction based on ICA for regression problems, In International Conference on Artificial Neural Networks Springer, Berlin, Heidelberg.

Kumar Singla, S., Dev Garg, R., Prakash Dubey, O., & Bala, A. (2018). Extraction of crop information from reconstructed Landsat data in Himalayan Foothills region. 6th International Conference on smart computing and communication, Kurukshetra. India.

Lou, G., Chen, G., & Tian, L. (2016). Minimum Noise Fraction versus Principal Component Analysis as a Preprocessing Step for Hyper spectral Imagery Denoising. Canadian Journal of Remote Sensing, 42.

Liu, J. (2017). Application of satellite image time series and texture information in land cover characterization and burned area detection, Academic dissertation, University of Helsinki.

Mamachan, P., & Baby, J. (2015). Denoising of images using a hybrid image fusion algorithms. International journal of advanced research in electrical, electronic and instrumentation engineering, 4, 5813- 5818.

Ping, P., Zhu, X., & Wang, L. (2017). Similarities/ Dissimilarities arities analysis of protein sequences based on PCA-FFT. Journal of biological systems, 25, 29-45.

Qiu, F., Abdelsalam, M., & Thakkar, P. (2006). Spectral analysis of Aster data covering part of the Neoproterozoic Allaqi- Heiani suture, southern Egypt. Journal of African Earth science, 44, 169-180.

Sahisi, V. S., & Krishna, I. V. M. (2016). Performance evaluation of dimensionality reduction techniques on CHRIS hyper spectral data for surface discrimination. Journal of Geomatics, 10.

Sorzano, C. O. S., Vargas, J., & Montano, A. P. (2014). A survey of dimensionality reduction techniques, arXiv preprint arXiv:1403.2877.

Torahi, A., Adli Atiq, R., & Hasani Moghaddam, H. (2016). Evaluating the capability of supervised classification algorithms in land use/cover map preparation. The 1st national conference on geospatial information technology, K. N. Toosi University. Tehran. Iran.

Unlusoy, D. (2013). Image fusion for improving spatial resolution of multispectral satellite images, Thesis for Master of Science, Middle East technical university.

Varshney, P. K., & Arora, M. K. (2004). Advanced image processing techniques for remotely sensed hyperspectral data. Springer. USA.

Vivekan, A. J., Thirumurugan, P., & Dhanarega, A. J. (2014). Image fusion and improving classification accuracy: A review. International journal of engineering science & research technology, 3, 496-500.

Wang, J., & Chang, Ch. I. (2006). Independent Component Analysis-Based Dimensionality Reduction with Applications in Hyperspectral Image Analysis. IEEE Translation and geoscience and remote sensing, 44, 1586-1600.

Wang, M., Yu, J., Niu, L., & Sun, W. (2017). Unsupervised feature extraction for hyper spectral images using combined low rank representation and locally linear embedding, ICAASP, 1428-1431.

Yusuf, Y., Tetuko Sri Sumantyo, J., & Kuze, H. (2013). Spectral information analysis of image fusion data for remote sensing application. Geocarto international, 28, 291- 310.

Available online at www.jrors.ir

JRORS
Journal Of Radar and Optic Remote Sensing

Journal Of Radar and Optic Remote Sensing

JRORS 2 (2018) 38–54

Detecting and predicting vegetation cover changes using sentinel 2 Data (A Case Study: Andika Region)

Sedigheh Emami[a*] , esmail Emami[b]

[a]*Ms in GIS, remote sensing,Yazd Branch, Islamic Azad University, Yazd, Iran*
[b]*Graduate student University of electric power systems of the Islamic trends free khomeynishahr*

Received 12 February 2018; revised 9 April 2018; accepted 10 June 2018

Abstract

The earth surface is itself a complex system, and land cover variation is a complex process influenced by the interference of variables. In this study, the data of Sentinel 2 for 2017 and 2016 were processed and classified to study the changes in the Andika area. After discovering vegetation changes between two images over the mentioned time, vegetation increased by 661.74 hectares. Multiple regressions have been used to identify factors affecting vegetation changes. Multiple regressions can explain the relationship between vegetation changes and the factors affecting them. In order to investigate the factors affecting vegetation change, altitude data, distance from the road, distance from residential areas of the village and river were introduced into regression equation. Since this method uses three parameters such as Pseudo-R^2 and Relative Operation Characteristic (ROC), 0.23, and 0.696 values for the above parameters, which indicates that the model is in good agreement. The results of regression analysis show that linear composition of height variable as independent variables in comparison with other parameters has been able to estimate vegetation change. Subsequently, by using two classified pictures of 2017 and 2016, the amount of vegetation changes was calculated, and Markov chain method was used for 2018 forecast changes.

Keywords: NDVI, Sentinel 2, Cellular Automata Markov and logistic regression

* Corresponding author. Tel: +98-9166225978.
E-mail address: s.emami061@gmail.com.

1. Introduction

On a global scale, population growth can be considered as the main reason for changing the land use. Paying attention to the patterns, the trend of landscape changes to understand the dynamics of vegetation, sustainable conservation and assessment of management approaches is necessary. In recent years, much attention has been paid to changes in land cover, land use and vegetation change. Forecasting and modeling of land cover changes, such as urban development, deforestation, etc. are considered as a powerful tool for managing natural resources and monitoring environmental changes. These changes reflect how are human interactions with the environment and its modeling influences large-scale decision-making and planning (Aslani Moghadam, 2012).

Some phenomena and complications of the earth's surface, such as vegetation, have changed over time due to natural or human factors, which affects the ecosystem's condition and performance. Therefore, the need to detect, predict and care for such changes in an ecosystem is of great importance. In addition, acquiring knowledge about vegetation and its effective factors in soil management plays an important role. Today, the production of a detailed vegetation map is one of the most important tools in design and development. It is usually difficult and limited to monitor vegetation on a global or regional scale. Because traditional and old data is collected from small location at different time interval, which differ in terms of type and credit rating (Pettorelli et al., 2005). Remote sensing technology is a very useful tool that can be used to obtain information layers from soil and vegetation (Adamchuk et al., 2004). Features such as providing a broad and integrated view of a region, the ability to repeat, the ease to use information, and the high accuracy of the resulting information and saving time are the features used to examine vegetation. Accordingly, many researchers have used remote sensing data to study vegetation and this technique is suitable for such studies (Pettorelli et al., 2005; Huete and ustin, 2004). The Normalized Difference Vegetation Index (NDVI)has been beneficial in many studies. This indicator is based on the fact that the chlorophyll in the plant can absorb red light and reflect the mesophilic layer of the near-infrared light.

This index is calculated using the NDVI formula (Equation 1) and its value varies between 1+ and -1. The negative values in this index indicate the absence of vegetation (Pettorelli et al., 2005; Adamchuk et al., 2004; Al-Madrasi Al-Husseini, 2013). The value of this indicator is influenced by the factors that awareness of them play an important role in vegetation studies. In this research, multiple regression has been used to identify the factors influencing vegetation changes.

Normalized Vegetation Index= (TM4-TM3)/ (TM4+TM3) (1)

One of the tools used by planners to control the process of changing forests cover is regression relations, given that environmental science deals with various phenomena. Therefore, in regression issues, multiple regressions are of great importance (Bihamta and Zare Chahui, 2011). Multiple linear regressions are available to analyze the relationship between multiple variables. In multiple linear regressions there is an assumption of the existence of linear relationship between dependent variables and independent variables (Salman Mahini et al., 2012). Using remote sensing data and linear regression equation in GIS environment provides a better understanding of how to change

forest cover and determine the effecting factors. Jafarzadeh and Arkhi (2012), simulated destruction in the northern forests of Ilam, they aimed to predict the spatial distribution of deforestation and the identification of its effective factors in the northern forests of Ilam province. In order to estimate the spatial distribution of deforestation, the logistic regression method was used for modeling. Modeling results showed that deforestation is the most commonly found phenomenon in discrete forest coverages and in areas near forest and non-forest boundaries (Miranda et al., 2012). Modeling regions are susceptible to forest cover changes using logistic regression in the rain forest of northern Mexico. The results showed that forests in the study area are highly susceptible to degradation and change in utilization, which is a major factor in increasing the population and unnecessary use of forest resources in the region. The study of land cover change in Isfahan area was carried out during the years 1987 to 1998 (Safiyanian, 2009). The results indicated that the ground level of agriculture has undergone significant changes. In another study in Isfahan, population growth has been the main factor in reducing vegetation cover and increasing residential utilization (Zairi Amirani and Safiyanian, 2010). In the country, limited research has been done on coastal land changes. In a study of land change in Aslouyeh coastal area shows that under the influence of land changes, the erosion and sediment of the area have changed dramatically (Na'imi Nezam et al., 2010). Also, remote sensing is an appropriate tool for monitoring coastal land changes (Ghazalfali and Alawafanah, 2010). A variety of studies have been done to simulate coating changes using the CA-Markov model. These include studies in the prediction of the land cover situation in Isfahan (Fallahtakar et al., 2009) simulation of land cover changes in the Gorganroud area, (Sheikh Goodarzi et al., 2013) and the study of vegetation changes (Chang et al., 2006; López et al., 2001; Sang et al., 2011).

Therefore, considering the importance of the study of vegetation changes, as well as the determination of coordinated and integrated planning for sustainable use of land resources, the present research intends to study the trend of vegetation changes over environmental factors by determining the land cover changes in the Andika city, using satellite data and the time trend of vegetation changes using the logistic regression.

The distinction between the present study and previous study in this model, while identifying the positive or negative effects of each variable on the presence and absence of effective factors, can identify variables that have a greater effect on the behavior of vegetation changes (Sensitization). The present study intends to use the satellite data to model landslide changes in the Andika city, and to prepare spatial distribution of changes map and to fit the Logistic regression model to investigate the vegetation change and map the probability of vegetation change in the study area. The general objective of this research is to identify the factors affecting vegetation change and predict vegetation changes in the forested area of Indica in northern Khuzestan province.

2. Materials and Methods

2.1. Realm of research

Andika is located between 49 degrees and 53 minutes to 49 degrees and 52 minutes east longitude from Prime Meridian (Greenwich) and 31 degrees and 43 minutes to 32 degrees and 39 minutes north latitude from the equator in the eastern part of Khuzestan province. The area of the Andika city is 2336 km^2 and the altitude of the sea level is approximately 800 meters. The elevation is between 400 and 3000 meters above sea level. The average temperature is 50°C in July, and the average temperature is 6°C in January and the average annual precipitation is 400 mm in the form of rain and hail; and snow in the highlands of the region. The amberthermic curve shows that the region has no rainfall since late spring to early autumn (Figure 1).

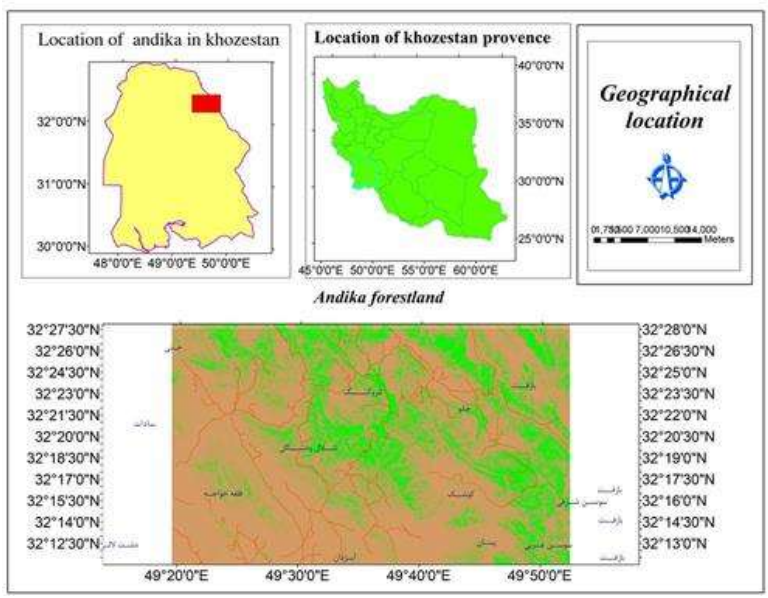

Figure 1. Geographical location of the study area

2.2. Research Method

Land changes have been studied for many years. However, the advent of satellite imagery and land-based techniques has opened a new dimension to review and evaluate land change patterns (Matsushita et al., 2007). Geographic information system and remote sensing data can be used as a tool for analysis and provide accurate results (Aronov, 2013). The multivariate feature of satellite imagery for assessing changes is widely been used in environmental review, land cover change assessments, forest surveys, and urban studies which plays an important role in many areas of application (Zebiri and Majd, 2001).

In this research, in order to achieve quantitative and qualitative changes in vegetation changes in the Andika region, the normalized difference index data (an indicator based on the band ratio) was

extracted from Sentinel satellite images of 2016 and 2017. This index is calculated using the formula (equation 1) and its value varies between numbers +1 and -1. Negative values in this index indicate the absence of vegetation (Aslani Moghadam, 2012; Almodaresi Al-Husseini, 2015). In this study, in order to study vegetation changes as an associated variable and digital elevation data from the sea level, distance from the road, distance from residential areas of the village and river as effective parameters in vegetation change process as independent variables in establishing multiple linear regression. The regression equation shows each of the independent variables and the constant coefficient. The constant coefficient represents the value of the dependent variable at the time when all independent variables have zero values. Regression coefficients show the effect of each independent variable on the dependent variable. R represents the multiple correlation coefficients between dependent variables and independent variables. R^2 indicates the variability of the dependent variable based on all independent variables. Using the determination coefficient, it is determined how much is variable variation dependent on the independent variable. Several methods for analyzing the time series of images, such as principal components analysis, wavelet analysis, Fourier analysis, are proposed. These methods allow the change process to be interpreted only between two periods (e.g. between years or stages of growth), which makes analysis dependent on the choice of these courses. Additionally, changing the time series that occurs with seasonal variations of temperature and rainfall, the techniques of detecting changes focuses on minimizing seasonal variations over a particular period in a year. In order to predict forest area changes, the CA-Markov model was used. Markov chain analysis describes land-use changes from one period to another and uses them as a basis for mapping future changes. CA-Markov is an important issue in Markov's analysis and there is no spatial element in this modeling (Mahdavi et al., 2015).

In fact, the Markov model focuses on quantity in predicting land changes. The spatial parameters in this model are weak and different types of land cover variations are not recognized in spatial patterns (Sang et al., 2011). The automated CA network will be used to add the location element to the model. CA has the capability to locate spatially-temporal dynamics in combination with sophisticated spatial systems, with a good location-based detection capability. The CA-Markov model combines the ability of Markov and CA which is well-suited for predicting spatial and temporal series. Thus, the CA-Markov model provides a better simulation of spatial and temporal patterns of land cover variations in a given amount and location (Sang et al., 2011). In this study, the CA-Markov model integrated with the Idrisi program was used to simulate forest cover change.

Several software applications have been used in this research. Among them are: 1. ENVI4.8 and SNAP software for geo-referencing images and production of vegetation map and classification. 2. EDRISI software for applying the LCM model, mapping the vegetation changes, preparation of independent variables, and also studying the potential of vegetation change due to independent factors. 3. ArcGIS10.2 for cutting the area.

3. Results

3.1. Change detection

The discovery of changes has been one of the major applications of measuring sensitivity. With the repetition of the remote sensing data of different times, it is possible to detect and verify the dynamic variable phenomena in the environment. Identifying an appropriate method for detecting changes in the region to generate good results is a crucial element in detecting changes (Matsushita et al., 2007). In this study, NDVI method was used to detect the vegetation changes.

Image 2 has latitude of 290 km and a precision of 10 meters. First, two geometric corrections were made for 2016 and 2017, and then the desired range was clipped, used to cut a layer of a vector in the ENVI4.8 software. Then, NDVI from the desired areas was created and classified for each image (Figure 2).

The NDVI value varies between +1 and -1. The negative values in this index indicate water and values from 0 to 0.2 are the soil classes (the first class is from -1 to 0.2 which means the vegetation is absent) and the values of 0.2 to 1 are attributed to the vegetation class. The classification results showed that in 2016, the total surface area of the region was about 35884.78 hectares covered by vegetation, while in 2017 vegetation class were about 35223.04 hectares (Table 1).

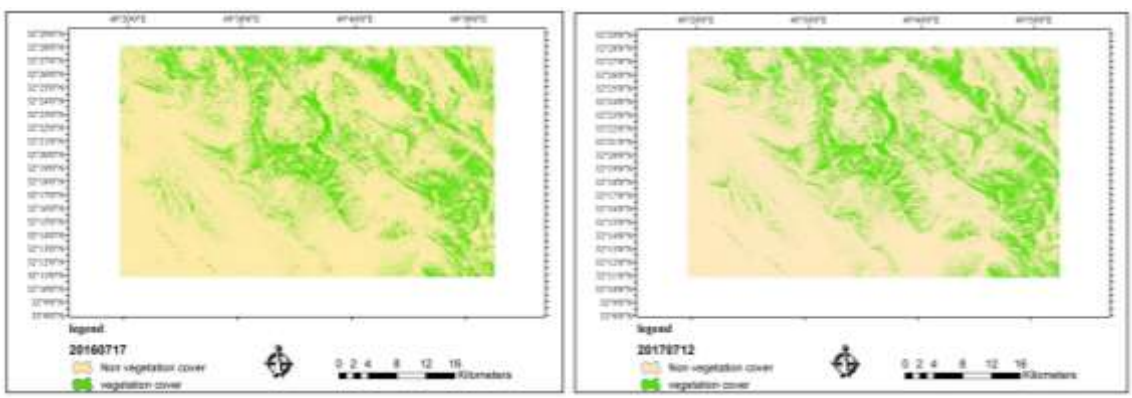

Figure 2. Classification of vegetation in the Andika region

Table 1. Changes in vegetation cover in 2016-2017

User classes	Non vegetation cover	vegetation cover	Total
Area of 2016 (Hectare)	128489.42	35884.78	164374.2
Area of 2017 (Hectare)	129151.16	35223.04	164374.2
Level of changes (Hectare)	661.74	-661.74	
Percentage change versus total	0.402581	0.40258	

The results of the comparison between the two maps indicates that 661.74 hectares of vegetation areas have been reduced. The change is shown in Figure 3 and the changes in the vegetation cover are shown in Figure 4.

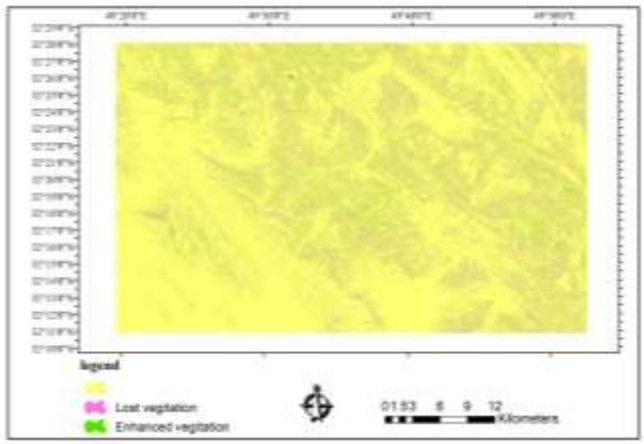

Figure 3. Map of vegetation changes in the Andika region

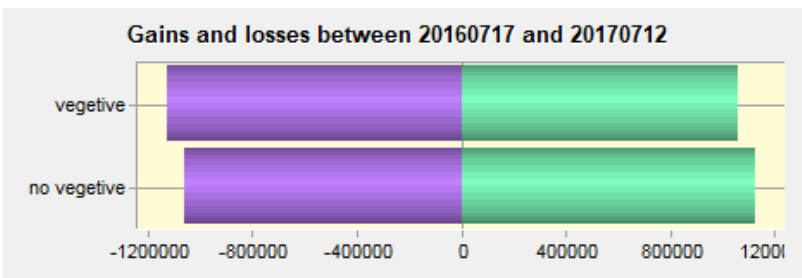

Figure 4. Vegetation changes in the Andika region between 2017 and 2016

Table 2. Variation in vegetation cover between 2016-2016

User classes	Changes (Hectare)
Non vegetation cover to vegetation cover	10604.48
Vegetation to the Non vegetation cover	11266.22
Total	21870.7

The study area with an area of 2187.7 hectares has been observed which shows that 11266.22 hectares of the vegetation cover area has been destroyed and 10604.48 hectares of land has changed to vegetation.

3.2. Multiple regressions

Empirical estimation methods, using statistical techniques, models the relationship between the forest cover reduction and the influencing factors. Logistic regression is one of the experimental

models that fit the probabilistic model between forest cover reduction (as dependent variable) and its effective factors (as an independent variable). Based on this model, one can explain the relationship between variables, estimate the relative importance of index variables and map (Kamyab et al., 2010).

After determining the location and extent of vegetation changes, multiple linear regressions assume a linear relationship between dependent and independent variables. With a number of independent variables, the linear multiple regression equation will be (Relationship 2). In logistic regression, the null hypothesis is that the probability of obtaining a certain value of a nominal variable in relation to a measured variable is not, or indeed, the linear gradient that expresses the relationship between the measurement variable and the probability of a nominal variable is zero. Logistic regression is followed by an equation that predicts the value of the variable Y for each value of the X variable. Here, the dependent variable Y is not directly measured; instead the probability of obtaining a certain value of it is investigated. This probability is between zero and one variable, although this value cannot be directly entered in the regression (Shojaeai et al., 2017).

$$Y= a+b1\ x1 +b2\ x2 +\ldots+bn\ xn \quad (2)$$

In the process of modeling with the logistic regression that is done in the Idrisi software, a map will eventually result in a model showing the potential for vegetation changes for 2016 and 2017. A file that contains information on modeling results, the weight of independent variables and indicators for assessing the logistic regression model are presented along with the output map of the model (Figure 5).

3.3. Assessing the logistic regression

Recently, the developing world has experienced unprecedented growth in urban areas which has a significant impact on land use intensification. Therefore, modeling and predicting changes for planning natural resource conservation advocates is crucial for setting up a sustainable development strategy, whose main goal is to identify the factors and the process of changes (Kamyabet al., 2010). Indicators for evaluation of logistic regression model the ROC index is expressed numerically between 0-1 which is obtained from the ROC curve When there is a perfect match between the actual map and the map from the model. The ROC index is equal to one and The value of 0.5 for this indicator expresses the randomness of the positions and shows that the value of the cells in the prediction map is created in the form of random positions (Mirza'i Zadeh et al., 2016). The use of the Pseudo-R2 index in the logistic regression model for the fit test of the model was confirmed by McFadden 1973 Domnick and McFadden 1975 and Clarke and Hawking 1986 (Mesgari and Ranjbar, 2003; Domencich and McFadden, 1975; Clark and Hosking, 1986). According to the study, the Pseudo-R2 acceptable rate for verifying the satisfaction of the model ranges from 0.2-0.4 (Mirza'i Zadeh et al., 2016).

$$\text{logit (lcm Train Non vegetation cover to vegetation)} = -1.6322+1.489921\ *\text{contour} - 0.354199*\text{road} - 1.626083*\text{river} - 0.434008*\text{village} \quad (3)$$

The Distance from urban and rural residential areas and also the distance from the road and the river were considered as independent variables. Then, the linear multiple regression relationship between vegetation changes was established as a dependent variable with the above parameters, which is shown in Table 3. Regression coefficients show the effect of each independent variable on the dependent variable.

Table 3. Multiple Regression Model Linear Results

Adjusted Odds Ratio	ROC	Chi-square	Pseudo R-square	B4x4	B3x3	B2x2	B1x1	A	Y
1.4797	0.696	5402.3866	0.23	-0.434008	-1.626083	-0.354199	1.489921	-1.6322	Y1
				Village	River	Road	Height	y-intercept	Vegetation changes

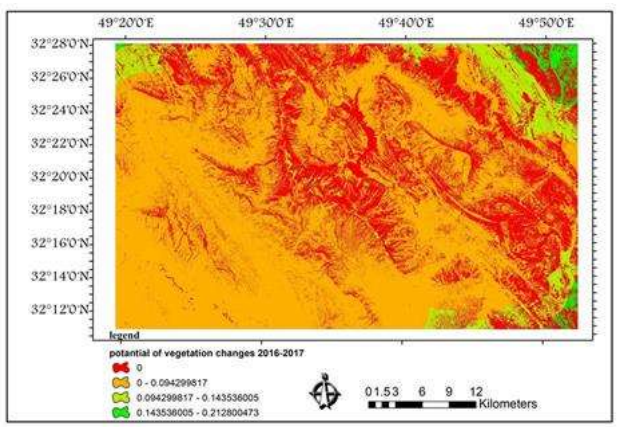

Figure 5. Output map of Logistic Regression Model (Potential of non-vegetation cover conversion to vegetation)

Since this method uses three parameters such as Pseudo-R^2, ROC, there is a value of 0.23, 0.696 obtained for the above parameters that represents the good fit of the resulting model with reality (Almodaresi Al-Husseini, 2015). Using the coefficient of determination, it is determined how much is change dependent on the independent variable. According to the coefficient determined with a probability of 0.696, vegetation cover per hectare has been created by independent variables. It can be said that the error rate of 10% indicates that the probability of the model error is 49969.7 hectares. The ROC value for the present study was 0.696. This statistic is an appropriate statistic for assessing the validity of the model and can be used to compare the actualized image. Value 1 represents the complete spatial agreement and value of 50% represents a low agreement of the model with reality (Salman Mahini et al., 2012).

3.4. Model sensitivity

In order to determine the importance of independent variables, the sensitivity of the model (regression equation of soil changes to vegetation) has been studied. The sensitivity of the multiple linear regression model is such that and after the implementation of the model with a complete data series, the model is restored to the number of independent variables. Now, the difference in each stage is the model of one of the independent variables which is eliminated and the model with the remaining independent variables is performed (Courage and Aniya, 2009). The advantage of this is in sensitizing the variables and discovering the effect of the variables in the final model. After each iteration, the coefficient of model determination is extracted and based on the obtained difference with the complete data series, the independent variable is calculated (Figure 5). The variables of distance from height have a determinant effect on the performance of the model because by deleting these variables, the coefficient index determines a significant decrease (Salman Mahini et al., 2012).

Table 4. Results of the model sensitivity

Deleted independent variable	Variable coefficient	Deleted independent
Perfect model	0.696	1
Village	0.6299	2
Road	0.5937	3
River	0.6442	4
Height	0.5904	5

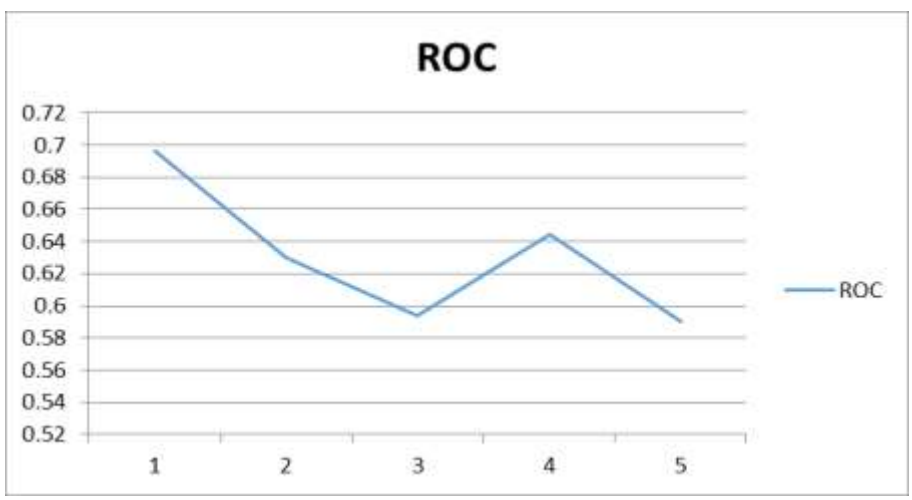

Chart 1. Relationship between ROC and independent variable

With enough information on how to change the city and the process of vegetation change, better plan can be mastered on how to expand the city and vegetation in future. The area of Andika includes a metropolitan area on a hillside and the villages scattered around the city. Since the height

is a deterrent factor of urban development, this model does not consider the mountainous areas susceptible to agriculture. Mountain range areas are more agricultural in terms of their location and the greatest potential for changing vegetation is in the bulk. The sensitivity of the model shows that the height of the mountains has the largest effect on vegetation change and oak shoots are mostly concentrated in mountain heights Figure 6.

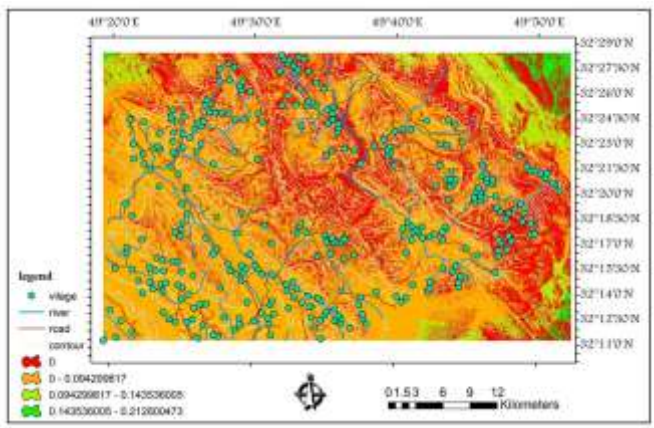

Figure 6. Map of change potential in the Andika region along with factors affecting vegetation change

3.5. Predicting Markov chain model changes

There are models of land cover variations, including mathematical and statistical equations, systematic models, randomized models, and automated cell-based models (Sheikh Goodarzi et al., 2013). CA-Markov is a hybrid model of automated cells 4 and Markov system 1. The CA-Markov model is a suitable method for time and space modeling of land covers variations because GIS and remote sensing can be combined with other sciences (Courage and Aniya, 2009). In this regard, remote sensing can be used to prepare a forest plan and monitor spatial and temporal patterns. Satellite images are the best sustainable resource with up-to-date spatial data to estimate deforestation. The Markov chain was presented by a Russian mathematician Andrei A. Markov in 1907. The Markov process is used when the future status of a system can be modeled in general on the basis of the pre-existing state of the system. This method which is now considered as an important method in geographic research, is usually used to predict geographic characteristics with subsequent disruptions (Sang et al., 2011). Markov chain analysis expresses changes in land cover from one period to another, and uses it as the basis for mapping future changes. This work uses the development of a matrix of probability from time one to time two (salman Mahini, et al., 2009). The forecast of land cover changes is calculated as follows:

$$S(t+1) = Pij * S(t) \quad (4)$$

$$Pij = \begin{bmatrix} P11 & P12 & \dots & P1n \\ P21 & P22 & \dots & P2n \\ \dots & \dots & \dots & \dots \\ Pn1 & Pn2 & \dots & Pnn \end{bmatrix}$$

$$(O \le Pij < 1 \text{ and } \sum_{nj=1} Pij = 1 , (i,j = 1,2 , \dots n)) \quad (5)$$

In the relation s (t) and S (t + 1) are the system states at time t and t + 1, and Pij is the probability change matrix 11.

CA: An automated cell model was first designed in the 1940s by two mathematicians called Olam and Newman (Schatten, 1999). Automatic cells are a discrete dynamical system that mode each cell at time t+1 by the position of neighboring cells at time t and in accordance with predefined rules. As a result, geographic status is more important. The CA model is shown in the following formula:

$$S(t, t+1)= f(s(t),N) \quad (6)$$

S is restrictions and discrete cellular states, N number of cells, t and t + 1 different times and f is the transmission of cell status. The CA model is in fact a raster modeling technique in which the cell's state usually represents the cell's surface (Almeida et al., 2008). These models have features such as spatial location and the ability to integrate with other spatial data. Mathematics can be a tool for studying and modeling complex processes.

An important issue in Markov's analysis is that there is no spatial element in this modeling (salman Mahini, et al., 2009). In fact, the Markov model focuses on quantity in predicting land cover variations. Spatial parameters in this model are poor and do not distinguish different types of land cover changes in spatial patterns (López et al., 2001). CA has the capability to have spatial-temporal detection capabilities in combination with sophisticated spatial systems with proper spatial detection capabilities. The CA-Markov model which combines the ability of Markov and CA, is well-suited for predicting spatial and temporal series. Thus, CA-Markov model provides a better simulation of spatial and temporal patterns of land cover variations in a given amount and location (Sang et al., 2011).

In this study, CA-Markov model was used to simulate forest cover changes. After categorizing the images of 2016 and 2017 and using the automatic cells and Markov chain method, predicting vegetation changes in the Andika forests in 2018 was started. Then, using the automatic cell and Markov chain method, the area of the oak forests for the year 2018 was predicted (Figure 7). After entering the classified images, the area of each classified category can be calculated. After this step, using the Markov chain in the Idrisi software, the matrices of the probability of vegetation changes can be obtained (Table 5). Then, the changes in forest area non vegetation cover is calculated (Table6).

Table 5. Probability matrix of vegetation changes on the vegetation of the Andika

Vegetation cover	Non vegetation cover	
0.2202	0.7798	Non vegetation cover
0.5831	0.4169	Vegetation cover

Table 6. Changes in the Andika vegetation cover from 2016 to 2018

Year	**2016**	**2017**	**2018**
Non vegetation cover	129151.16	128489.42	115406.05
Vegetation cover	35223.04	35884.78	48968.15

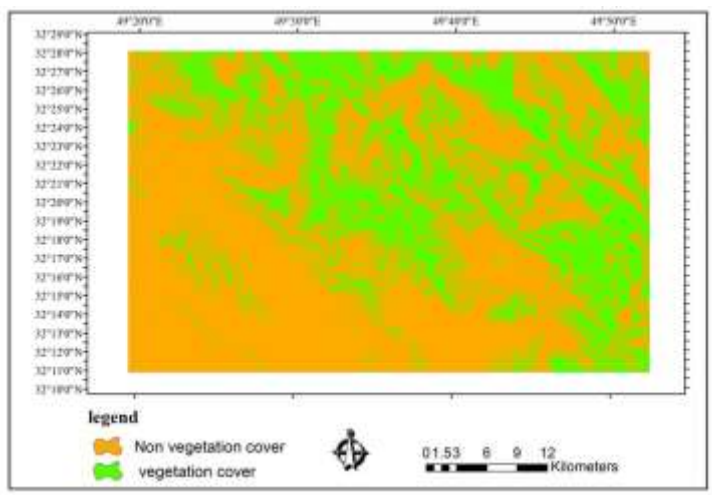

Figure 7. Prediction map of vegetation changes in the Andika region for 2018

4. Discussion

One of the main prerequisites for optimal use of land is the knowledge of land use patterns and changes over time. Principal exploitation of natural resources requires modeling of the region, while observing the instructions of ecological models sustainable development should be taken into consideration.

The results of this study indicate that the integration of remote sensing and GIS techniques is efficient in implementing spatial-temporal variations assessment models to know the type and percentage of land use and the extent of their changes in natural resources and other parts. Planners

of different executive sector can assist in comprehensive management and development (Azizi Ghalati et al., 2015).

This research was carried out with the aim of determining the factors affecting vegetation changes in the forest area in Andika county, Khuzestan province. The vegetation of the oak forest is observed at mountain heights and the mountainous nature of the area prevents urban development and also the possibility of provision of welfare facilities for the inhabitants of the villages. Because access to oak forests in the mountains is difficult, residents of the villages do not harm it and the size of the forests has increased over the course of study. The total area is 164374 hectares, and the amount of land cover changes from 2016-2017 was 661.74 hectares.

The effect of four factors, that are the distance from the road, the distance from the rural residential areas, river and altitude from sea level on the amount of vegetation changes was investigated. Linear regression analysis has been used to determine the relationship between the factors mentioned above and increasing vegetation cover. It can be claimed that there is a significant relationship between independent and dependent variables. Outputs of the regression equation show the effect of independent variables on dependent variables. The value of the determination coefficient of 69.6 indicates a huge agreement between the model and reality. The potential map of region changes and independent variables are shown in Figure 5.

The sensitivity of the multiple regression model can be concluded that the height variable has a decisive effect on the performance of the model because by deleting these variables, the index of the coefficient of determination decreases significantly (Salman Mahini et al., 2011). The coefficient of determination decreased from 0.696 to 5904. The highest vegetation cover is at the mountains height around the Andika which are the oak forests. The vegetation cover increased from 35223 hectares to 35884 hectares from 2016 to 2017. The use of automated cells and Markov chain to predict the vegetation changes for 2018 in the area under consideration, estimated an area of vegetation of 48,968 hectares. In other studies, Similar results and could well examine changes at two different times were presented. Land cover changes in the city of Isfahan were carried out by Safiyanan during the years 1987 to 1998. The results indicate that the level of agricultural land has undergone A significant change (Safiyanian, 2009). Also, in another study, population growth has been the main factor in reducing the vegetation cover and increasing residential utilization (Zairi Amirani and Safiyanian, 2010). In a study using logistic regression method, in modeling the spatial pattern of vegetation change probability in Chehel-Chay watershed in Golestan province, the results showed that variables from forest margin, distance to road and distance to the village, the slope of the earth and the distance to the waterways have been considered most relevant in relation to forest cover changes in the catchment area (Zare Garzi et al. 2012). Modeling the forest area changes and the factors affecting it were analyzed using logistic regression model in Waz and Lavij watersheds. Implementation of logistic regression model in two independent discrete and continuous variables, the coefficients obtained from the implementation of the model in a discrete state indicate the probability of 100 meters from the village (Hosseinzadeh et al., 2013).

It is also possible to change the structure of the HNN algorithm, such as how to initialize, how to apply coefficients for different classes depending on compactness and circularity parameters, how

to change the averaging method of neurons, how to increase and decrease the values of neurons for each repetition and improved algorithm performance.

References

Aslani Moghadam, I. (2012). Evaluation of Cellular Automata Modeling in order to predict landslide changes, Master's Thesis in Civil Engineering, Faculty of Engineering, University of Tehran, 2012.

Adamchuk, V. I., Perk, R. L., & Schepers, J. S. (2004). Applications of remote sensing in site-specific management. University of Nebraska, Cooperative Extension. Institute of agriculture and natural resources.

Almodaresi Al-Husseini, S. A., Karami, J., & Roshan Seyyed, S. (2015). Modeling of Hamedan City Development Using Logistic Regression Method, National Conference on Application of Advanced Spatial Analysis (Remote Sensing and GIS), Islamic Azad University of Yazd.

Aronov, S. (2013). Remote Sensing for Managers, GIS Translation: A. A. Darvish Sefat, Mahtab Pirbaghor, Manizheh Rajabpour Rahmati, Tehran University Press.

Almeida., C. D., Gleriani, J. M., Castejon, E. F., & Soares-Filho, B. S. (2008). Using neural networks and cellular automata for modelling intra-urban land-use dynamics. International Journal of Geographical Information Science, 22(9), 943-963.

Azizi Ghalati, S., Rangzan, K., Taghizadeh, A., & Ahmadi, S. (2013). Modeling of Land Use Change Using Logistic Regression Method in LCM Model (Case Study: Kohmareh Sorkhi Region of Fars Province) Journal of Research in Forest and Poplar Iran. 22(4), 565-596.

Bihamta, M., & Zare Chahouki, M. (2011). Principles of statistics for the natural resources science. University of Tehran Press. 300 (In Persian).

Clark, W. A., & Hosking, P. L. (1986). Statistical methods for geographers. New York: Wiley.

Chang, C. L., & Chang, J. C. (2006). Markov model and cellular automata for vegetation. Journal of geographical research, 45, 45-57.

Courage, k., Aniya, m. (2009). Hybrid classification of Landsat data and GIS for land use/cover change analysis of the Bindura district, Zimbabwe, International Journal of Remote Sensing, Vol. 30, No. 1, 97–115.

Domencich, T. Y. M., & McFadden, D. D. (1975). Urban travel demand: A Behavioral analysis. Amsterdam: North–Holland.

Fallahtakar, S., Sufyanian, A., Seyyed Jamalodin, Kh., & Ziaei, H. R. (2009). The study of the ability of the CA Markov model to predict landslide (Case study: Isfahan city). Geomatics conference articles, Mapping Organization, Tehran.

Ghazalfali, M., & Alawafanah, S. K. (2010). Application of Visual Interpretation of Satellite Data in Detection of Coastal Changes. The 17th National Geomatics Conference, Iran.

Hosseinzadeh, M. M., Derafshiand, Kh., & Mirbagheri, B. (2013). Modeling forest extent change and its influencing factors, using logistic regression model in GIS environment, (case study: Vaz and Lavij basins). Iranian Journal of Forest and Popular Research, 21(1), 86-98. (In Persian)

Huete, A., & USTIN, S. (2004). Remote sensing for natural resources management and environmental monitoring: Manual of remote sensing. Remote sensing for natural resources management and environmental monitoring manual of remote sensing.

Jafarzadeh, A. A., & Arekhi, S. (2012). Analyze and predict processes of deforestation using logistic regression and GIS (a cas e study of northern Ilam forest, Ilam province, Iran). Elixir Agriculture, 44, 7104-7111 (In Persian).

Kamusoko, C., Aniya, M., Adi, B., & Manjoro, M. (2009). Rural sustainability under threat in Zimbabwe-simulation of future land use/cover changes in the Bindura district based on the Markov-cellular automata model. Applied Geography, 29(3), 435-447.

Kamyab, H. R., Salman Mahiny, A., Hossini, M., & Gholamalifard, M. (2010). A Knowledge-Based Approach to Urban Growth Modeling in Gorgan City Using Logistic Regression. Journal of environmental studies, 36(2), 89-96 (In Persian).

López, E., Bocco, G., Mendoza, M., & Duhau, E. (2001). Predicting land-cover and land-use change in the urban fringe: a case in Morelia city, Mexico. Landscape and Urban Planning, 55(4), 271-285.

Matsushita. B., Yang, W., Chen, J., Onda, Y., & Qui, G. (2007). Sensitivity of the Enhanced Vegetation Index (EVI) and Normalized Difference Vegetation Index (NDVI) to topographic effects: A case study in high-density Cypress forest. Sensors, 7(11), 2636-2651.

Mahdavi, A., Fathizadeh, H., Shtaei Joybari, S. (2015). Evaluation and Analysis of Various Methods of Land Use Change / Vegetation Change (Case Study: Manesht Forest Protected Areas of Ilam Province), Journal of Wood and Forest Science and Technology, 21(4).

Salman Mahini, A., Feghhi, J., Nadali, A., and Riazi, B. (2009). Tree cover change detection through Artificial Neural Network classification using Landsat TM and ETM+images (case study: Golestan Province, Iran). Iranian Journal of Forest and Poplar Research, 16: 3. 495-505. (In Persian)

Mesgari, S., & Ranjbar, A. (2003). Analysis and estimation of deforestation using satellite imagery and GIS, Proceedings of Map India, the 6th Annual International Conference and Exhibition, New Delhi, India.

Miranda-Argon, L., Trevino-Garza, E. J., Jimenez-Perez, J., Aguirre-Calderon, O. A., Gonzalez-Tagle, M. A., Pompa-Garcia, M., & Aguirre-Salado, C. A. (2012). Modelling susceptibility to deforestation of remaining ecosystems in North Central Mexico with logistic regression. Journal of forestry Research, 23(3), 345-354.

Mirza'i Zadeh, V., Mahdavi, A., Karimshahi, A., Ja'farzadeh, A. (2016). Investigation of spatial pattern of forest cover changes using logistic regression in Malekhahi city. Journal of Science and Technology in wood and forest, 23(3), 11 (Persian).

Na'imi Nezamabad. Ghahroudi Tali, M., & Servati, M. (2010). Surveillance of Coast Line Changes and Geomorphologic Landforms of Persian Gulf using Remote Sensing and Geographic Information System (Case Study: Asalouyeh Coastal Area), Geographical Space, Tenth Year, 30, 45-61.

Pettorelli, N., Vik, J. O., Mysterud, A., Gaillard, J. M., Tucker, C. J., & Stenseth, N. C. (2005). Using the satellite-derived NDVI to assess ecological responses to environmental change. Trends in ecology & evolution, 20(9), 503-510.

Sang, L., Zhang, C., Yang, J., Zhu, D., & Yun, W. (2011). Simulation of land use spatial pattern of towns and villages based on CA–Markov model. Mathematical and Computer Modelling, 54(3-4), 938-943.

Salman Mahini, A. & Kamyab, H. (2012). Applied Remote Sensing and GIS with Idrisi. Second Edition. Publication of Mehrmahdis. Tehran, Iran, 596 (In Persian).

Safiyanian. (2009). Investigation of Land Use Changes in Isfahan Area Using the Detection Technique of Changes during the Years 1987 to 1998. Agricultural and Natural Resources Sciences and Technology, Thirteenth year, 99, 153-164.

Schatten, A. (1999). Cellular automata: Digital worlds. Retrieved February, 13, 2004.

Sheikh Goodarzi, M., Alizadeh, A., Salman Mahini, A., & Jahangir, J. (2013). Markov Automatic Marker Cells in Simulation of Land Cover Changes. Proceedings of the Geomatics Conference, Mapping Organization, Tehran.

Shojaeai, M., Kiyani, B., Stode, A., & Azim zadh, H. (2017). Investigation of the role of topographic factors in spatial prediction of plant species by using logistic regression. Journal of Quarterly Journal of Khashak Boom, 7(1), 2 (Persian).

Zairi Amirani, A., & Safiyanian. (2010). Study of the trend of changes in land cover and population growth in the city of Isfahan using remote sensing during 1986-2009. The 17th National Geo-Technical Conference, Iran.

Zare Garizi, A., Sheikh, V., Sadoddin A., & Salman Mahini, A. (2012). Application of logistic regression modeling of spatial pattern of vegetation change (case study: Chehelchay watershed Golestan province). Journal of Geographic Space, 12(37), 273-285 (In Persian).

Zebiri, M., & Majd, A. (2001). Introduction to Remote Sensing and Application in Natural Resources, Tehran University Press and Publishing Institute.

Available online at www.jrors.ir

JRORS Journal Of Radar and Optic Remote Sensing

Journal Of Radar and Optic Remote Sensing

JRORS 2 (2018) 55–66

Assessment of Remotely Sensed Indices to Estimate Soil Salinity

Naser Ahmadi Sani [a*], Mohammad khanyaghma [b]

[a] *Assist. Prof., Faculty of Agriculture and Natural Resources, Mahabad Branch, Islamic Azad University, Mahabad, Iran*
MSc of Agroecology, Mahabad Branch, Islamic Azad University, Mahabad, Iran

Received 17 March 2018; revised 4 October 2018; accepted 5 October 2018

Abstract

Soil Salinization is one of the oldest environmental problems and one of the main paths to desertification. Access to information in the shortest time and at low cost is the major factor influencing decision making. The satellite imagery provides information data on salinity and also offers large amount of data that can be analyzed and processed to understand several indices based on the type of the sensor used. In this research, the capability of different indices derived from IRS-P6 data was evaluated to identify saline soils in Mahabad County. The quality of the satellite images was first evaluated and no noticeable radiometric and geometric distortion was detected. The Ortho-rectification of the image was performed using the satellite ephemeris data, digital elevation model, and ground control points. The RMS error was less than a pixel. In this study, the correlation between the bands and used indices, including Salinity1, Salinity2, Salinity3, PCA1 (B2, B3), PCA1 (B4, B5), PCA1 (B1, B2, B3, B4, B5), Fusion (Pan and B2), Fusion (Pan and B3) and Fusion (Pan and B4) with EC were investigated. The highest correlation was related to the Fusion (Pan and B2) with a coefficient 0.76 and the lowest correlation was related to B4 with a coefficient 0.2. The results showed that the indices have a high ability for modeling, mapping and estimating the soil salinity.

Keywords: Indices, IRS-P6, Remote sensing, Soil Salinity

1. Introduction

Salinization is one of the most common land degradation processes in arid and semi-arid areas. It is one of the oldest environmental problems and paths to desertification (Morshed et al., 2016).

* Corresponding author. Tel: +98-9142960454.
E-mail address: n.ahmadisani@gmail.com.

Salinity usually refers to a significant concentration of mineral salts in soil or water because of the hydrological processes (Schofield et al. 2001). There are two main types of salinization: primary and secondary. Primary salinization occurs through the natural processes. Secondary salinization occurs due to poor management practices (Mashimbye, 2013). The effects of salinization can be observed in numerous vital ecological and non-ecological soil functions (Daliakopoulos et al., 2016). Soil salinity can reduce the productivity of affected lands, posing degradation, and threats to sustainable development (Yu et al., 2018).

Planning for each type of activity requires correct and timely information. The required data and information can be obtained in different ways like field inventory and remote sensing. By using field method one can acquire data with the desired spatial and descriptive accuracy, but generally it is time-consuming and costly. In contrast, by using remote sensing technology in several fields, the required data can be quick and efficient (Makhdoum et al., 2009; Ahmadi Sani et al., 2011).

By the launch of Landsat in 1972, remote sensing technology opened a new horizon into the planning and management of different resources. This issue supplies a new method for surveying and estimating different parameters (Alavipanah and Ladani, 2010). In this regard, the role of RS is directly and indirectly proved by providing new chances for using different satellite images and various methods of classifying and mapping (Ahmadi Sani et al., 2011). Remote sensing data are considered to be a convenient source to extract several indices in either simple or complicated band ratio combinations. Satellite images offer a large amount of data that could be analyzed, processed and stored for better understanding of several indices based on the type of the used sensors (Elhag and Bahrawi, 2017).

With saline and sodic soils covering of 93232 million hectares globally, and one of the major soil degradation threats worldwide, with mismanaged irrigation affecting 34.19 million hectares or over 10% of the total irrigated lands, soil salinization is a widespread phenomenon. The excessive accumulation of soluble salts in the soil surface influences soil properties, which decreases soil productivity, limits the growth of crops, and constraints agricultural productivity. Excessive concentration of salts in soil may lead to the abandonment of agricultural land. Globally, the cost of irrigation-induced salinity is equal to an estimated US$11 billions per year (Morshed et al., 2016).

Various remote sensing data are being used for identifying and monitoring salt-affected areas such as aerial photographs, infrared thermography, visible and infrared multispectral, and microwave images (Metternicht and Zinck 2003). Regarding the importance of indices in soil salinity mapping, various researchers have been using different indices (Fernandez-Buses et al., 2006; Morshed et al., 2016). They have introduced different and sometimes similar indices as the best indices for soil salinity evaluation. But results have shown that one can use the indices instead of single and original bands for more exact mapping and information extraction of soils saline. Therefore, in this study the possibility of using some indices of earlier studies was evaluated for soil salinity mapping using IRS-P6 data.

2. Materials and Methods

2.1. The Study Area

The study area is located in West Azerbaijan Province, north of Mahabad County, with an area of about 33,000 hectares. The climate of the area is cold and humid and the average annual precipitation is about 356 mm. Most of the area is allocated to agricultural lands. The major crops in the region are cereals, sugar beet, alfalfa, cucurbits, legumes, apple and stone fruit orchards. Ranges and residential areas also occupy a small percentage of the area.

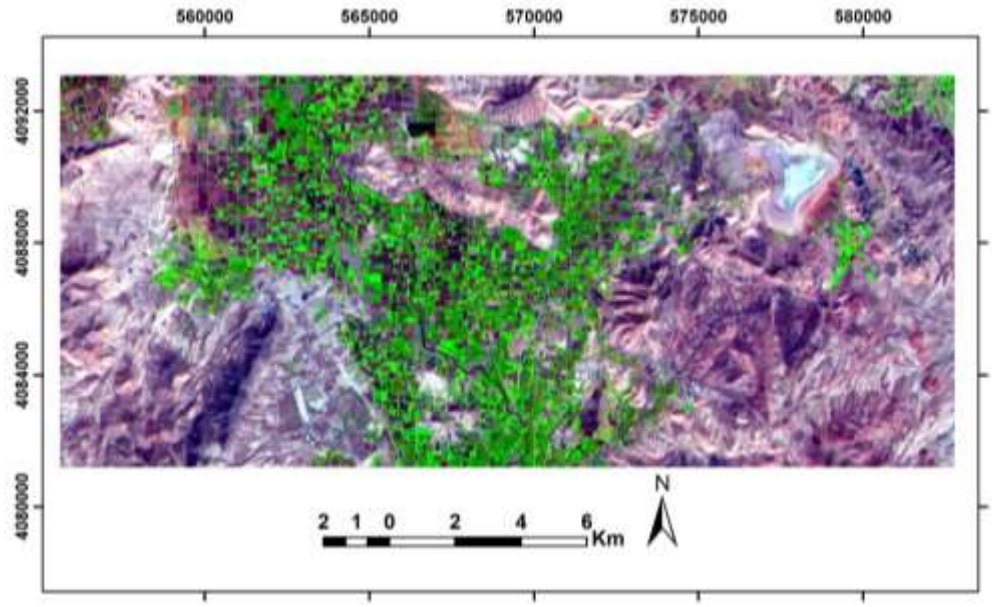

Figure 1. A view of the study area (RGB_{543})

2.2. Methodology

This paper has made an attempt to measure the soil salinity from remote sensing indices analysis. To predict soil salinity, an integrated approach of salinity indices and field data was used. The correlations between different indices and field data of soil salinity were calculated to find out the highly correlated indices. The stepwise regression analysis was done to determine the combination of indices and bands that showed the best correlation with the field EC values. The research method is shown in Figure 2.

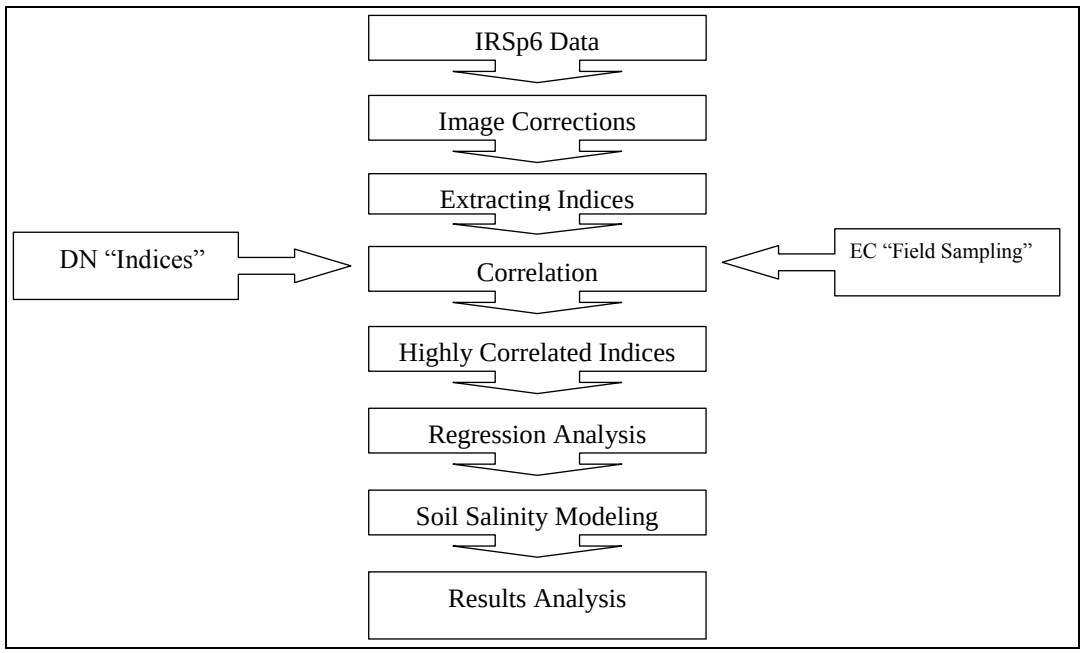

Figure 2. Flowchart of research methodology

2.2.1. Satellite Data

In this research, IRS-P6 satellite data, including panchromatic band and the multi-spectral bands were used. The data were gathered in summer of 2011 because the best images to study the soil salinity are the images that have the least plant cover at the time of imaging the soil.

2.2.2. Data Corrections

All raw satellite data have geometric errors. Radiometric errors are visible if present. In this study, there was no significant radiometric error, and geometric corrections were made in two ways: 1. Images to map using the map of rivers and roads and by the method of Ortho-rectification for the correction of panchromatic band. 2. Using images to image for correction of spectral bands using the corrected band as the basis.

2.2.3. Indices and Synthetic Bands

Many researchers have used various indices to prepare soil salinity maps (Daliakopoulos et al., 2016; Elhag and Bahrawi, 2017; Medjani et al., 2017; Morshed et al., 2016; Fourati et al., 2015; Daempanah et al., 2011; Dashtakian et al., 2008), so some indices are known and can be used in soil salinity mapping. Indices, in addition to increasing the clarity and improving categorization of phenomena, reduce the negative effects of inappropriate factors and the effects of other land covers.

In this research, by applying the methods of Ratioing, Principal Components Analysis and also Fusion in order to import spatial precision of panchromatic band into multi-spectral bands to better fit the true values of salinity and digital values of images in different locations. Therefore, several indices and synthetic bands were developed and used in the analysis.

2.2.4. Soil Sampling

In this research, systematic sampling was used. A regular grid, 1000 × 1000 meter, was deployed by GPS in the area and Surface soil samples were taken. Sampling was done in September to adapt the time between imagery and sampling. The vegetation areas, orchards, inaccessible areas and mountains were eliminated. Finally, 147 samples were taken and the electrical conductivity of each sample in the soil laboratory was extracted. By entering the salinity data (EC) into the grid map table, a point salinity map was prepared.

2.2.5. Extract of the Corresponding Values

After bands correction and preparing of different indices, the vector map of the sampling grid was placed on bands and indices. The pixel digital number which was placed at each sampling point was recorded as the digital number of that point in the images in the ArcGIS environment. This work was carried out for all sampled points and for all the bands in the study area. Finally, the values for each band (main and synthetic), along with the amount of salinity, were entered into the SPSS software for last analysis.

2.2.6. Statistical Analysis

At first descriptive statistics of EC were extracted, including average, mode, mean, and standard deviation, standard error, maximum and minimum. The histogram was then plotted and the data were normalized by log-transforming, which was tested by Kolmogorov-Smirnov test. Finally, correlation, regression, and variance analysis were investigated to verify the significance of the data. Also, the stepwise regression analysis was performed and a salinity model was developed.

Table 1. Used indices and formula

Indices	**Formula**
Salinity1	$(B2 + B3)^{0.5}$
Salinity2	$(B2^2+B3^2+B4^2)^{0.5}$
Salinity3	$(B2^2+B3^2)^{0.5}$
PCA1 (2,3)	The first component of PCA on B2,3
PCA1 (4,5)	The first component of PCA on B4, 5
PCA1 (1,2,3,4,5)	The first component of PCA on B1-5
Fusion (Pan, B2)	Fusion of B2 with Pan
Fusion (Pan, B3)	Fusion of B3 with Pan
Fusion (Pan, B4)	Fusion of B4 with Pan

3. Results and Discussion

Regarding investigations on different bands of IRS-P6 images, no considerable radiometric error was observed. Geometrical correction of images was done using an Ortho-rectification method with RMSE of less than one pixel. The indices were prepared using Fusion, PCA and Salinity indices (Figures 3-5).

Fusion can in general be done at different levels namely pixel level, feature level, object level and decision levels (Subramanian et al., 2006). There are many image fusion methods that can be used to produce high resolution multispectral images from a high resolution pan image and low resolution multispectral images, including component substitution numerical methods, statistical image fusion, multi-resolution approaches and hybrid techniques. Mathematical combinations of different images are among the simplest and earliest methods used in remote sensing (Pohl and Van Genderen, 2017). In this study, numerical method (sum) has been used for fusion of panchromatic and multispectral bands (Figure 3).

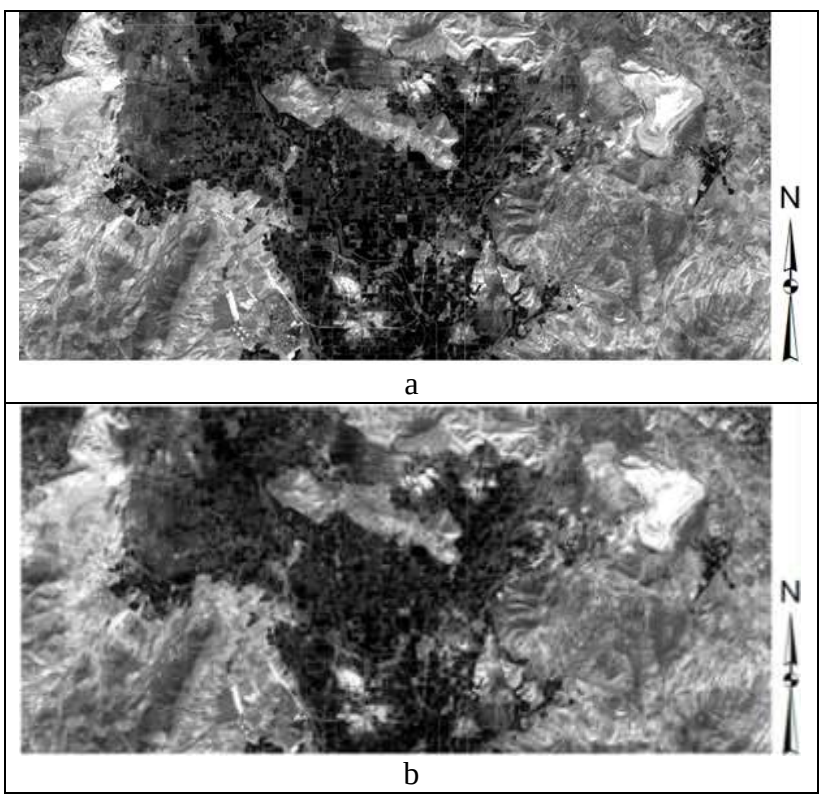

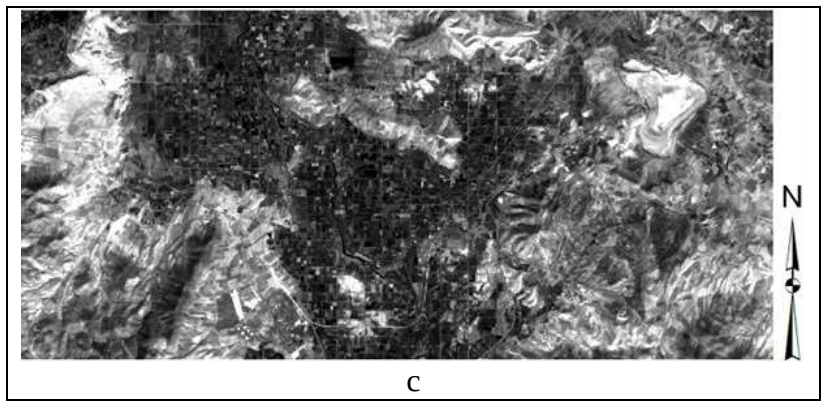

Figure 3. Fusion indices; a (B2 & Pan), b (B3 & Pan), c (B4 & Pan)

The principal component analysis technique was applied to the 4 temporal data sets of SWIR, NIR, Red and Green bands, to de-correlate possible redundant information into some PCs (Pattanaaik et al., 2008). It was found that the first PCs concentrated on most of the information of necessity showing highest variance percentage among all other PCs (Figure 4).

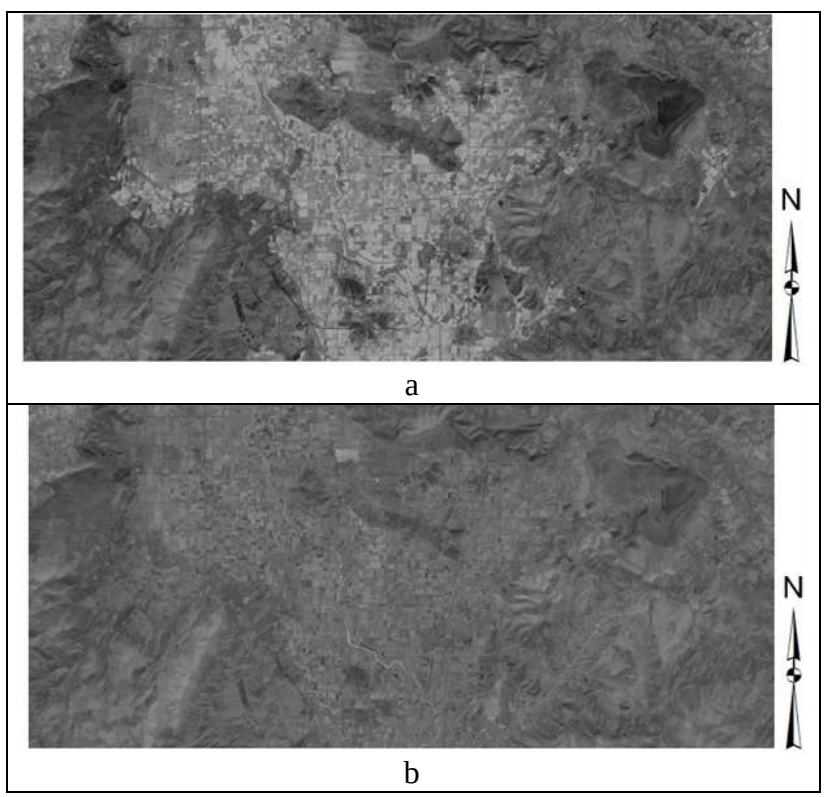

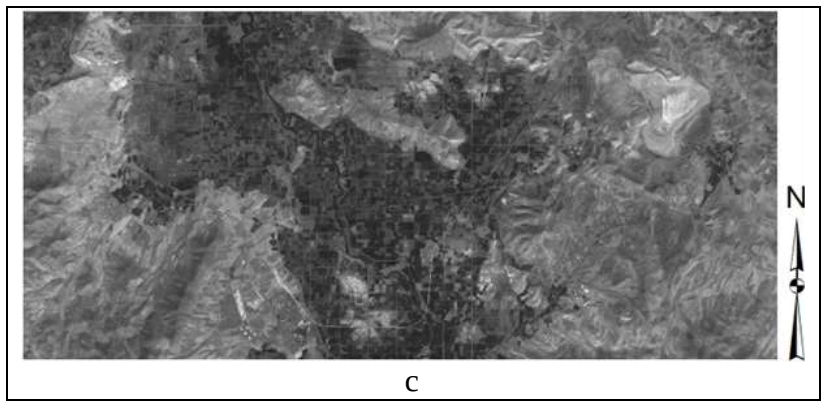

Figure 4. PCA indices; a (PC1B2 & B3), b (PC1B4 & B5), c (PC1B1 & B5)

Soil salinity indices are principally adjusted to detect salt mineral in soils based on the different responses of salty soils to various spectral bands (Elhag and bahrawi, 2017). Among the three computed spectral salinity indices (Figure 5), SI1 offers the highest correlation coefficient (Fourati et al., 2015; Yu et al., 2018).

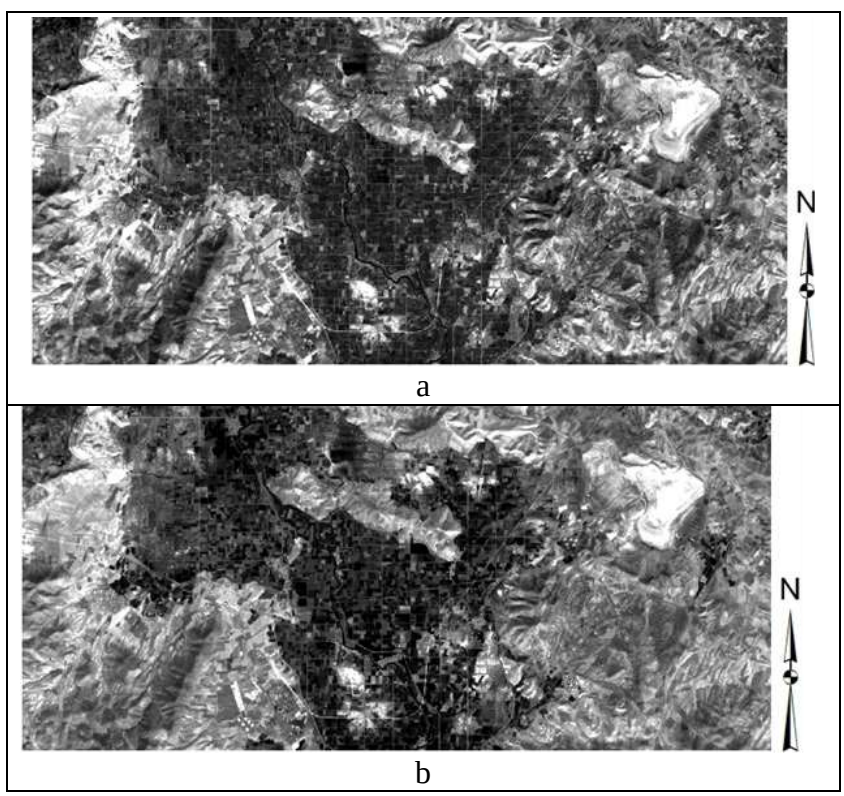

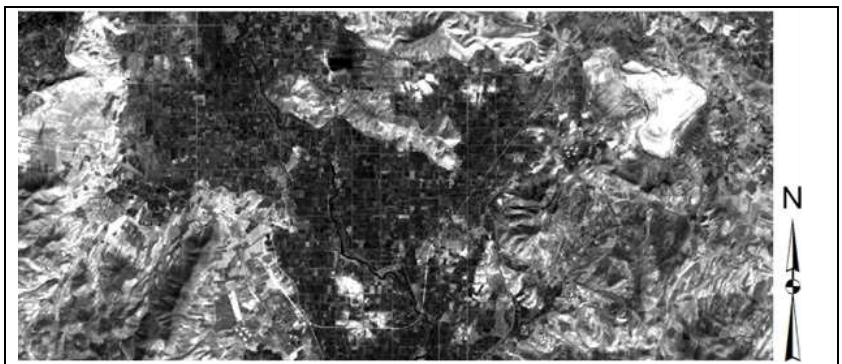

Figure 5. Salinity indices; a (Salinity1), b (Salinity2), c (Salinity3)

As the figures show visually, the fusion index of (Pan, B2) has shown the salinity changes better than other indices. The descriptive statistics calculation of EC showed that the average amount of salinity was 54.7 ds/m and data variance, standard deviation and median were 54, 58 and 87 respectively. The lowest amount of EC was 0.31 and the highest was 26.19and the range of electrical conduction was 25.88.

Comparison of correlation coefficient among main bands and indices with EC showed that B2 (0.73) and (Pan +B2) fusion index (0.76) had the highest correlations. Also, in this research, B4 (0.2) had a very poor correlation (Fourati et al., 2015). Regarding the correlation between bands and indices, highest correlation (0.994) belonged to B3 and salinity1 index (Fourati et al., 2015; Bouaziz et al., 2011) and indices PCA23, PCA45 had negative correlation. The stepwise regression analysis showed a relatively good salinity model in comparison with the earlier research studies (Abdinam, 2004) including only one index (fusion of Pan and B2) with a correlation coefficient equal to 0.628 and Radj equal to 0.39. The regression equation combining remote sensing indices which is shown in Equation 1.

$$Salinity = 0.046 * Fusion\ (B2, Pan) - 0.858 \quad (1)$$

Table 2. Some Correlation Coefficients

Bands and Indices	EC	Pan	B2	B4	Salinity1	Salinity3	PCA1 (1-5)	Fus (Pan,2)
Pan	0.7	1						
B2	0.73	0.88	1					
B4	0.2	0.11	0.26	1				
Salinity1	0.71	0.9	0.99	0.19	1			
Salinity3	0.72	0.9	0.99	0.21	0.99	1		
PCA1 (1-5)	0.72	0.93	0.98	0.26	0.99	0.99	1	
Fus (Pan, 2)	0.76	0.97	0.97	0.21	0.97	0.97	0.99	1
Fus (Pan, 4)	0.66	0.78	0.71	0.68	0.77	0.78	0.83	0.82

The results showed that Pan and B2 bands had the highest correlation with electrical conductivity, so it is reasonable that the fusion index (Pan, B2) has the highest correlation with salinity values. The correlation of EC with the indices used in this research was high except for Fusion (Pan, B4), PCA1 (B4, B5) and salinity2 indices so it could be related to the use of B4 in preparation of these indices; because as the salinity increases, the spectral value of the near-infrared band decreases. The results of regression analysis showed that among all the bands and indices, only Fusion (Pan, B2) index has a significant correlation with salinity changes. The resulting amounts R^2 and Radj do not have any significant difference with the results of other research studies (Fourati et al., 2015; Bouaziz et al., 2011; Tajgardan et al, 2009; Dadresi and Pakparvar, 2007). In the earlier studies, different researchers recommended different bands and indices for salinity evaluation. Therefore, even if one index had no importance in an area, it is possible to be suitable for other areas. It means that in the areas with different salinity, climate, geographical and geological conditions, different indices can describe salinity changes. The best correlation coefficient of satellite data with electrical conductivity changes in this study compared with earlier studies (Abdinam, 2004; Dadresi and Pakparvar, 2007; Bouaziz et al., 2011), showed potential of IRS-P6 data for soil surface salinity mapping. Also, in confirmation of earlier studies, the use of correlation and regression between satellite data with salinity values facilitate soil mapping with less time and cost required (Alavipanah and Ladani, 2010; Meng et al., 2016).

As Table 3 shows, the use of regression and ETM+ data has been more common, so the investigation of the IRS-P6 data capability requires more studies. Moreover, the best bands and indices included SWIR band, PCA indices and salinity indices in different studies (Table 3). There are differences in some studies (Tajgardan et al., 2009; Bouaziz et al., 2011; Meng et al., 2016) for example the near-infrared band is the best band, which can be due to the use of different data and conditions of the studied area, including vegetation type and density. However, this integrated approach has the potential for detecting soil salinity over local scale efficiently and economically (Morshed et al., 2016) and provide tools for soil salinity monitoring and the sustainable utilization of land resources (Yu et al., 2018).

Table 3. Comparison of past studies

Study	Indices	Methods	Data	The Best
Abdinam, 2004	Color Composite (FCC742)	Regression	ETM+	B7
Dadresi and Pakparvar, 2007	Different Ratioings + PCA	Classification	TM	PCA 234-FCC521
Dashtakian et al., 2008	BI-SI-NDSI-YSI	Regression	ETM+	SI
Tajgardan et al., 2009	SI1-3,BI-MSI-PCA-Fusion	Regression	ETM+	B4-FusB4
Daempanah et al., 2011	PCA SI1-SI2- BI-NDSI	Regression	IRS-P6	SI1
Bouaziz et al., 2011	NDVI- SAVI- SI- SI1- SI2	Regression	MODIS	SI2- SWIR- NIR
Fourati et al., 2015	BI-SI-SI1-SI2-SI3	Regression	OLI	SI- SI3
Meng et al., 2016	NDSI- BI- SI- COSRI	Regression	ETM+OLI	NDSI- SWIR-NIR
Morshed et al., 2016	BI-SI1-SI2-SI3-NDVI-EVI	Regression	ETM+	NIR-SWIR-SI2
Medjani et al., 2017	BI-NDVI-PCI	Classification	ETM+	BI -PCA

4. Conclusion

This paper has presented the potential of integrating IRS-P6 data analysis and field survey data to assess and monitor soil salinity over a local scale. The correlations between the field EC and salinity indices is relatively good and about 40%, variation was observed between the field data and predicted EC by the indices analysis. The results compared to other studies showed that depending on the land physiographic, vegetation, climate and land use, the degree of salinity and geology, different sensors, bands, and indices can be used for soil salinity estimation. Therefore, in this study although Pan and B2 bands are highly correlated with changes in the electrical conductivity of soil, fusion index (Pan, B2) gave better results. The results of the indices showed that they are important for improving the accuracy of the soil salinity map. The Use of the hottest month images of the year, due to the maximum evaporation and salt accumulation in the soil surface can be more effective for estimation of soil salinity. The study showed the high-capability of IRS-P6 data to produce a soil salinity map. Also, in addition to simplicity and high precision using correlation and regression methods between satellite data (DN) and soil salinity (EC) facilitates mapping of soil salinity with more efficiency. It is suggested that in the future, data with a wider spectral range, SWIR and TIR bands, along with other indices be evaluated for preparing salinity maps.

References

Abdinam, A. (2004). The mapping of soil salinity using the correlation between satellite data and salinity values in Qazvin plain. PAJOUHESH-VA-SAZANDEGI, 17(3), 33-38.

Ahmadi-Sani, N., Babaei-Kafaky, S., & Mataji, A. (2011, May). Application of GIS and remote sensing in ecological capability assessment studies. 18th Geomatics Conference, National Cartographic Center, Tehran.

Alavipanah, S. K., & Ladani, M. (2010). Remote Sensing and Geographic Information System. Tehran University Press.

Bouaziz, M., Matschullat, J., & Gloaguen, R. (2011). Improved remote sensing detection of soil salinity from a semi-arid climate in Northeast Brazil. Comptes Rendus Geoscience, 343(11-12), 795-803.

Dadresi-Sabzevari, A., & Pakparvar, M. (2007). The trend of desertification using remote and near sensing in Sabzevar. Iranian Journal of range and desert Researches, 14(1), 33-52.

Daempanah, R., Haghnia, G., Alizadeh, A., & Karimi, A. (2011). Mapping of soil salinity and alkalinity using remote sensing and geostatistical methods in Mahvelat city. Journal of Water and Soil, 25(3), 498-508.

Daliakopoulos, I. N., Tsanis, I. K., Koutroulis, A., Kourgialas, N. N., Varouchakis, A. E., Karatzas, G. P., & Ritsema, C. J. (2016). The threat of soil salinity: A European scale review. Science of the Total Environment, 573, 727-739.

Dashtkian, K., Pakparvar, M., & Abdullahi, J. (2008). Investigation of soil salinity mapping methods using Landsat satellite data in Marvast area. Iranian Journal of range and desert Researches, 15(2), 139-157.

Elhag, M., & Bahrawi, J. A. (2017). Soil salinity mapping and hydrological drought indices assessment in arid environments based on remote sensing techniques. Geoscientific Instrumentation, Methods and Data Systems, 6(1), 149-158.

Fernandez-Buses, N., Siebe, C., Cram, S., & Palaci, J. L. (2006). Mapping soil salinity using a combined spectral response index for bare soil and vegetation: A case study in the former lake Texcoco, Mexico. Journal of Arid Environments, 65(4), 644-667.

Fourati, H. T, Bouaziz, M., Benzina, M., & Bouaziz, S. (2015). Modeling of soil salinity within a semi-arid region using spectral analysis. Arabian Journal of Geosciences, 8(12), 11175-11182.

Makhdoum, M., Darvishsefat, A. S., Jafarzadeh, H., & Makhdoum, A. (2009). Assessment and planning of Environment with GIS. Tehran University Press.

Mashimbye, Z. E. (2013). Remote sensing of salt-affected soils (Doctoral dissertation, Stellenbosch: Stellenbosch University).

Medjani, F., Aissani, B., Labar, S., Djidel, M., Ducrot, D., Masse, A., & Hamilton, C. M. L. (2017). Identifying saline wetlands in an arid desert climate using Landsat remote sensing imagery. Application on Ouargla Basin, southeastern Algeria. Arabian Journal of Geosciences, 10(7), 176.

Meng, L., Zhou, S., Zhang, H., & Bi, X. (2016). Estimating soil salinity in different landscapes of the Yellow River Delta through Landsat OLI/TIRS and ETM+ Data. Journal of Coastal Conservation, 20(4), 271-279.

Metternicht, G. I., & Zinck, J. A. (2003). Remote sensing of soil salinity: potentials and constraints. Remote sensing of Environment, 85(1), 1-20.

Morshed, M., Islam, T., & Jamil, R. (2016). Soil salinity detection from satellite image analysis: an integrated approach to salinity indices and field data. Environmental Monitoring and Assessment, 188(2), 119.

Pattanaaik, S. K., Singh, O. P., Sahoo, R. N., & Singh, D. K. (2008). Irrigation induced soil salinity mapping through principal component analysis of remote sensing data. Journal of Agricultural Physics, 8, 29-36.

Pohl, C., & Van Genderen, J. L. (2017). Remote sensing image fusion: A practical guide. CRC Press.

Schofield, R., Thomas, D. S. G., & Kirkby, M. J. (2001). Causal processes of soil salinization in Tunisia, Spain and Hungary. Land Degradation & Development, 12(2), 163-181.

Subramanian, P., Alamelu, N. R., & Aramudhan, M. (2006). Fusion of multispectral and panchromatic images and its quality assessment. ARPN Journal of Engineering and Applied Sciences, 9(10), 4126-4132.

Tajgardan, T., Aioubi, Sh., Shataee, Sh., & Khormali, F. (2009). Soil salinity mapping using ETM+ remotely sensed data. Journal of water and soil conservation, 16(2), 1-18.

Yu, H., Liu, M., Du, B., Wang, Z., Hu, L., & Zhang, B. (2018). Mapping Soil Salinity/Sodicity by using Landsat OLI Imagery and PLSR Algorithm over Semiarid West Jilin Province, China. Sensors, 18(4), 1048.

Available online at www.jrors.ir

JRORS Journal Of Radar and Optic Remote Sensing

Journal Of Radar and Optic Remote Sensing

JRORS 2 (2018) 67–78

Geotectonic Critical Analysis with Emphasis on Active Remote Sensing (ASAR Sensor) Case study: Persepolis

Asghar Daneshmandi [a*]

[a] *Ms in GIS&RS, Yazd Branch, Islamic Azad University, Yazd, Iran*

Received 17 February 2018; revised 12 September 2018; accepted 12 September 2018

Abstract

The main reason for subsidence in Iran is the large amount of water withdrawn from underground resources, which, if not managed properly will cause irreparable damages. To deal with such a problem, it is necessary to identify the subsidence areas. Most country's ancient artifacts have been built on fertile plains, and due to the dryness of the past decade, and the abundance of groundwater from the subsidence, it accelerates the destruction of ancient works in these areas. In this research, the area of Persepolis, which is 57 km northeast of Shiraz and 10 km north of Marvdasht city, is based on the level of the land subsidence using differential radar interferometry technique. Using Eoli-SA 9.4.3 software, two images were taken from the ASVAR data series of the ENVISAT satellite. The data processing with SARSCAPE 4.3 software, a radar differential interference method, has been implemented at two different times in a region. A new image called an interferogram or interferometer was provided that contains the target geophysical information. Therefore, the amount of subsidence or uplift was determined in the three interlaced states. During the research period from 23/12/2004 to 17/12/2009, which is 1820 days, it has been clear that the ancient area of Persepolis, the historic city of the pool and the role of Rustam between two and three centimeters subsided, and the role of Rajab is also between the four has seen up to five centimeters of subsidence.

Keywords: Geotechnical, Radar interferometry, Subsidence, Persepolis

[*] Corresponding author. Tel: +98-9173292153.
E-mail address: dangisrs@gmail.com.

1. Introduction

Earth subsidence is the gradual or sudden collapse of the earth's surface due to the changes in the shape and displacement of particles (Rahman and Kazemifar, 2006), which is affected by natural factors (volcanoes, landslides at the site of disintegrating rocks, stiffness) and human factors (mining, extraction underground water, oil and gas, and construction) (Hunt, 2007).

The phenomenon of subsidence by altering the topographic state of the area can cause significant changes in the hydrology of the region. On the other hand, this phenomenon can lead to abnormal results by altering the aquifer status of the area, such as the direction and the speed of the flow of underwater, underground water basins and so on.

Therefore, the damage caused by the occurrence is suppressed and its phenomena associated includes the anomalous variation in elevation and slope of rivers, waterways and structures of water transfer, and failure or exhaust of the pipe walls of the wells as a result of compressive stresses due to the density. The aquifers and disturbance in the utilization of groundwater resources (Holzer, 1989) are also the advancement of waves in coastal areas and the reduction of groundwater quality and increase in salt water (Hajizadeh et al., 2013). Techno-logical properties of landforms and energy-efficient ones resulting from electromagnetic waves, plays a role in the geomorphological and environmental changes of each region, and determines the controlling factors of landforms. Earth subsidence as one of the consequences of karstization may be created as a sudden subsidence or gradual formation. When the earth's surface moves down gradually, the wider area of the earth subsides and suddenly falls. The dry climatic conditions in most parts of Iran and the increasing use of groundwater resources have provided favorable conditions for this phenomenon (Sharifi Kia, 2011). Also, the persistence of droughts and increased pumping of groundwater resources has expanded this phenomenon in humid areas of western and northwestern Iran (Faladi Moghadam, 2009). Utilization of oil and gas resources in addition to groundwater harvesting has led to the emergence of this phenomenon in the southwest of the country (Haghighat Mehr, 2010). Measuring the magnitude and extent of subsidence through satellite data is a new method in monitoring this phenomenon. In this regard, differential radar interferometry is one of the most accurate and least expensive remote sensing methods. Therefore, its footprint is deserted in the Persepolis area and the deformation analysis spatial and temporal dimension is necessary using the radar differential interference technique in order to manage the incident and to identify and reduce the damage caused by it.

Wang et al. (2011), using COSMO-SkyMed radar images and radar interferometry technology, surveyed the subsidence of the Shanghai metro subway tunnel, whose results showed that the metro caused subsidence at a high rate of 5 to 20 mm per year at most stations. Vincent et al. (2011) have studied the abnormal behavior of ground-level outage caused by the activities of the Chinese Lop-Nin atomic site using radar interferometry, which used ERS satellite radar data between 97-99 and determined that the height of the upper surface is about 2.7 centimeters.

Karimzadeh (2016) drops the Tabriz area using 17 ASAR images and Radar differential interferometry between 2003 and 2010, which shows the results of a residual 4-cm subsidence. Babaee et al. (2016) calculated the subsidence rate of Qazvin plain between 2003 and 2010 by

analyzing the time series of radar images using short-length line and permanent dispersers of 20 to 35 mm per year.

2. Study area

2.1. Location and Geographical Coordinates of Persepolis

Persepolis is built on a mountain cliff of Rahmat Mountain, 57 km northeast of Shiraz and 10 km north of Marvdasht. The structure is 1770 meters above sea level. Geographical coordinates are located along the east 52°53'25" and 29°56'04" degrees latitude. This work was registered on 16 September 1931 with record number 20.

Figure 1. Location of the Jamshid Bed in coordinates 52°53'25" N and 29°56'04" E

2.2. Naghsh-e-Rostam

The Naghsh-e-Rostam is one of the most important historical works of the Elymian, Achaemenid and Sasanian period and is a collection of works made in the heart of the mountain. The Naghsh-e-Rostam and Mount Hajiabad are 5 km north of Persepolis, and it is commonplace for people and their inhabitants to consider the magnitude of their bodies, the figure of Rostam, the famous mythologist of Iran, known as the Naghsh-e-Rostam. In this mountain, there are huge tombs of Kheshayar Shah, Dariush Kabir, Ardeshir I and Dariush II.

2.3. Naghsh-e-Rajab

The Naghsh-e-Rajab is on the slopes of Mount Mehr (Mount of Rahmat), which has been painted on Ardashir Babakan and Shapur I. This work has been registered as number 22 on 16/09/1931. Naghsh-e-Rajab is 3 km northeast of Persepolis in Mount Rahmat.

2.4. Estakhr City

The ancient site of Estakhr City is located 5 kilometers north of the Persepolis. The most important way of connecting Marvdasht plain with Pasargad and Fars with the inner parts of the Iranian plateau, is the modest doors that are the bedrock of the river Pular. The city of Estakhr is located at the entrance to the valley to Marvdasht, and this has given it a superior geographic feature during its establishment. This work has been registered with the number 18 on 16/9/1931 (Pirnia, 2006).

ENVISAT Satellite

The study has used ENVISAT Europe satellite imagery with a brief description. The ENVISAT satellite was orbited from 2002 to early 2012. It has a repeating orbital period of 35 days with spatial resolution of 30 meters. The monitors installed on the ENVISAT satellite include ASAR MERIS, GOMOS RA-2, AATSR, SCIAMACHY, MIPAS, MWR, LRR and DORIS.

The selection of ASAR images should be out of snow and ice time, the ASAR sensor works in the C band, which is reflected by snow surface. Therefore, there is no vegetation during winter to check proper land subsidence. The selected images are related to the months with low vegetation and snow on the ground.

3. Research Methodology

3.1. Data collection and stages of work

First, using EOLI 9.4.3 software, two images of the ASAR data series of the ENVISAT Europe Satellite C Data Band were taken for specific dates. The data processing has been done with SARSCAPE 4.3 software with the use of differential interference method Radar which is suppressed by the region. The GPS has been used to accurately select the ground subsidence points.

By selecting ASAR sensor images from ESA website and matching the coupled images of Slave and Master geometrically, Radiometry and Radar, an initial preparation of interferometer from the region, and removing the topographic effects and restoring the remaining phase by the SARSCAPE 4.3 software has been conducted, Extracting the phase associated with the earth surface deformation, and eventually obtaining the map of subsidence of the region. Also, the variables studied in the form of a conceptual model and description of how to examine and measure the variables has been shown in Figure 2. The figure also shows the method and the selected images for

this research with track number 142 and shooting time between 18:31 and 18:32. The calculation period for the subsidence is 1820 days from 23/12/2004 to 17/12/2009).

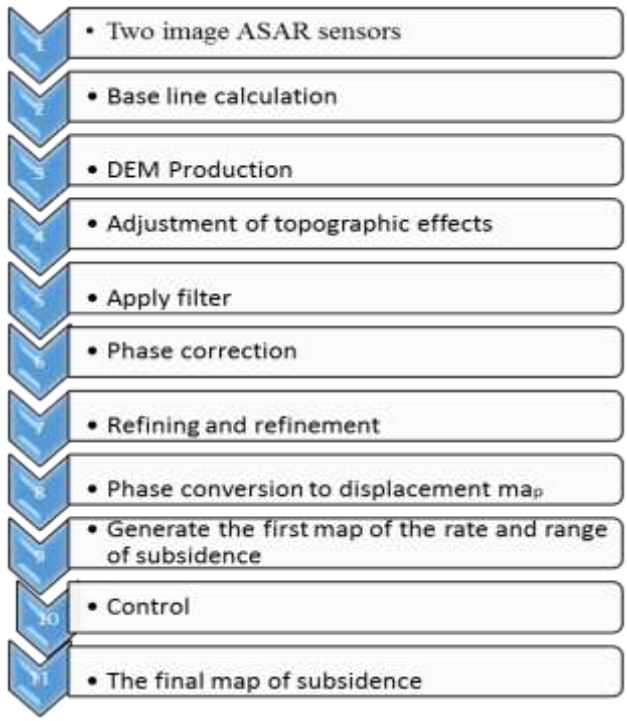

Figure 2. Research methodology flowchart

4. Data analysis method

In this project, after obtaining ASAR image sensors during the period 2002-2012 and the digital elevation model with a spatial resolution of 90 meters as the altitude for eliminating topographic effects, and using the SARSCAPE 4.3 software, the ENVI 4/8 platform changes the gap between ground and radar photographer along the satellite's line of sight with a precision of the fraction of the radar wavelength (cm or millimeter) during the data entry step into the software, measuring the base line, creating the DEM, eliminating the effects of the topography, applying the filter, correcting the phase. The phase transformation to the map of the displacement was fine-tuned the initial map of the rate and the range is generated, controlled and measured. Finally, in order to analyze and identify the area of high risk sites, minimum and maximum subsidence has been prepared. For this purpose, the D-InSAR image pair is selected based on two principles:

1. Time difference between images
2. The vertical line with the distance between the circuits, the shorter of which is the score type

4.1. Data used

ASA_IMS_1PTDPA20041223_183202_000000162033_00142_14725_9198.N1
ASA_IMS_1PTDPA20060216_183156_000000162045_00142_20737_9202.N1
ASA_IMS_1PTDPA20071108_183156_000000162063_00142_29755_9201.N1
ASA_IMS_1PTDPA20091217_183147_000000162085_00142_40777_9200.N1

For ASAR sensor data, orbital modification is needed to be introduced separately. The satellite in its orbit is free-fall and diverges from its orbit for various reasons, such as the moon, The sun, etc. The process of orbital correction is such that by moving the sensor called DORIS, the ASAR circuit rotates within 24 hours and corrects the satellite circuit with a 0.1 mm accuracy with the help of land sensors working with LIDAR. Therefore, for ASAR sensor orbital correction, DORIS sensor files should be used with 24 hours' time difference.

The DORIS files required are as follows:

DOR_VOR_AXVF-P20120424_170100_20041223_215528_20041225_002328
DOR_VOR_AXVF-P20120424_205700_20060216_215527_20060218_002327
DOR_VOR_AXVF-P20120425_164900_20071108_215527_20071110_002327
DOR_VOR_AXVF-P20120425_223600_20091217_215526_20091219_002326

The XCA file was used to modify the parameters of the satellite orbit and data sources prior to 2005

ASA_XCA_AXVIEC20070130_111449_20040412_000000_20050101_000000

4.2. Baseline

The baseline is based on two types of time line and spatial basis lines. The time line represents the duration of the images. If the time interval is too large, it increases the lack of correlation and reduces the phase coherence between the two images (Liu et al, 2013). The spatial basis is the distance between the two transmissions of the sensor. To test the subsidence, one needs to use images that have a zero point of reference. The table below shows slave and master images, as well as the intervals of each one (Table 1)

Table 1. Radar images and their titles

R	Date image master	Date image slave	Time interval (day)
1	2004/12/23	2006/02/16	421
2	2006/02/16	2007/11/08	630
3	2007/11/08	2009/12/17	770

The information provided after calculating the baseline by the software includes:

Normal Baseline: The distance between two satellites when shooting.

Critical Baseline: Maximum allowed space for two satellites.

Ambiguity height

Range shift: Displays the Range value of the Master image to the Slave

Azimuth shift: Shifts the master image to the slave in Azimuth.

Doppler Centroid difference: By placing the Doppler gravity center of the images, the slave indicates the difference between the slave and the master.

The values obtained for the Baseline are images complying with the table below (Table2).

Table 2. A coupled picture base line

Date of the images	Couple image number	Normal Baseline (m)	Critical Baseline (m)	2PI Ambiguity height (m)	Range Shift (pixels)	Azimuth Shift (pixels)	Doppler Centroid diff
2004/12/23 2006/2/16	A	136.623	2157.670	135.105	-14.267	22.993	-4.169
2006/2/16 2007/11/8	B	335.859	2157.584	54.958	-31.932	21.654	-12.485
2007/11/8 2009/3/12	C	307.722	2157.537	59.982	-26.118	9.140	-4.123

5. Results

5.1. Results of the subsidence between 2004-2006

Between 2004 and 2006, the area drops to a maximum of 12 centimeters and has seen 10 centimeters above ground level. The greatest amount of subsidence related to the coordinates are 29^{o} 56' 11" N and 52^{o} 51' 21" E. During this time, the center of the ancient temples of Persepolis was between two and three centimeters. The northern region of these areas fell between three to four centimeters, the northwest and north-east between two to three centimeters subsided, as well as forest park between one to two centimeters subsided. The ancient Naghsh-e-Rajab and its northern and western regions subsided between 2.5 to 3 centimeters, and the eastern, southeast, and southeast regions subsided between 3 and 3.5 centimeters. The historical and ancient Estakhr city has been down between two and nine to three centimeters. The study revealed that the northern, northeastern and northwest parts of Naghsh-e-Rostam were between five to six centimeters high and southern, southwestern, and southeast areas four to five centimeters above the surface. During this period, most of the regions were between two and four centimeters.

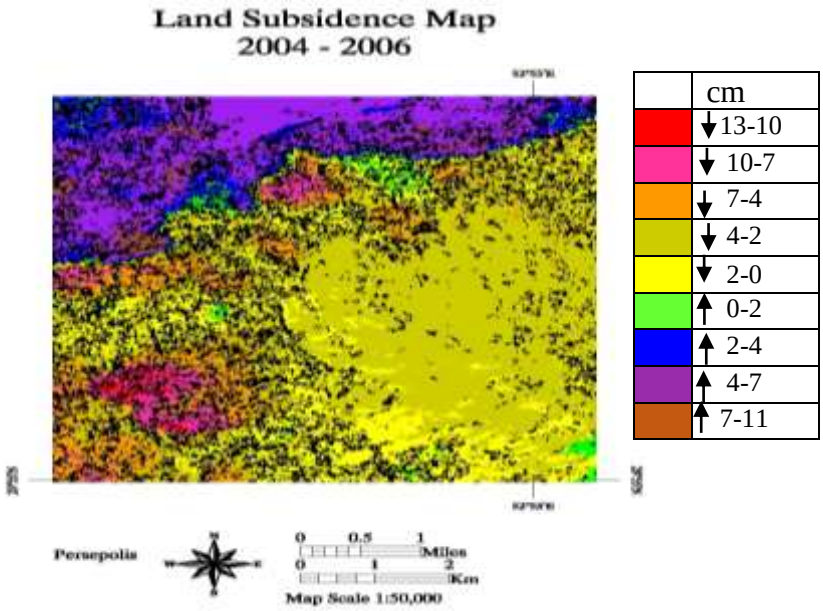

Figure 3. Subsidence between the years 2004 to 2006

5.2. Results of the subsidence between 2006-2007

Between 2006 and 2007, in this region, the largest amount of 8-meter subsidence is related to the coordinates of 29° 55' 23" N and 52° 55' 11" E. It is noteworthy that during these 630 days the maximum surface area has been two centimeters and the study area had an average of one centimeter subsidence. During this time, the center of the ancient temples of Persepolis was between zero and one centimeter. The northern, southern, eastern and western parts subsided between zero and one centimeter and also a forest park between one and two centimeters subsided. The ancient artifacts of Naghsh-e-Rajab and its surrounding areas dropped from zero to one centimeter. And the historical and ancient Estakhr city has been between zero and one centimeter of subsidence. The study found that the ancient area of Naghsh-e-Rostam, other than its northern parts, between 1 and 2 centimeters, has been observed, and in other areas with a maximum of one centimeter subsidence. During this period, most areas had subsided from zero to two centimeters.

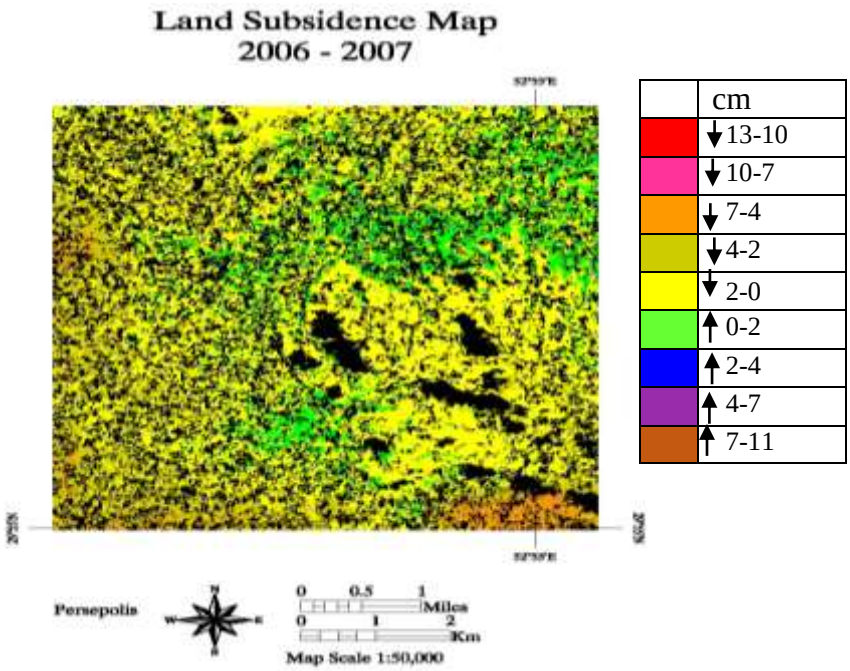

Figure 4. Subsidence between the years 2006 to 2007

5.3. Results of the subsidence between 2007-2009

In this study, it was found that between 2007 and 2009, the area had the lowest subsidence compared to previous years. During the 770 days in the third pixel of the images, the maximum abandonment is related to the coordinates of 29° 58' 42" N and 52° 51' 26" E to seven centimeters and the maximum area elevation during this period was three centimeters. During this period, the average changes were zero and the changes in the Persepolis are as follows:

The collections of works and the northern, southern, eastern and western areas, as well as the forest park between zero and 0.5 centimeters, have been the lowest in recent years. The Naghsh-e-Rajab's collection has subsided between zero and 0.5 centimeters in this period. Also, the collection of the historical Estakhr city, like Naghsh-e-Rajab between zero and 0.5 centimeter, has been abandoned. The study revealed that the ancient area of Naghsh-e-Rostam and the northern, eastern and southern parts of Naghsh-e-Rostam were between 2 or 2.5 centimeters, and western regions between 2.5 to 3 centimeters subsidence. The northeastern parts of this work had dipped between 3.5 to 4 centimeters. It is worth mentioning that black points are points without information in radar images.

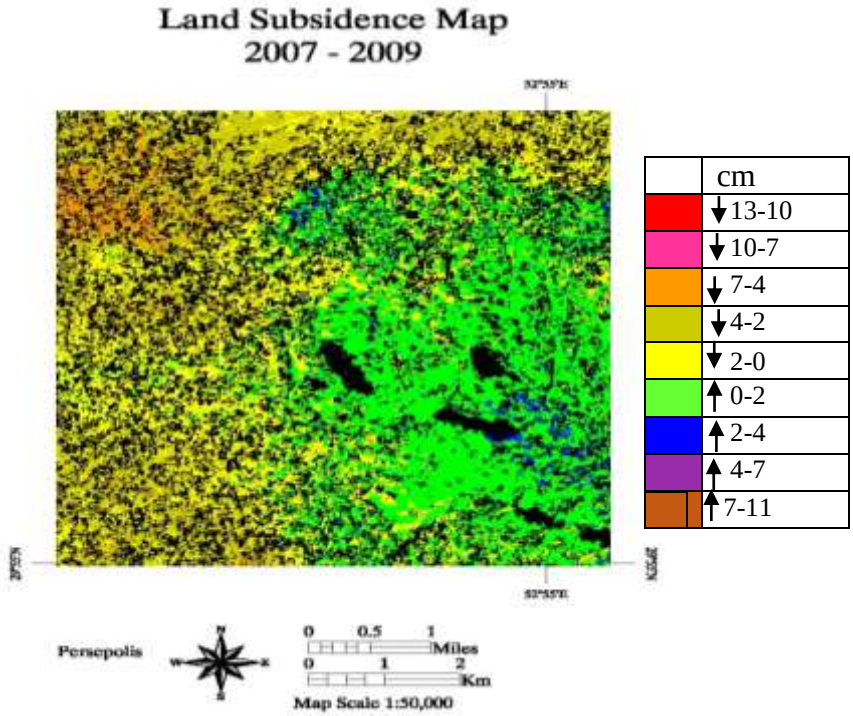

Figure 5. Subsidence between the years 2007 to 2009

5.4. **Conclusion**

The figure shows1820 days. The maximum descent of thirteen centimeters corresponds to the coordinates of 29° 56' 12" N and 52° 51' 36" E, with a maximum height of 8 centimeters. The entire region has generally dropped by three centimeters. During this period, the ancient area of Persepolis fell between two and three centimeters, and the southeastern region subsided between zero and one centimeter and the northeastern region between three and four centimeters. There is also a forest park between two or three centimeters of subsidence.

During this time, the historical Estakhr city and the surrounding area was between two to three centimeters subsided. In this research, it was found that Naghsh-e-Rostam area was between two and three centimeters, which according to the climate of this region in 2004 to 2006, the subsidence of the region is more than other regions. Naghsh-e-Rajab subsided between four and five centimeters and its southeastern sections between three and four centimeters and southward between two and three centimeters.

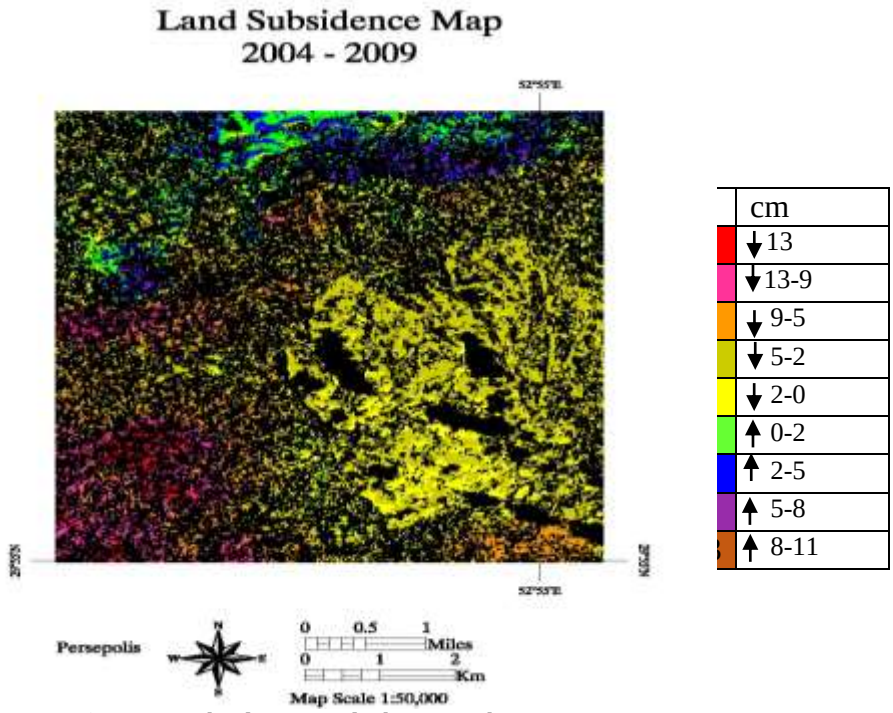

Figure 6. Subsidence results between the years 2004 to 2009

With the addition of three layers of paired images, the image shows the amount of dying between 2004 and 2009. besides, it should be noted that in each image, the pixel value is NONE. In the overall image, its pixel value is also NONE, so in the overall image, the number of points with NONE value is more than other images.

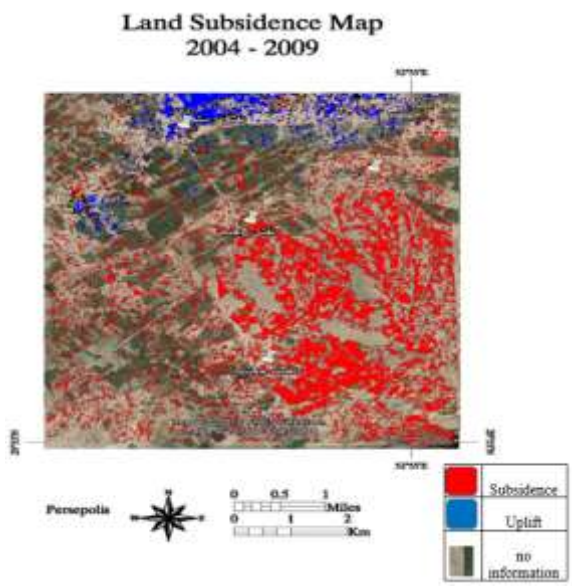

Figure 7. Subsidence of the region between 2004 and 2009

It is seen in Figure 7 that during the research period (i.e.1820 days) most of the areas have been abandoned which is shown in red, and the blue sections represent the areas that were on the highway during that time. With regard to the elevation of these areas due to the isostatic law, it can be concluded that, the only reason for subsidence is not due to the underground groundwater. It is worth noting that these areas are the northern mountains of Naghsh-e-Rostam. It should be noted that this is the first research on subsidence in the flat area of the oblast, and there are no other studies for comparing the results.

References

Babaee, S. S., Mouavi, Z., & Roostaei, M. (2016). Time series analysis of SAR images using Small Baseline Subset (SBAS) and Persistent Scatterer (PS) approaches to determining subsidence rate of Qazvin plain. Journal of Geomatics Science and Technology, 5(4), 95-111.

Foladi Moghadam, N. (2009). Determination of the rate of land abandonment in the Aghajari oilfield based on differential radar interference. (Master's Thesis), Shahid Beheshti University, Tehran.

Haghighat Mehr, P. (2010). Study of land subsidence due to extraction of groundwater and oil wells using differential radiative interference method (Radar Master's thesis), Khaje Nasir University, Tehran.

Hajizadeh, A., Nezam Mahalle, M. A., Saeed, F., Rastegar, A. & Seyed Rezaei, H. (2013). Fundamentals of Microwave Remote Sensing (Radar Interference) with Emphasis on Earth Sciences, Satellite Publishing, Tehran.

Holzer, T. L. (1989). State and local response to damaging land subsidence in United States urban areas. Engineering Geology, 27(1-4), 449-466.

Hunt, R. E. (2007). Geologic hazards: a field guide for geotechnical engineers. CRC Press.

Karimzadeh, S. (2016). Characterization of land subsidence in Tabriz basin (NW Iran) using InSAR and watershed analyses. Acta Geodaetica et Geophysica, 51(2), 181-195.

Liu, P., Li, Z., Hoey, T., Kincal, C., Zhang, J., Zeng, Q., & Muller, J. P. (2013). Using advanced InSAR time series techniques to monitor landslide movements in Badong of the Three Gorges region, China. International Journal of Applied Earth Observation and Geoinformation, 21, 253-264.

Pirnia, H. (2006). History of Ancient Iran, World Book Publishing, Tehran.

Rahman, M. Kazemifar, F. (2006). Earth subsidence due to the drop in groundwater level in Rafsanjan plain, National conference on Irrigation and Drainage Management, University of Chamran, Ahvaz.

Sharifi Kia, M. (2011). Investigation of the Consequence of the Subsidence Death in the Lands and Residential Plots of the Country. Journal of Engineering Geology, 1(2-3), 43-58.

Vincent, P., Buckley, S. M., Yang, D., & Carle, S. F. (2011). Anomalous transient uplift observed at the Lop Nor, China nuclear test site using satellite radar interferometry time-series analysis. Geophysical Research Letters, 38(23).

Wang, Z., Perissin, D., & Lin, H. (2011). Subway tunnels identification through Cosmo-SkyMed PSInSAR analysis in Shanghai. In Geoscience and Remote Sensing Symposium (IGARSS), 2011 IEEE International (pp. 1267-1270). IEEE.

Available online at www.jrors.ir

JRORS
Journal Of Radar and Optic Remote Sensing

Journal Of Radar and Optic Remote Sensing

JRORS 2 (2018) 79–93

Investigating the role of duality in geomorphology using radar data in Bahadoran plain of Yazd

Hamed Piri [a*], Abolqasem Amir Ahmadi [b], Hamed Adab[c]

[a] *Member of young researcher club, Islamic Azad university, Safadasht Branch, Tehran,Iran*
[b] *Associate Professor of Faculty of Geography, Hakim University of Sabzevar*
[c] *Assistant Professor of Faculty of Geography, Hakim Sabzevari University*

Received 23 May 2018; revised 22 September 2018; accepted 22 October 2018

Abstract

Many varied attitudes exist about how the changes occur in the land-surface from the time of William Davis's research to the latest researchers in the history of geomorphologic philosophy and many different terms are used by scientists in order to observe their ideas related to geomorphic phenomena. The phenomenon of duality has been seen less in the geomorphology field. There exist some contradictory phenomena in nature, but further investigation can show their correlation clearly. Durability can be considered as a better dynamic entropy. In this research, radar interferometry technique has been used in Yazd-Bahadoran area and the amount of subsidence and uplifting has been investigated Through field and library studies and the results have been compared with the other researchers' studies, which is a new concept in the literature of geomorphology under geo-duality. The study results indicate that the main reason for the subsidence was not to cut down the level of groundwater, and in this regard the tectonic movements play a significant role. Also, the study shows a significant relationship between subsidence in the Bahadoran plain and the collapse in adjacent heights in terms of duality or dichotomy.

Keywords: Subsidence, Uplifting, Duality, Geomorphology, Radar images

[*] Corresponding author. Tel: +98-9124598597.
E-mail address: pirihamed@gmail.com.

1. Introduction

Land subsidence due to groundwater extraction has been known as a major problem with environmental impacts in many areas. The effects of subsidence due to inappropriate groundwater abstraction, geological factors and groundwater are also very effective. The porosity of the aggregates of the soil layers, density, type, kind and composition of the layers, the pumping method, the geological structure of the area, the hydraulic conductivity of the layers, rainfall and temperature, are the factors affecting the subsidence of the land (Akbari et al., 2009).

Excessive groundwater abstraction leads to a drop in groundwater level and a decrease in fluid pressure resulting in an increase in particle pressure, which leads to a density and a phenomenon of subsidence of the earth.

In Iran, almost a thirty-year history has been related to land subsidence, If this phenomenon occurred only in some of the provinces, such as Kerman and Yazd. Also the present field of Isfahan, Khorasan, Tehran, Tabriz, etc., are subsiding and this problem increasingly occurs in Governments which are more prominent (Ghani Ardekani and Maleki, 2016). Among all the downsides which occur in Iran, the extraction of underground water is the most important factor for land subsidence.

The Iranian plateau is located at the site of Saudi Arabia, India and Eurasia. The intersection of these folios has caused alteration to the shell of the Iran plateau which is surrounded by wrinkles and mountains, such as the Zagros in the west and southwest, the Alborz and Kopeh Dagh in the north and northwest, and the mountains of east and south east (Makran) which have a high seismicity. With the advent of techno-movement that has existed for many years in different parts of the terrestrial zone, the uplifting or rise can be seen (Adib et al., 2016) at the end of the altitudes more often, and sometimes elsewhere in Iran.

To identify the fault patterns in the Zagros; three geological sections are depicted to estimate the elevation during the fault of Zagros. Zagros faults indicate the general state of tectonic movements in the course of a natural fault (Monserrat et al., 2014). In this region, fault patterns and lithogenic curves indicate a reversal of tectonic movements during the old faults. Considering the geological sections and stratigraphic sections and the age of the Zagros fault, the minimum vertical fault velocity from the beginning of sedimentation of Bakhtiari formation in Zagros is 2.05. 01 mm per year (Hakimi, 2015).

When the lithosphere is compressed and moves to occupy less space, the stones are crushed, bent, eaten, or moved upwards. Conflict with horizontal structure has been due to the ground forces and by horizontal and vertical curvature and folding forces which can be and seen in different forms of anticline and syncline. Broken bubbles or hot spots: These low-density forms move upwards, sometimes up to 3,000 kilometers. The active processes in the cones influence their evolution and therefore can consider the movements of the faults and the displacement of the earth's surface. Investigating Maroon basin characteristics in the southwest of the country regarding tectonic and geologically new changes indicate that the uplift in this region is very active and tectonic has a great influence on settlements and land forms (Maqsoudi et al., 2018).

There exist both different and separate phenomena interacting upon each other in nature. In many cases the association of these phenomena is expressed as solidarity and one can also measure these relationships through mathematical methods. Among them, one can find a pair of phenomena

having some connections to each other (Pourkhosrowani, 2015) but these relationships cannot be suggested as a matter of solidarity, and their connection in terms of feature between them has been raised as duality. Duality describes a connection with symmetry, operating in an opposite direction and the expression of a certain proportion can be considered as one of its characteristics. Each scientific theory presented by the scholars of world is characterized in terms and metaphors that follow the structure and patterns of the technique. Therefore, the structure and technical patterns are based on concepts, basic patterns, literature, and theories. In different sciences, the processing and conversion of the basic words of this science is required. Here it is possible to refer specifically to the duality.

Radar interferometry (InSAR) has also been widely considered in recent years as one of the non-geodetic methods with regard to the advantages of other methods (Cigna et al., 2012). This method among ground and space methods is considered as the most efficient method for measuring ground changes with high precision and spatial resolution. Its advantages are of high precision (Monserrat et al., 2014) wide coverage, high spatial resolution, and the lack of need for field work, cost-effectiveness, and the ability to access information in any weather conditions. In Iran, in the past few years, this method has been used to monitor earth's deformations. But to date, the ability of the radar interferometry technique in studying earth's deformations in comparison with the observations of the global positioning system has not thoroughly and extensively been evaluated. One of the reasons is the limited number of permanent GPS stations in the geodynamic network of Iran. The study of the ability and precision of this method seems necessary in measuring the displacement of the surface of the earth.

The purpose of this study is to investigate the duality using the radar interferometry method in Bahadaran plain of Yazd. The research hypothesis is that the correlation between subsidence and uplifting is significant in the study area - duality.

Case Study: Central Plain of Iran-Bahadoran Yazd

This area is in a geographical position of 54 degrees and 30 minutes to 55 degrees' east longitude and 31 degrees to 31 degrees 30 minutes the north latitude which surround the southern quarter of Yazd (Figure 1). Yazd and Mehriz cities are in the northwest. The pomegranate sheriffdom is part of the southeast. The climate of this area whose name is derived from Bahadoran village, is like a desert climate with high temperatures, low humidity and high vaporization. Its maximum temperature reaches to +48°C and reaches a minimum temperature of -15°C and its precipitation reaches to about 60-70 mm per year. This area does not have a river and agricultural activities are carried out through the aqueducts. The morphology of roughness is divided into three groups: slopes, plains and heights. The stone units of this area are mostly northwest-southeast which its northern side is towards Bahadoran and the southern and central parts of Pariya basin. These basins are located in hollow, therefore it is the location of waters flow in which a lot of salt remains due to high evaporation a lot of salt remains (Figure 1).

The second unit produces quaternary acquaillite of alluvial tributaries that at the time of precipitation makes the existing streams. The high and rugged mountain ranges are the third unit formed by the carbonate formation of Taft.

The highest point of Kermanshah Mountain is at 2890 meters and the lowest elevation is Bahadaran plain with a height of 1427 meters. Geologically, Paleozoic rocks are seen in a few hills scattered in the Bahadaran plate and Jamal formation. The most extensive expansion of these rocks is from the northwest to the southeast, called Taft formation.

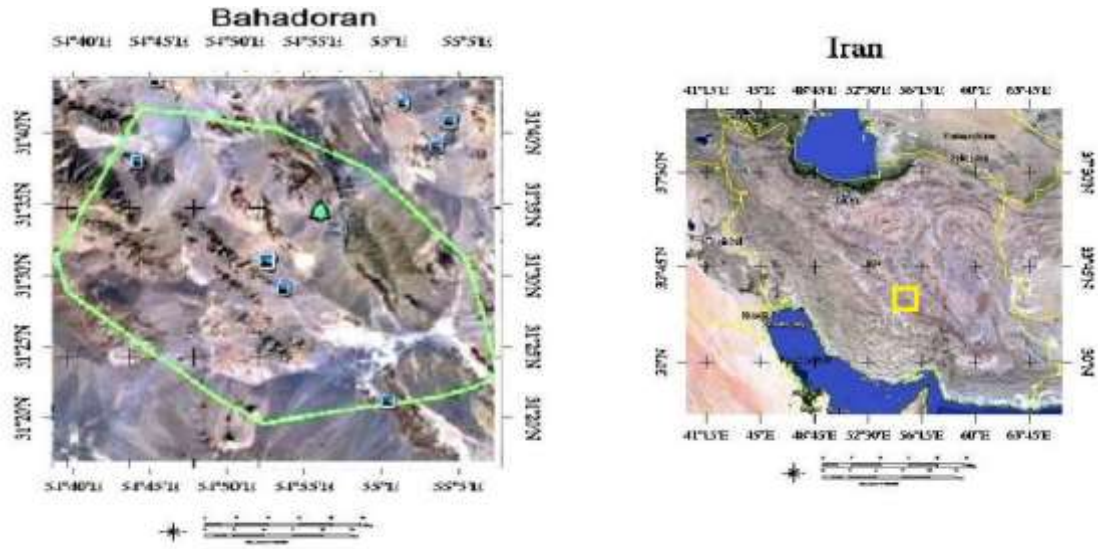

Figure 1. The studied area (Bahadoran plain of Yazd)

2. Materials and methods

Radar interferometer technique is one of the most powerful tools for monitoring the subsidence phenomenon (Buck, 2011). By comparing the phases of two radar images taken from a region at two different times, this method is able to determine the changes in the surface of the earth at that time interval. The phase is taken from an earth fault, proportional to its distance to the radar sensor. therefore, creating a change in this distance affects the measured phase by using image of a Radar interferometer technique by the name of a constructed interferogram. An interferogram is an image that contains a phase difference of two radar images which are recorded geometrically to each other (Yarahmadi et al., 2015). The interferogram phase contains topographic effects, orbital errors and atmospheric effects. In order to obtain the displacement of the earth's surface over a period of time, the orbital errors, the effects of the topography and atmospheric noise should be eliminated from the interferogram. To eliminate topographic effects, the SRTM digital elevation model is used with a spatial resolution of 90 meters. The atmospheric error can be modified with the help of atmospheric information and atmospheric model (Hakimi, 2015).

The use of synthetic aperture radar images (SAR) began to detect ground-level displacements at below centimeter grades late in 1980s, which ended in introducing radar interferometry method (element). This method has become a powerful tool for analyzing the tectonic movements of the earth's crust because it is able to accurately measure the earth's surface in a wide range, high spatial resolution, and also it is less time consuming and saves expenses in this regard. Interferometry of multiplication a mixed image SAR IN second-conjugate image is produced and creates an interferometric image and the phase of this image is the phase difference between the images.

In the atmosphere that leads to a change and creates an extra phase in the whole illustrated, these limitations make it difficult to use conventional radar interferometry (Eslamizadeh and Samanirad, 2010).

In 2000 & 2001, it was discovered that there are problems on the ground that, over time, their dispersal features are constant and are not influenced by factors such as long base and spatial time. Also, in areas with high roughness, the correlation between radar images is affected by the viewing angle and direction; the phenomena that have a dominant and stable replay over time are less affected by the lack of correlation. The researchers showed that if these effects were detected on the surface of the earth, it would not only be possible to monitor the displacement of the earth's surface at these points, regardless of the lack of correlation of radar images (Shirani et al., 2014) but also the effect of other harmful components on interferometric results including atmospheric effects and error associate to the digital earth model can be estimated and eliminated. There are some methods by which the stable dispersers are detected and the amount of surface displacement on those points is monitored. The technical specification of the (SAR) radar with artificial pore coherent imaging (phase data recording alongside the backward amplitude wave) and high-resolution images of the SAR marker create a high spatial area. On the other hand, the randomized phase image is basically random; the weighted average of the phase delay between sending and receiving all dispersions on the ground is in pixel But the difference in the phase between the two images can be as a change in the distance from the satellite to the earth, provided that the spatial distribution properties of the earth remain almost constant. In the interferometer of the rotational phase of the images taken from different shooting situations or shooting times, pixel to pixel are compared. By differentiating between these values, a new image is obtained which is the name of the interferometer. The final phase created in the interferometer which contains additional terms, is as Equation1:

$$\phi int=W\{\phi def+\phi atm+\phi orb+\phi \theta+\phi N\} \quad (1)$$

where, ϕdef is the phase due to the pixel motion in the direction of the satellite's view (line of sight), ϕatm is the difference in the atmospheric phase delay between the two images, ϕorb is the remaining phase due to the orbital error, $\phi \theta$ is the remaining phase due to the viewing angle error (which is usually DEM error) and ϕN is the noise phase due to the diversity in the diffusers and thermal noise. The operator W indicates that the received phase has a value between these two figures (π and π-). Since the satellite does not record the correct numbers of proper wave cycles, one of the most important, and at the same time, the most difficult stages in radar interference is

estimating the number of correct cycles, which is called phase retrieval. (Ghani Ardakani and Maleki, ,2016)

lioIn radar interferometry which is a phase obtained from two images taken from a given region for producing interferometric. In fact, the interfering product is a mixed result of two radar images. These two images may be taken by an airplane or space containing two antennas with a specified distance (line-of-sight) (single-track interferometry) or two images at different intervals and from a similar platform (method intermittent crossing with frequent passage) (Ghani Ardakani and Maleki, 2016). The phase difference in the two images is shown in the form of an edge or border in the interfacing, where each boundary or edge is related to the fuzzy difference. The provided interferometer by InSAR method has the ability to display elevation changes and ripples (Chaussard et al., 2014).

The radar interferometry (InSAR) provides the possibility of generating digital models of roughness earth whose optimum heights for the 6.5-c wave band data is about 5 meters. This term is used to measure some of the parameters, such as topography, variation and displacement of the earth's surface which are caused by phase interference of two or more radar images taken from the same area (SAR) with a virtual hole (Iran Space Agency website). This method is capable of detecting surface changes occurring on the ground at different intervals with millimeter precision using at least three (two radar image + DEM)or more radar images (Figure 1). However, this accuracy will be the Equation1 of the data wavelength used and half its equivalent (λ 1/2). The radar interferometry method for measuring the surface changes of the earth's crust is admirable (Shirani et al., 2014).

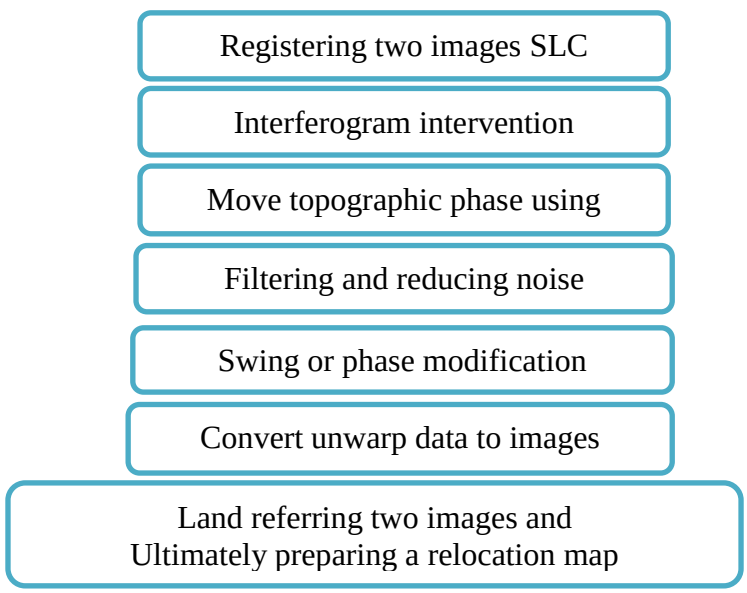

Chart 1. The stages of processing and producing subsidence and collapse maps

In this article, the description and justification of the concepts of basic words that underlie the foundation of the research are proposed, such as the patterns and techniques that can be helpful in understanding this research, the following can be mentioned:

So far, geomorphologists have tried to explain the geomorphic phenomena within the framework of the causality law (Shimoni, et al., 2017). Whereas in geographic space, contrary to classical geography, there is no requirement for the existence of relations between phenomena to be public, and only the proposed relations are of a generic type that can justify causality (Pourkhosrowani et al., 2012). And, of course, the generic relationship with what is called the correlation has a fundamental difference. Dual can be duality and duality can be doubled, a term which also implies the concept of implicit contrast, and conjunction of two phenomena. Duality can contain the symmetry of two phenomena, operating in vice versa, and specify some ratios. The design of the theory of duality in geomorphology, which is hereinafter referred to as "geodesy", is not the simple concept and expression of its implications in geomorphology, but stimulate the researchers in this field to generalize a review of how to manage, control and monitor much data of the phenomenon of geomorphology (Harvey, 2001). In describing this idea, an attempt has been made to rely on empirical-analogical approach and the interferometry-wave technique of the wave (ratio) (and its effects on geomorphology analysis). In general, the results of using this concept show that analyzing them can be in the framework of the theory of geo-duality which can create complete cause to the classical analysis in geomorphology. Although the concept of dual with concepts like coupling and duality have false similarity, and similarities can be found in the technical domain, there is an analysis of the numbers and their equivalence, but with a significant difference. Dual should not be understood by the concept of equivalent duality (Pourkhosrowani, 2015), but from the philosophical point of view, a term that can carry its meaning in Persian, one should use the paired terms. Land subsidence due to groundwater extraction is known as a major problem with environmental impacts in many areas. The creation of a subsidence phenomenon due to inappropriate groundwater abstraction, geological factors, Samadimoghadam, 2016) and the following factor comes from the porosity of soil aggregates, density, type, composition of layers, pumping method and ground structure.

Area of the region, hydraulic conductivity of the layers, rainfall and temperature are the factors affecting subsidence of the earth (Akbari et al., 2009). Unnecessary groundwater extraction causes loss of water levels and decreases the fluid pressure and thus increases the intermediate particle pressure which leads to the formation of the phenomenon of subsidence of the earth. The uneven drop in groundwater levels, the heterogeneity of tissue, sediment, and alluvial characteristics of the area also causes the irregular subsidence of the earth and creates gaps in the earth's crust. Land subsidence has been reported in many plains from dry and semi-arid areas of central and eastern Iran with a sustained decline in groundwater levels. The statistics of the country's plains, facing this phenomenon has reached 751 plains. This phenomenon is observed in other plains of Iran such as Arak, Nahavand, Khomein, Natanz, Yazd, Abarkuh, Kashmar plain in Khorasan Razavi province which is under development (Ghani ardakani Maleki, 2016). The frontier effects resulting from the development of land surfaces can be reduced by precise planning and conservation matters. The environmental consequences of the subsidence phenomenon (Sun et al., 2017) includes damage to

man-made structures such as buildings, streets, bridges and power lines, creating gaps on the surface of the earth and the flood. In all the subsidence that occurs in Iran, extraction of underground water is the only factor or the main cause of subsidence. To measure the phenomenon of deformation, one needs to study the time series in a study area. Therefore, several images should be available at different time intervals of that area and several interferogram between different time periods embedded to calculate the deformation rate in the calculations (Yarahmadi et al., 2015). This method is known as interferometric technique since the received phase is as the fraction of the phase needed to estimate the displacement implemented as a phase retrieval phase.

3. Results and Discussion

The data used in this research are of two categories: one the data Piezometric area of the region which according to the map piezometric wells area (Figure 2) of the water level height in wells in the years 1983 to 1993 were examined and evaluated which observed a 10 to 20 meter water level drop in between years. Due to this amount of water loss in the region, definitely the subsidence of the earth's surface has also been observed.

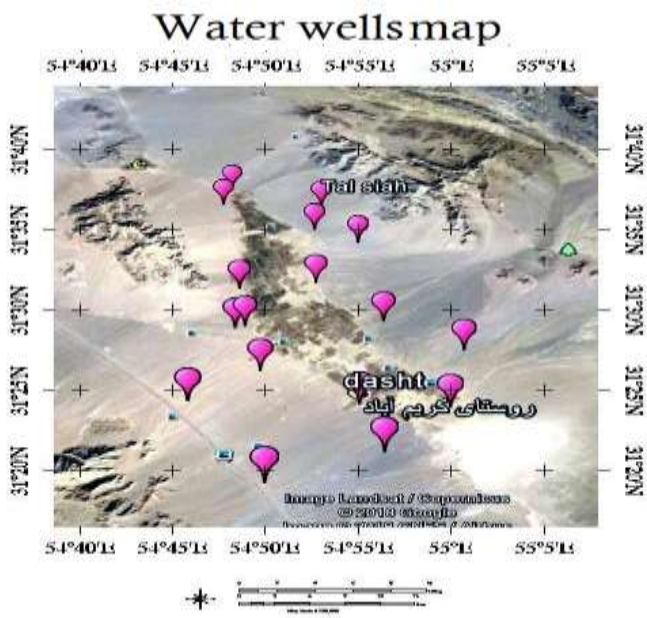

Figure 2. Map of wells in the study area

In this research, using a land survey method, the subsidence model was developed based on the following tables in the GIS and SPSS software.

Linear regression and modeling of land subsidence

Table 1. Modeling

Model Summary[b]

Model	R	R Square	Adjusted R Square	Std. Error of the Estimate	Change Statistics				
					R Square Change	F Change	df1	df2	Sig. F Change
1	.367[a]	.135	.124	38.132	.135	13.371	1	86	.000

a. Predictors: (Constant), groundwater extraction

b. Dependent Variable: subsidence

Table 2. Liner Regression

ANOVA[a]

Model		Sum of Squares	df	Mean Square	F	Sig.
1	Regression	19441.573	1	19441.573	13.371	.000[b]
	Residual	125045.870	86	1454.022		
	Total	144487.443	87			

a. Dependent Variable: subsidence

b. Predictors: (Constant), groundwater extraction

Interpretation of Table 2-ANOVA-: A single-variable linear regression model is meaningful between the rate of groundwater extraction and land subsidence

Linear regression coefficient B

Table 3. Linear regression coefficient

Model	Unstandadized coefficients		standadized coefficients	t	Sig.	95.0%Confidence Interval for B		Collinearity Statistics	
	B	Str.Error	Beta			Lower Bound	Upper Bound	Tolerance	VIF
1(Constant) groundwater extraction	62.884 1.538	13.402 .421	.367	4.692 3.657	.000 .000	36.242 .702	89.525 2.375	1.000	1.000

a:Dependent Variable :Subsidence

T distribution in this table with 0.421 indicates that there is no distribution and it is significant.

Interpretation: in Table 3, coefficients shows that there is a direct and significant relationship between the amount of groundwater extraction and the land subsidence, so that for one unit of increase in water extraction, the average land subsidence increases by 1.5 units.

Charts

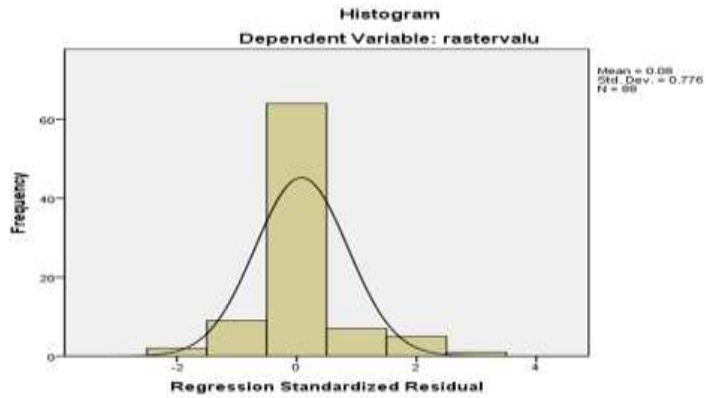

Chart 2. Normal distribution

The linear regression in Table 2,3 assumption is that the remainder of the model has a normal distribution, which, as we can see, assumes this assumption.

The significance of the regression is also shown in the table that the level (Sig = 0.00) is 99% less than 0.05. It can be deduced that the ratio of two variables is significant.

Based on linear regression, the amount of subsidence (Y) can be predicted through the rate of water harvesting (x).

$Y=a+bx$ (2)

Y= the amount of predicted dependency (the amount of land subsidence), a= constant value (the amount of dependent variable at the time when the independent variable is zero) b= Line slope or regression coefficient," X "is the independent variable values (piezometric wells)

$Y=62.884+1.538*X$

X: water extracting rate Y: subsided pictures

For each unit the variation in water extraction, 1.538 variations are created in height.

- The model derived from the following formula, the components of which were described above, were analyzed by SPSS software and concluded that the correlation coefficient between the two parameters is as Equation (2)

- The correlation coefficient of the two parameters is positive with each other, which means that in the space where the study is done, the increase of a parameter with the increase of the other parameter, and also the reduction of that parameter, is accompanied by a decrease in the other parameter. In this model, changes and extraction from the water surface can predict 0.367 percent of the subsidence.

The quantity r^2 or R^2, also called the determination coefficient, is the ratio of the variables (variables) defined to the total variables (variables). (This measure allows us to determine how much it can predict a reliable model or diagram.) The value of the determination coefficient is in the range $0 < r^2 < 1$ which represents the percentage of recruits that are closer to the regression

line. For example, when $r^2 = 0.797$, this means that 79% of the total variation of y can be obtained through the linear relationship between x and y through the defined equation, and 21% of the y variables are not defined- Adjusted coefficient: The important difference between the coefficient of determination and the adjusted coefficient of determination is that the coefficient of determination assumes that each independent variable observed in the model explains the changes in the dependent variable. Therefore, the percent represented by the coefficient of determination assumes the effect of all independent variables on the dependent variable. If the percentages indicated by the modified coefficient are only due to the actual effect of the independent variables of the model, then not all independent variables. The other difference is that the suitability of the variables for the model cannot be determined by the coefficient of determination even with a high value, if the value of the estimated adjusted coefficient can be trusted.

Table 4. Model

Model	Correlation coefficient	Coefficient of determination	Adjusted coefficient
1	0.367	0.797	0.74

In table.5, number 6 is the coefficient of determination and number 7 is Adjusted coefficient

Table 5. Balance equilibrium

OBJECTID*	VARNAME	VARABLE	DEFINITION
1	Neighbors	22	
2	ResidualSquares	29242.771295	
3	Effective Number	20.055553	
4	Sigma	20.7459	
5	AICc	801.237358	
6	R2	0.79761	
7	R2 adjusted	0.740849	
8	Dependent field	0	subsidence
9	Explanatory field	1	groundwater

The second group data is radar information. Radar interferometric computing in this research is based on six images ENVISAT with low imaging geometry. 6 Interfrogram images with software help Sarscape and the Orbital Information Agency of the European Space Agency Specification Interferogram (Table 5) processed in the study area by considering the spatial basis. In order to reduce noise and increase the correlation between interferograms an attempt has been made to use a pair of radar images with a short period of time.

Table 6. Specifications of processed interferogram in plain Bahadoran Yazd.

Spatial base line	Secondary image	Primitive image	number
911	29/7/2005	22/6/2003	1
416	25/4/2007	10/5/2006	2
398	16/9/2011	21/2/2011	3

After the production of interferograms by applying the phase-to-gap coefficient, displacement maps were prepared in the time series of the (Table 5). The survey of displacement maps shows that the phenomenon of subsidence in the central region of the study area has almost reached the same rate and anyway to the northwest or to the elevation around the area, The subsidence will be reduced and increased by a large proportion.Radar surveys which show that the ratio of each type is between the subsidence and the extinction in the region. As it subsides in the plains, it has been relatively more frequent, but in the heights it has been observed to be relatively less.

In exploring the radar data, it clearly shows a slight relationship between subsidences and uplifting in the region of the plains and the area has fallen subsidence to a greater extent but small range of uplifting has been seen at high altitudes. The statistics in the survey suggest that the mean maximum subsidence is 0.25 meter and the mean maximum uplifting is 0.07 meter, respectively (Figure 4, 5 and 6).

Displacement maps of the study area at different time intervals

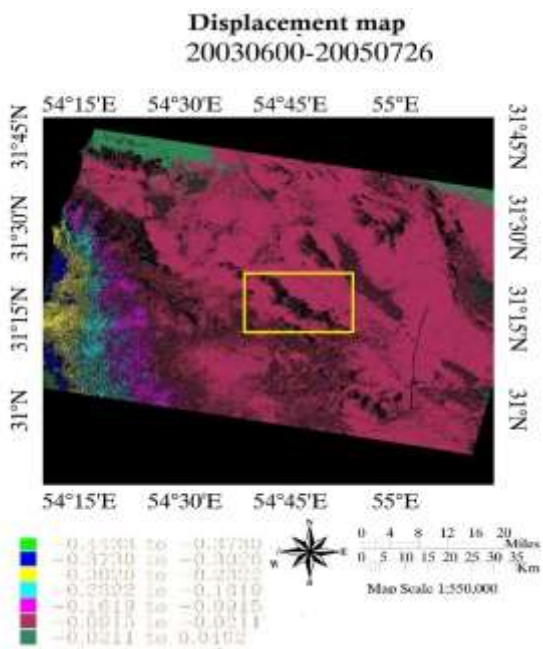

Figure 4. Displacement between 2005 and 2003

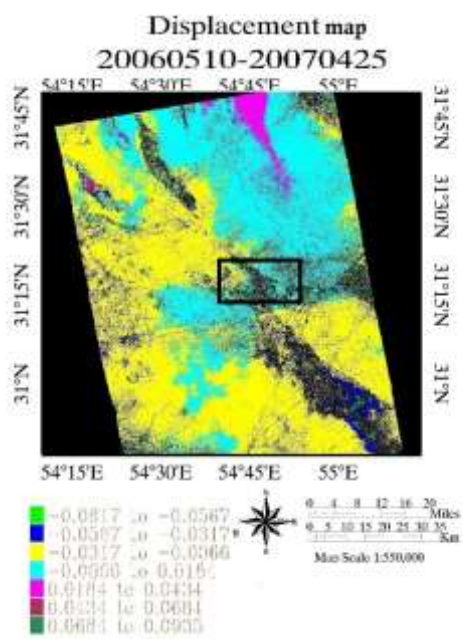

Figure 5. Displacement between 2007 and 2006

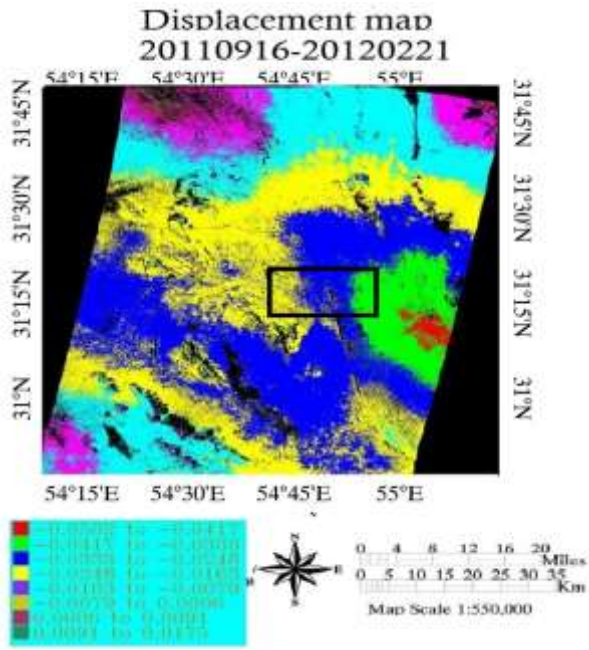

Figure 6. Displacement between 2011 and 2012

The subsidence and uplifting variations on the maps of the study shows that the largest subsidence in the plain has occurred in the flat zones and the most uplifting is seen on the high mountains overlooking and in the surrounding mountains.

According to the results specified in the data mining section, the use of the radar interferometry method shows the proper capacity of its capabilities in determining the range of subsidence at the levels. The dry climate of the study area decreases the effect of the phase shift caused by atmospheric compounds to the viscosity of the humidity, providing an accurate measure of the phase difference resulting from surface displacement. Also, the lack of co-incident vegetation in the phase of radar images in the C band is the least. It was possible to measure phase change over the annual time interval for the C band data, which indicates that the displacement numbers are close in two maps with different wavelengths. Groundwater harvesting has reduced the piezometric pressure which this reduction of the piezometric pressure causes an imbalance and increased pressure from the upper sediments. So that the porosity of the sediments is reduced and the density increases, which is one of the factors of subsidence if the pores are filled with rain water or temporary rivers and this will prevent collapse in the area.

4. Conclusions

The results of this research show that the study of duality has been proved in the domain of geomorphologies function. This review calls the general thinking in question that is associated to the complete cause of subsidence which is reduced groundwater and has been claimed by scholars and researchers because by monitoring the causes, the breaks in this area have reached over 60

years while the mechanical extraction of groundwater has short lifespan. Therefore, it can be concluded that the movements of the earth's crust has important and fundamental causes of uplifting and subsidence. Secondly, the subsidence and uplifting can be explained and defined in the duality of geomorphology. These ups and downs caused by the unnecessary extraction of groundwater witnesses the crust movements in the plains and the adjacent peaks which indicates the crust motions in order to achieve the crustal balance. Whereas, the subsidence occurred alone, as no line of equilibrium observed on the heights. Displacement maps were prepared according to the time series in Table 5. The evaluation map of the displacement rate demonstrates the phenomenon of subsidence in the boundary of the central region of the case study for the evaluated years and as far as the center of the Bahadoran plain to the north western and other regions around the area comes from the rate of the subsidence declined and slightly added to uplifting. In exploring the radar data, it is clear that there is a slight relationship between subsidence and uplifting as in the region of the plains and the area has fallen subsidence to a greater extent. But small range of uplifting were observed at high altitudes. The survey statistics suggest that the mean maximum subsidence is 0.25 meter and the mean maximum uplifting is 0.07 meter, respectively (Figure 4, 5 and 6).

As a result, the hypothesis of this research can be verified by experiments because the direct relation between the subsidence and uplifting by radar interferometry has a significant correlation.

References

Adib, A., Afzal, P., & Zare, M. (2016). Seismic zoning East of Yazd province based on earthquakes and faults Quaternary using fractal modeling. Advanced Applied Geology, 22.

Akbari, M., Jirga, M., & Rauf, (2009). system application Geographic Information (GIS) in Resource Management Review Groundwater) Case study: Kashmar plain aquifer Bradsank. In the first National Symposium on Correction) Consumption based on natural resources, agriculture and so on Veterinary, University of Zabol (in Farsi).

Buck, P.E.(2011). Detecting prehistoric landscape use through remote sensing in new Arizona, , USA. in 2011 GSA Annual Meeting in Minneapolis.

Cigna, F., Osmanoğlu, B., Cabral-Cano, E., Dixon, T. H., Avila-Olivera, J. A., Garduno-Monroy, V. H., & Wdowinski, S. (2012). Monitoring land subsidence and its induced geological hazard with Synthetic Aperture Radar Interferometry: A case study in Morelia, Mexico. Remote Sensing of Environment, 117, 146-161.

Chaussard, E., Wdowinski, S., Cabral-Cano, E., & Amelung, F. (2014). Land subsidence in central Mexico detected by ALOS InSAR time-series. Remote sensing of environment, 140, 94-106.

Eslamizadeh, A. & Samanirad, S. (2010). Land subsidence and fissuring due to ground water withdrawal in Yazd-Ardakan basin, central Iran. World Academy of Science, Engineering and Technology, 48, 489-492.

Ghani Ardakani, J., & Maleki, Z. (2016). Evaluating the causes and Environmental effects of the phenomenon of subsidence in the Earth Yazd Ardakan plain. In the second international congress Land, space, and clean energy with a management focus Natural resources, agriculture and sustainable development. Kian Design Company (in Farsi).

Harvey, A. M. (2001). Coupling between hillslopes and channels in upland fluvial systems: implications for landscape sensitivity, illustrated from the Howgill Fells, northwest England. Catena, 42(2-4), 225-250.

Hakimi, S. (2015). Fault Patterns and High Speed Estimates Excavation along high Zagros fault. Earth Magazine Engineering, 1(2), (in Farsi).

Monserrat, O., Crosetto, M., & Luzi, G. (2014). A review of ground-based SAR interferometry for deformation measurement. ISPRS Journal of Photogrammetry and Remote Sensing, 93, 40-48.

Maghsoudi, Mehran-Zamzadeh, Seyyed Mohammad-Mamani, Mojtaba (2018), Investigating active tectonics of Maroon basin using geomorphic indices, Journal of Quantitative Geomorphology Researches, Volume 6, Number 3, pp. 24-32(in farsi)

Pourkhosrowani, M. (2015). Geo-Duality Theory Ideas in Geomorphology Knowledge (geography and program). Environmental Design, 25(1), 25-36 (in Farsi).

Pourkhosrowani M., Ramasht, M., & Al-Murdasi, SA. (2012). Duality in Geomorphology. Researches Natural Geography, 44(3), 63-72 (in Farsi).

Samadimoghadam, R. (2016). Fault Neotectonic Evaluation Kelmrd using GIS, Shirghest area). Central Journal of Geography and Development, 14(45), 159-180 (in Farsi).

Sun, H., Zhang, Q., Zhao, C., Yang, C., Sun, Q., & Chen, W. (2017). Monitoring land subsidence in the southern part of the lower Liaohe plain, China with a multi-track PS-InSAR technique. Remote Sensing of Environment, 188, 73-84.

Shimoni, M., Lopez, J., Walstra, J., Declercq, P. Y., Bejarano-Urrego, L., Verstrynge, E., & Van Balen, K. (2017). GEPATAR: A geotechnical based PS-InSAR toolbox for architectural conservation in Belgium. In Geoscience and Remote Sensing Symposium (IGARSS), 2017 IEEE International (pp. 5555-5558). IEEE.

Shirani, K., Seif, A., & Sharifikia, M. (2014). ASAR and PALSAR sensors assessment for landslide detection, monitoring using differential interferometry in Zagros Mountains. Journal of Watershed Engineering and Management.

Iran Space Agency website. Retrieved from: http://isa.ir/find.php?item=2.133.946.fa (in Farsi).

Yarahmadi, J., Sharifikia, M., Roustaei, M., & Roustaei, Sh. (2015). Identification and monitoring of instability different interframe meter processing Case Study: Garmichay Mianeh Basin. Journal of Quantitative Geomorphology Research, 3(4), 44-59 (in Farsi).